CERN/LHCC 2013-022
LHCb TDR 14
28 November 2013

UPGRADE

LHCb Particle Identification TDR

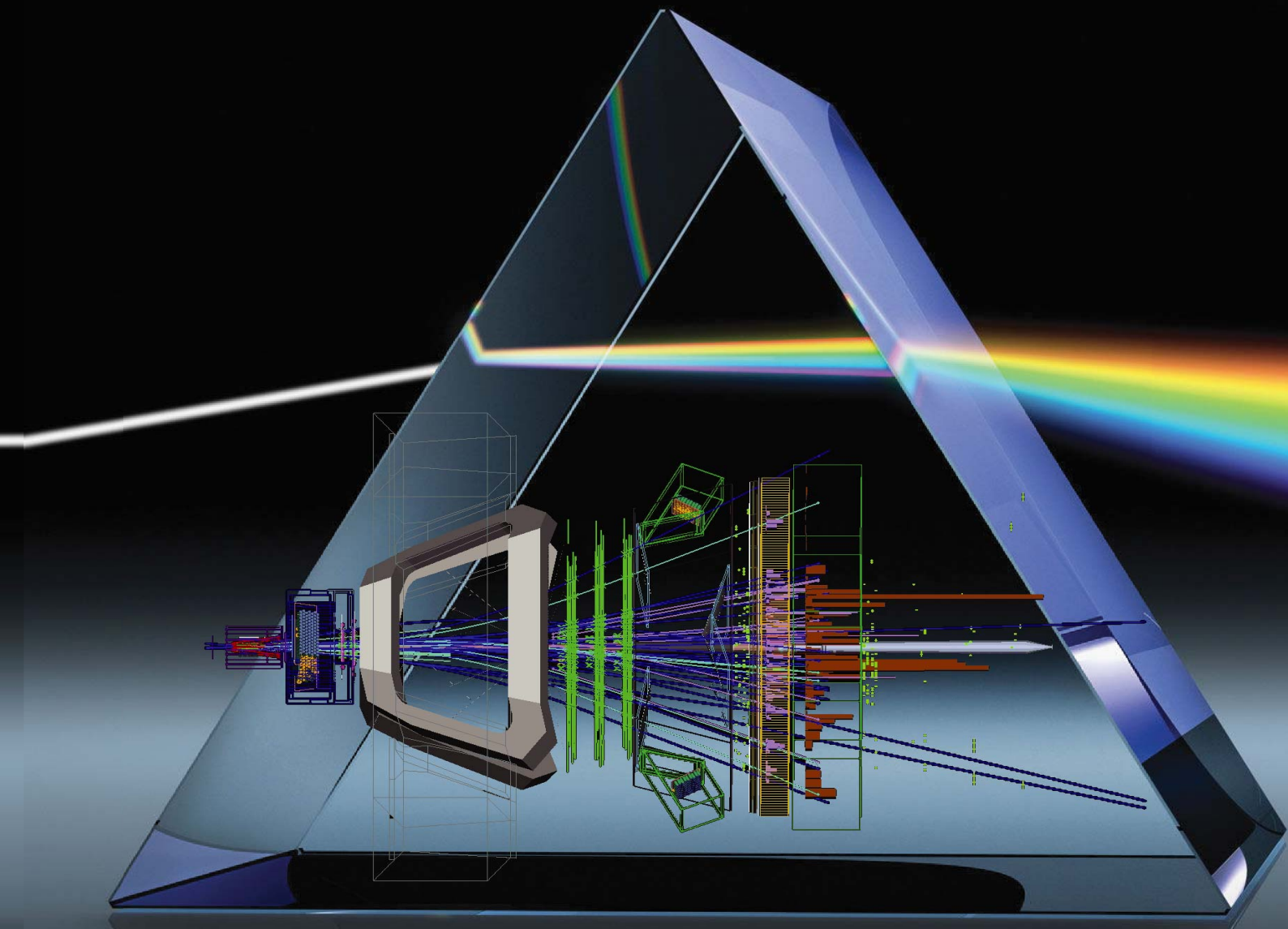

Technical Design Report

CERN/LHCC 2013-022
LHCb TDR 14
November 28, 2013

LHCb Particle Identification Upgrade Technical Design Report

The LHCb Collaboration

Abstract

The LHCb upgrade will take place in the second long shutdown of the LHC, currently scheduled to begin in 2018. The upgrade will enable the experiment to run at luminosities of $2 \times 10^{33}\text{cm}^{-2}\text{s}^{-1}$ and will read out data at a rate of 40 MHz into a flexible software-based trigger. All sub-detectors of LHCb will be re-designed to comply with these new operating conditions. This Technical Design Report presents the upgrade plans of the Ring Imaging Cherenkov (RICH) system, the calorimeter system and the muon system, which together provide the particle identification capabilities of the experiment.

LHCb collaboration

I. Bediaga, J.M. De Miranda, F. Ferreira Rodrigues, A. Gomes[a], A. Hicheur, A. Massafferri, I. Nasteva, A.C. dos Reis, A.B. Rodrigues
[1] *Centro Brasileiro de Pesquisas Físicas (CBPF), Rio de Janeiro, Brazil*

S. Amato, K. Carvalho Akiba, L. De Paula, O. Francisco, M. Gandelman, J.H. Lopes, D. Martins Tostes, J.M. Otalora Goicochea, E. Polycarpo, M.S. Rangel, V. Salustino Guimaraes, B. Souza De Paula, D. Szilard, D. Vieira
[2] *Universidade Federal do Rio de Janeiro (UFRJ), Rio de Janeiro, Brazil*

M. Cruz Torres, C. Göbel, J. Molina Rodriguez
[3] *Pontifícia Universidade Católica do Rio de Janeiro (PUC-Rio), Rio de Janeiro, Brazil*

Y. Gao, F. Jing, Y. Li, H. Lu, S. Wu, Z. Yang, X. Yuan, F. Zhang, Y. Zhang, L. Zhong
[4] *Center for High Energy Physics, Tsinghua University, Beijing, China*

I. De Bonis, D. Decamp, N. Déléage, C. Drancourt, Ph. Ghez, J.-P. Lees, B. Lieunard, J.F. Marchand, M.-N. Minard, B. Pietrzyk, W. Qian, S. T'Jampens, V. Tisserand, E. Tournefier[59]
[5] *LAPP, Université de Savoie, CNRS/IN2P3, Annecy-Le-Vieux, France*

Z. Ajaltouni, M. Baalouch, E. Cogneras, O. Deschamps, I. El Rifai, M. Grabalosa Gándara, P. Henrard, M. Hoballah, R. Lefèvre, J. Maratas, S. Monteil, V. Niess, P. Perret, D.A. Roa Romero
[6] *Clermont Université, Université Blaise Pascal, CNRS/IN2P3, LPC, Clermont-Ferrand, France*

C. Abellán Beteta, E. Aslanides, J. Cogan, W. Kanso, R. Le Gac, O. Leroy, G. Mancinelli, A. Mordà, M. Perrin-Terrin, M. Sapunov, J. Serrano, A. Tsaregorodtsev
[7] *CPPM, Aix-Marseille Université, CNRS/IN2P3, Marseille, France*

Y. Amhis, S. Barsuk, C. Beigbeder-Beau, M. Borsato, T. Cacérès, O. Callot, D. Charlet, O. Duarte, O. Kochebina, J. Lefrançois, F. Machefert, A. Martín Sánchez, M. Nicol, P. Robbe, M.-H. Schune, M. Teklishyn, A. Vallier, B. Viaud, G. Wormser
[8] *LAL, Université Paris-Sud, CNRS/IN2P3, Orsay, France*

E. Ben-Haim, M. Charles, S. Coquereau, P. David, L. Del Buono, A. Martens, D.A. Milanes, F. Polci
[9] *LPNHE, Université Pierre et Marie Curie, Université Paris Diderot, CNRS/IN2P3, Paris, France*

J. Albrecht, T. Brambach, Ch. Cauet, M. Deckenhoff, U. Eitschberger, R. Ekelhof, M. Kaballo, F. Kruse, F. Meier, R. Niet, C.J. Parkinson, M. Schlupp, A. Shires, B. Spaan, S. Swientek, J. Wishahi
[10] *Fakultät Physik, Technische Universität Dortmund, Dortmund, Germany*

O. Aquines Gutierrez, J. Blouw, M. Britsch, M. Fontana, D. Popov, M. Schmelling, D. Volyanskyy, H. Voss, M. Zavertyaev[b]
[11] *Max-Planck-Institut für Kernphysik (MPIK), Heidelberg, Germany*

S. Bachmann, A. Bien, M. De Cian, A. Di Canto, F. Dordei, C. Färber, E. Gersabeck, L. Grillo, S. Hansmann-Menzemer, A. Jaeger, K. Kreplin, G. Krocker, B. Leverington, C. Linn, J. Marks, M. Meissner, T. Nikodem, P. Seyfert, S. Stahl, J. van Tilburg, U. Uwer, M. Vesterinen, S. Wandernoth, D. Wiedner, A. Zhelezov
[12] *Physikalisches Institut, Ruprecht-Karls-Universität Heidelberg, Heidelberg, Germany*

O. Grünberg, T. Hartmann, M. Heß, C. Voß, R. Waldi
[13] *Institut für Physik, Universität Rostock, Rostock, Germany*

R. McNulty, R. Wallace, W.C. Zhang
[14] *School of Physics, University College Dublin, Dublin, Ireland*

A. Palano[c]
[15] *Sezione INFN di Bari, Bari, Italy*

A. Carbone[d], D. Galli[d], U. Marconi, S. Perazzini[d], V. Vagnoni, G. Valenti, M. Zangoli
[16] *Sezione INFN di Bologna, Bologna, Italy*

M. Arba, W. Bonivento[42], S. Cadeddu, A. Cardini, A. Contu[42], L. Ladelfa, A. Lai, B. Liu, G. Manca[e], D. Marras, R. Oldeman[e], B. Saitta[e], M. Tuveri
[17] *Sezione INFN di Cagliari, Cagliari, Italy*

M. Andreotti[f], W. Baldini, C. Bozzi, R. Calabrese[f], S. Chiozzi, A. Cotta Ramusino, A. Falabella[f], M. Fiore[f], M. Fiorini[f], E. Luppi[f], R. Malaguti, M. Manzali[f], A. Mazurov[42,f], M. Melchiorri, L. Milano[f], L. Pappalardo, M. Savrie[f], I. Shapoval[49,f], G. Tellarini[f], L. Tomassetti[f], S. Vecchi
[18] *Sezione INFN di Ferrara, Ferrara, Italy*

L. Anderlini[g], A. Bizzeti[i], M. Frosini[42,g], G. Graziani, G. Passaleva, M. Veltri[h]
[19] *Sezione INFN di Firenze, Firenze, Italy*

M. Anelli, A. Balla, G. Bencivenni, P. Campana[42], M. Carletti, P. Ciambrone, P. De Simone, G. Felici, M. Gatta, G. Lanfranchi, M. Palutan, M. Rama, R. Rossellini, A. Saputi, A. Sarti, B. Sciascia, R. Vazquez Gomez
[20] *Laboratori Nazionali dell'INFN di Frascati, Frascati, Italy*

R. Cardinale[j], M. Cresta, F. Fontanelli[j], S. Gambetta[j], P. Musico, C. Patrignani[j], A. Petrolini[j], A. Pistone
[21] *Sezione INFN di Genova, Genova, Italy*

M. Calvi[k], P. Carniti, L. Cassina, A. Giachero, C. Gotti, B. Khanji, M. Kucharczyk[28,42,k], M. Maino, C. Matteuzzi, G. Pessina
[22] *Sezione INFN di Milano Bicocca, Milano, Italy*

A. Abba, F. Caponio, M. Citterio, S. Coelli, A. Cusimano[v], J. Fu, A. Geraci[v], M. Lazzaroni, M. Monti, N. Neri, F. Palombo[u]
[23] *Sezione INFN di Milano, Milano, Italy*

S. Amerio, M. Benettoni, G. Busetto[r], A. Gianelle, D. Lucchesi[r], M. Morandin, M. Rotondo, G. Simi, R. Stroili
[24] *Sezione INFN di Padova, Padova, Italy*

F. Bedeschi, S. Leo, P. Marino[t], M.J. Morello[t], G. Punzi[s], F. Ruffini, F. Spinella, S. Stracka[42]
[25] *Sezione INFN di Pisa, Pisa, Italy*

G. Carboni[l], E. Furfaro[l], E. Santovetti[l], A. Satta
[26] *Sezione INFN di Roma Tor Vergata, Roma, Italy*

A.A. Alves Jr, G. Auriemma[n], V. Bocci, G. Martellotti, G. Penso[m], D. Pinci, G. Sabatino[l], R. Santacesaria, C. Satriano[n], A. Sciubba
[27] *Sezione INFN di Roma La Sapienza, Roma, Italy*

M. Baszczyk[o], P. Dorosz[o], A. Dziurda, W. Kucewicz[o], T. Lesiak, P. Morawski, G. Polok, B. Rachwal, J. Wiechczynski, M. Witek
[28] *Henryk Niewodniczanski Institute of Nuclear Physics Polish Academy of Sciences, Kraków, Poland*

M. Idzik, B. Muryn, A. Oblakowska-Mucha, K. Senderowska, T. Szumlak
[29] *AGH - University of Science and Technology, Faculty of Physics and Applied Computer Science, Kraków, Poland*

V. Batozskaya, K. Kurek, M. Szczekowski, A. Ukleja, W. Wislicki
[30] *National Center for Nuclear Research (NCBJ), Warsaw, Poland*

C. Coca, L. Giubega, A. Grecu, F. Maciuc, R. Muresan, M. Orlandea, C. Pavel-Nicorescu, B. Popovici, S. Stoica, M. Straticiuc, E. Teodorescu
[31] *Horia Hulubei National Institute of Physics and Nuclear Engineering, Bucharest-Magurele, Romania*

G. Alkhazov, N. Bondar, A. Dzyuba, O. Maev[42], N. Sagidova, Y. Shcheglov, A. Vorobyev
[32] *Petersburg Nuclear Physics Institute (PNPI), Gatchina, Russia*

V. Balagura, S. Belogurov, I. Belyaev, V. Egorychev, D. Golubkov, A. Konoplyannikov, T. Kvaratskheliya[42], I.V. Machikhiliyan, S. Polikarpov, I. Polyakov, D. Savrina[34], A. Semennikov, P. Shatalov, A. Zhokhov
[33] *Institute of Theoretical and Experimental Physics (ITEP), Moscow, Russia*

A. Berezhnoy, M. Korolev, A. Leflat, A. Martynov, N. Nikitin
[34] *Institute of Nuclear Physics, Moscow State University (SINP MSU), Moscow, Russia*

S. Filippov, E. Gushchin, O. Karavichev, L. Kravchuk, A. Tikhonov
[35] *Institute for Nuclear Research of the Russian Academy of Sciences (INR RAN), Moscow, Russia*

V. Shevchenko, A. Ustyuzhanin
[36] *National Research Centre Kurchatov Institute, Moscow, Russia*

A. Bondar, S. Eidelman, P. Krokovny, V. Kudryavtsev, L. Shekhtman, V. Vorobyev
[37] *Budker Institute of Nuclear Physics (SB RAS) and Novosibirsk State University, Novosibirsk, Russia*

A. Artamonov, K. Belous, E. Chernov, R. Dzhelyadin, Yu. Guz[42], A. Novoselov, V. Obraztsov, A. Popov, V. Romanovsky, M. Shapkin, M. Soldatov, O. Yushchenko
[38] *Institute for High Energy Physics (IHEP), Protvino, Russia*

A. Badalov, M. Calvo Gomez[p], A. Camboni, A. Comerma-Montells, L. Garrido, D. Gascon, R. Graciani Diaz, E. Graugés, G. Loustau, J. Mauricio, A. Oyanguren, E. Picatoste Olloqui, C. Potterat, V. Rives Molina, M. Rosello[p], H. Ruiz, P. Ruiz Valls, X. Vilasis-Cardona[p]
[39] *Universitat de Barcelona, Barcelona, Spain*

B. Adeva, P. Alvarez Cartelle, A. Dosil Suárez, V. Fernandez Albor, A. Gallas Torreira, J.A. Hernando Morata, A. Pazos Alvarez, E. Perez Trigo, M. Plo Casasus, P. Rodriguez Perez, A. Romero Vidal, J.J. Saborido Silva, B. Sanmartin Sedes, C. Santamarina Rios, M. Seco, P. Vazquez Regueiro, C. Vázquez Sierra
[40] *Universidad de Santiago de Compostela, Santiago de Compostela, Spain*

F. Martinez Vidal, J. Mazorra de Cos
[41] *Instituto de Fisica Corpuscular (IFIC), Universitat de Valencia-CSIC, Valencia, Spain*

F. Alessio, F. Archilli, J. Buytaert, D. Campora Perez, L. Castillo Garcia, M. Cattaneo, Ph. Charpentier, K. Ciba, X. Cid Vidal, M. Clemencic, J. Closier, V. Coco, P. Collins, G. Corti, B. Couturier, C. D'Ambrosio, H. Dijkstra, P. Durante, M. Ferro-Luzzi, C. Fitzpatrick, R. Forty, M. Frank, C. Frei, C. Gaspar, V.V. Gligorov, H. Gordon, L.A. Granado Cardoso, T. Gys, C. Haen, J. He, T. Head, E. van Herwijnen, R. Jacobsson, C. Joram, B. Jost, M. Karacson, T.M. Karbach, D. Lacarrere, E. Lanciotti, C. Langenbruch, R. Lindner, G. Liu, S. Lohn, R. Matev, Z. Mathe, S. Neubert, N. Neufeld, R. Paluch, J. Panman, M. Pepe Altarelli, D. Piedigrossi, N. Rauschmayr, S. Roiser, T. Ruf, H. Schindler, B. Schmidt, A. Schopper, R. Schwemmer, F. Stagni, V.K. Subbiah, F. Teubert, E. Thomas, D. Tonelli, M. Ubeda Garcia, O. Ullaland, J. Wicht, K. Wyllie, A. Zvyagin
[42] *European Organization for Nuclear Research (CERN), Geneva, Switzerland*

C. Barschel, A. Bay, F. Blanc, J. Bressieux, M. Dorigo, F. Dupertuis, G. Haefeli, P. Jaton, C. Khurewathanakul, I. Komarov, V.N. La Thi, N. Lopez-March, J. Luisier, R. Märki, B. Muster, T. Nakada, A.D. Nguyen, T.D. Nguyen, C. Nguyen-Mau[q], J. Prisciandaro, A. Puig Navarro, B. Rakotomiaramanana, J. Rouvinet, O. Schneider, F. Soomro, P. Szczypka[42], M. Tobin, S. Tourneur, M.T. Tran, G. Veneziano
[43]*Ecole Polytechnique Fédérale de Lausanne (EPFL), Lausanne, Switzerland*

J. Anderson, R. Bernet, E. Bowen, A. Bursche, N. Chiapolini, M. Chrzaszcz[28], Ch. Elsasser, F. Lionetto, P. Lowdon, K. Müller, N. Serra, O. Steinkamp, B. Storaci, U. Straumann, M. Tresch, A. Vollhardt
[44]*Physik-Institut, Universität Zürich, Zürich, Switzerland*

R. Aaij, S. Ali, Th. Bauer, M. van Beuzekom, P.N.Y. David, K. De Bruyn, C. Farinelli, V. Heijne, W. Hulsbergen, E. Jans, P. Koppenburg, A. Kozlinskiy, J. van Leerdam, M. Martinelli, M. Merk, I. Mous, S. Oggero, A. Pellegrino, H. Snoek, P. Tsopelas, N. Tuning, J.A. de Vries, L. Wiggers
[45]*Nikhef National Institute for Subatomic Physics, Amsterdam, The Netherlands*

J. van den Brand, F. Dettori, T. Ketel, R.F. Koopman, R.W. Lambert, D. Martinez Santos, G. Raven, M. Schiller, V. Syropoulos, S. Tolk
[46]*Nikhef National Institute for Subatomic Physics and VU University Amsterdam, Amsterdam, The Netherlands*

T.W. Hafkenscheid, G. Onderwater
[47]*KVI - University of Groningen, Groningen, The Netherlands*

E. Pesen
[48]*Celal Bayar University, Manisa, Turkey*

A. Dovbnya, S. Kandybei, I. Raniuk, O. Shevchenko
[49]*NSC Kharkiv Institute of Physics and Technology (NSC KIPT), Kharkiv, Ukraine*

V. Iakovenko, O. Okhrimenko, V. Pugatch
[50]*Institute for Nuclear Research of the National Academy of Sciences (KINR), Kyiv, Ukraine*

S. Bifani, P. Griffith, I.R. Kenyon, C. Lazzeroni, J. McCarthy, L. Pescatore, N.K. Watson
[51]*University of Birmingham, Birmingham, United Kingdom*

M. Adinolfi, J. Benton, N.H. Brook, A. Cook, M. Coombes, J. Dalseno, T. Hampson, S.T. Harnew, P. Naik, C. Prouve, J.H. Rademacker, N. Skidmore, D. Souza, J.J. Velthuis, D. Voong
[52]*H.H. Wills Physics Laboratory, University of Bristol, Bristol, United Kingdom*

W. Barter, M.-O. Bettler, H.V. Cliff, J. Garra Tico, V. Gibson, S. Gregson, S.C. Haines, C.R. Jones, M. Sirendi, J. Smith, D.R. Ward, S.A. Wotton, S. Wright
[53]*Cavendish Laboratory, University of Cambridge, Cambridge, United Kingdom*

J.J. Back, T. Blake, D.C. Craik, D. Dossett, T. Gershon, M. Kreps, T. Latham, T. Pilař, A. Poluektov[37], M.M. Reid, R. Silva Coutinho, C. Wallace, M. Whitehead, M.P. Williams[55]
[54]*Department of Physics, University of Warwick, Coventry, United Kingdom*

S. Easo, R. Nandakumar, A. Papanestis[42], S. Ricciardi, F.F. Wilson
[55]*STFC Rutherford Appleton Laboratory, Didcot, United Kingdom*

S. Benson, H. Carranza-Mejia, L. Carson, P.E.L. Clarke, G.A. Cowan, R. Currie, S. Eisenhardt, D. Ferguson, D. Lambert, H. Luo, A.-B. Morris, F. Muheim, M. Needham, S. Playfer, G. Sidiropoulos, A. Sparkes, J. Webster, Y. Xie[42]
[56]*School of Physics and Astronomy, University of Edinburgh, Edinburgh, United Kingdom*

M. Alexander, J. Beddow, L. Eklund[42], D. Hynds, I. Longstaff, S. Ogilvy, M. Pappagallo, P. Sail, F.J.P. Soler, P. Spradlin
[57] *School of Physics and Astronomy, University of Glasgow, Glasgow, United Kingdom*

A. Affolder, T.J.V. Bowcock, H. Brown, G. Casse, S. Donleavy, S. Farry, K. Hennessy, T. Huse, D. Hutchcroft, M. Liles, B. McSkelly, G.D. Patel, A. Pritchard, K. Rinnert, T. Shears, N.A. Smith
[58] *Oliver Lodge Laboratory, University of Liverpool, Liverpool, United Kingdom*

G. Ciezarek, S. Cunliffe, U. Egede, A. Golutvin[33,42], S. Hall, M. McCann, P. Owen, M. Patel, K. Petridis, A. Richards, T. Savidge, I. Sepp, E. Smith, W. Sutcliffe, D. Websdale
[59] *Imperial College London, London, United Kingdom*

R.B. Appleby, R.J. Barlow, T. Bird, P.M. Bjørnstad, S. Borghi, D. Brett, S. De Capua, M. Gersabeck, J. Harrison, C. Hombach, S. Klaver, G. Lafferty, A. McNab, D. Moran, C. Parkes, A. Pearce, S. Reichert, E. Rodrigues, M. Smith, A.D. Webber
[60] *School of Physics and Astronomy, University of Manchester, Manchester, United Kingdom*

M. Brock, S.-F. Cheung, D. Derkach, R. Gao, R. Gauld, E. Greening, N. Harnew, D. Hill, P. Hunt, N. Hussain, J.J. John, M. John, D. Johnson, O. Lupton, S. Malde, A. Powell, S. Redford, E. Smith[55], S. Stevenson, C. Thomas, S. Topp-Joergensen, N. Torr, G. Wilkinson
[61] *Department of Physics, University of Oxford, Oxford, United Kingdom*

I. Counts, P. Ilten, M. Williams
[62] *Massachusetts Institute of Technology, Cambridge, MA, United States*

R. Andreassen, A. Davis, W. De Silva, B. Meadows[61], M.D. Sokoloff, L. Sun
[63] *University of Cincinnati, Cincinnati, OH, United States*

J.E. Andrews, R. Cenci, B. Hamilton, A. Jawahery, D.A. Roberts, J. Wimberley
[64] *University of Maryland, College Park, MD, United States*

M. Artuso, S. Blusk, A. Borgia, T. Britton, P. Gandini, J. Garofoli, B. Gui, C. Hadjivasiliou, N. Jurik, R. Mountain, B.K. Pal, T. Skwarnicki, S. Stone, J. Wang, Z. Xing, L. Zhang.
[65] *Syracuse University, Syracuse, NY, United States*

[a] *Universidade Federal do Triângulo Mineiro (UFTM), Uberaba-MG, Brazil*
[b] *P.N. Lebedev Physical Institute, Russian Academy of Science (LPI RAS), Moscow, Russia*
[c] *Università di Bari, Bari, Italy*
[d] *Università di Bologna, Bologna, Italy*
[e] *Università di Cagliari, Cagliari, Italy*
[f] *Università di Ferrara, Ferrara, Italy*
[g] *Università di Firenze, Firenze, Italy*
[h] *Università di Urbino, Urbino, Italy*
[i] *Università di Modena e Reggio Emilia, Modena, Italy*
[j] *Università di Genova, Genova, Italy*
[k] *Università di Milano Bicocca, Milano, Italy*
[l] *Università di Roma Tor Vergata, Roma, Italy*
[m] *Università di Roma La Sapienza, Roma, Italy*
[n] *Università della Basilicata, Potenza, Italy*
[o] *AGH - University of Science and Technology, Faculty of Computer Science, Electronics and Telecommunications, Kraków, Poland*
[p] *LIFAELS, La Salle, Universitat Ramon Llull, Barcelona, Spain*
[q] *Hanoi University of Science, Hanoi, Viet Nam*
[r] *Università di Padova, Padova, Italy*

[s] *Università di Pisa, Pisa, Italy*
[t] *Scuola Normale Superiore, Pisa, Italy*
[u] *Università degli Studi di Milano, Milano, Italy*
[v] *Politecnico di Milano, Milano, Italy*

Contents

Chapter 1

Introduction

1.1 Particle identification and the LHCb upgrade

Particle identification (PID) is an essential attribute of any flavour-physics experiment and has been central to the success of LHCb. In LHCb the hadron identification, in particular the separation of pions and kaons, is provided by the Ring Imaging Cherenkov (RICH) system. Hadron PID plays a key role in most LHCb analyses, for example allowing the isolation of different two-body charmless b-hadron decays and the recent first observation of CP-violation in the B_s^0 system [1], or the measurement of the unitary triangle angle γ through the study of $B^\pm \to DK^\pm$ decays [2]. The calorimeter system enables photon and electron identification; the former is of particular importance for studies of radiative Penguin processes and has made possible, for example, the world's most precise study of $B^0 \to K^{*0}\gamma$ and $B_s^0 \to \phi\gamma$ decays [3]. Many heavy flavour decays of interest have muons in the final state, and the identification capabilities provided by the LHCb muon system have recently led to the discovery of the highly suppressed and important mode $B_s^0 \to \mu^+\mu^-$ [4–6]. Particle identification is also mandatory for flavour tagging, which is necessary in time-dependent CP-violation studies. Finally, the calorimeter and muon systems are critical to the LHCb trigger as they give the input to the L0 decision, which is the earliest trigger level of the current experiment.

The LHCb upgrade will take place during the second long shutdown (LS2) of the LHC, currently scheduled to begin in 2018. By that time the current experiment will have accumulated data corresponding to an integrated luminosity of around 8 fb^{-1}, delivered at a levelled luminosity of 4×10^{32} cm^{-2}s^{-1}. By then the data-doubling time would be ineffective for efficient physics return unless the experiment is upgraded to handle higher luminosities and event rates. The upgraded experiment will operate at luminosities of 2×10^{33} cm^{-2}s^{-1}. Moreover, the current procedure of reading out the detector at 1 MHz after the L0 decision will be replaced by a 40 MHz readout, and the deployment of a very flexible software-based trigger running on a PC farm that will allow for significantly enhanced efficiencies, particularly for decays to hadronic final states. This change in strategy necessitates modifying the front-end electronics of essentially all the sub-detectors. In the early period of upgrade operation there may not be sufficient CPU to allow the software trigger to process all the events. Therefore it is planned to build a Low Level Trigger (LLT) that will throttle the input rate into the PC farm. This LLT will mainly rely on low level information provided by the calorimeter and muon systems, as is the case with the current L0. More information of the LHCb upgrade can be found in the Letter of Intent

(LoI) [7] and Framework Technical Design Report (FTDR) [8].

The role of the PID in achieving the physics goals of the upgraded experiment will remain critical. The expected physics performance in various measurements of interest is discussed in Ref. [9]. Furthermore, the calorimeter and muon system will continue to be essential in triggering because of their input to the LLT, and all PID systems will contribute to the decision of the software trigger.

This Technical Design Report (TDR) presents the plans for the three PID systems. The RICH upgrade is discussed in Chapter 2, the calorimeter upgrade in Chapter 3 and the upgrade of the muon system in Chapter 4.

Chapter 2

RICH system

2.1 Introduction

The RICH system of LHCb provides particle identification (PID) of charged hadrons over the momentum range 1.5–100 GeV/c. This is essential for the study of hadronic final states and central to the physics goals of the experiment, to make precision measurements of CP violation and rare decays of b and c hadrons. There are several examples; two-body hadronic B^0 and B_s^0 decays to $\pi^+\pi^-$, $K^+\pi^-$ and K^+K^- final states have overlapping peaks in invariant mass which require PID for them to be cleanly separated. Multibody final states such as $B_s^0 \to \phi\phi$ with $\phi \to K^+K^-$ would have severe combinatorial background without π–K separation. PID at the lower end of the momentum range is required for particle-antiparticle tagging, which relies on the identification of b (and $\bar{b}$) hadrons from their decay to charged kaons via the $b \to c \to s$ decay chain. Also, efficient identification of protons with the RICH system for example facilitates the study of heavy-flavour baryonic states.

2.1.1 Overview of the current RICH system

The current RICH system comprises two detectors with three Cherenkov radiators, shown in Figs. 2.1, 2.2(a) and 2.2(b), and described in detail in the original RICH TDR [10]. RICH 1 combines two radiators, silica aerogel and C_4F_{10} gas, and is located upstream of the spectrometer dipole magnet. It covers an angular acceptance of 25–300 mrad. The RICH 2 detector has a CF_4 gas radiator, located downstream of the magnet, covering the angular acceptance 15–120 mrad. RICH 2 is responsible for the high momentum coverage, since such tracks tend to be produced at low angles. The current RICH system is described in detail in Ref. [11], and its performance in Ref. [12].

2.1.2 The LHCb upgrade

The LHCb upgrade has been described in detail in Ref. [7] and Ref. [8]. Its main aim is to enable the experiment to run at an increased operating luminosity of $2 \times 10^{33}\,\mathrm{cm}^{-2}\mathrm{s}^{-1}$. This is only possible if the current bottleneck in the trigger is removed, namely the first hardware level (the so-called "Level-0") that reduces the LHC bunch-crossing rate to 1 MHz for readout of the full detector. As a consequence, the detector will instead be read out at the full 40 MHz bunch-crossing rate in the upgrade. The decision on whether to retain the event will be taken by

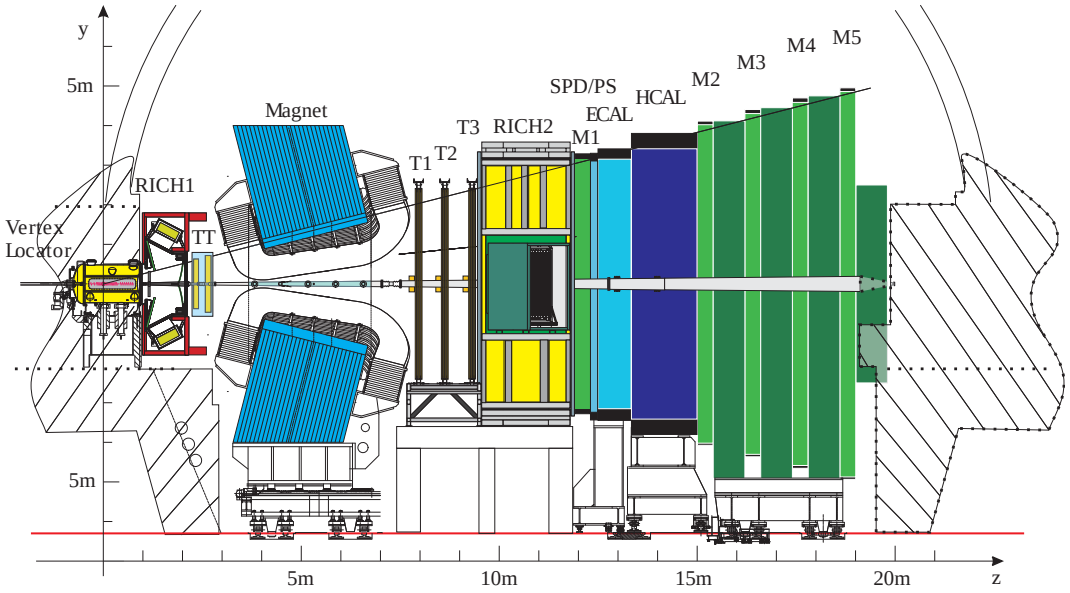

Figure 2.1: Layout of the current LHCb detector, viewed from the side, with the two RICH detectors visible upstream and downstream of the dipole magnet.

a flexible software trigger running in a large CPU farm. PID will be an important component of the software trigger, and RICH information will be used there.

The overall structure of both RICH detectors will remain unchanged in the upgrade, however with significant modifications to RICH 1. The current aerogel radiator gives a sparse number of detected photons per track, spread over large ring images, and has been found to be of reduced effectiveness at high luminosity [7]. The gain achieved by removing its material ($\sim$3.5% of X_0) has been found to outweigh the improvement in PID and therefore the aerogel will be removed. This will liberate space in RICH 1, where approximately one third of the current photon detector area is dedicated to the aerogel images. The removal of the need to detect large-radii aerogel rings has also influenced a new RICH 1 design, where the optics have been modified to spread gas rings over the full detector plane. To recover the low-momentum PID requirements, for example to improve the flavour tagging performance, a time-of-flight system ("TORCH") is actively under study, and is reported in Appendix 2.7.

A second major consequence of the upgrade strategy for the RICH system is that the photon detectors must be replaced, since the current hybrid photon detectors (HPDs) have their 1 MHz read-out electronics encapsulated within the tube. It is proposed to replace the HPDs with commercial multianode photomultipliers (MaPMTs) with external readout electronics. The baseline tube is the 1-inch Hamamatsu R11265. As a possibility for reducing the total number of MaPMTs in the regions of RICH-2 requiring lower granularity, the recently developed "flat panel" 2-inch H12700 MaPMT will also be evaluated. Alternatively a lens system may be used there, to re-focus the Cherenkov images onto the 1-inch tubes and thus reduce the number of tubes required. An adaptation of the HPD, but with external readout electronics, is under study as an alternative photon detector. This development is reported in Appendix 2.8.

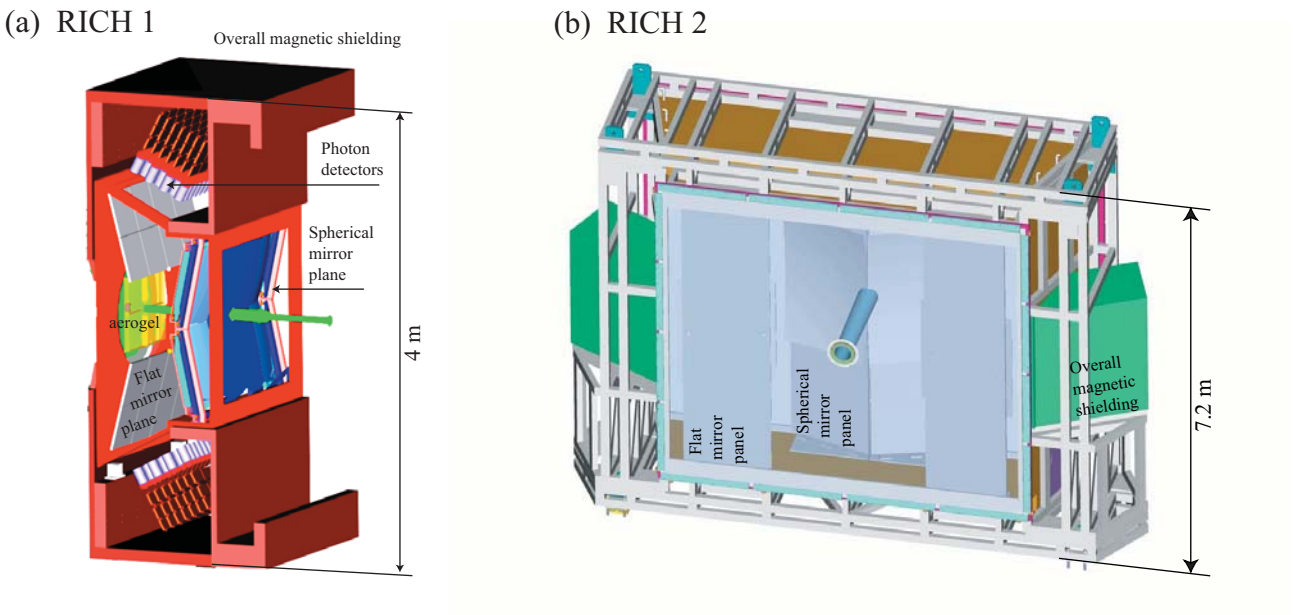

Figure 2.2: Schematic layout of the current RICH detectors: (a) RICH 1, (b) RICH 2. The overall structure of both detectors will remain unchanged in the upgrade, although the photon detectors will be replaced for both, as will the optical system in RICH 1.

2.1.3 Evolution of the RICH design

In addition to replacing the photon detectors and their associated readout electronics, studies have been made of possible alternative geometries for the upgraded RICH system. The combination of both remaining radiators in a single detector (located in the RICH 2 position) had the potential advantage of removing RICH 1 from the centre of the tracking system [13]. However, this was found not to give a decisive advantage for the tracking or trigger, and would have involved the replacement of RICH 2, for which the mechanical structure could otherwise be maintained in the upgrade.

A second series of studies involved a modified RICH 1, where a high peak occupancy of the photon detectors is expected at the increased luminosity of the upgrade. Studies were made of extending the vertical size of the RICH 1 vessel [14] by excavating into the floor, but this would have caused difficulties with the tight installation schedule during LS2. Furthermore, the substantial magnetic shielding that has been developed for the photon detectors in the current RICH 1 vessel, visible in Fig. 2.2 (a), has a significant impact on the fringe field of the spectrometer dipole magnet. Modification of that shielding would require significant studies to ensure there was no negative impact on the tracking or trigger, plus it would have involved lengthy civil engineering.

The decision was therefore taken to retain the current two-RICH layout, as will be described in this document. For RICH 2, the only major change is that of the photon detectors, electronics and mechanical mountings. For RICH 1, the aerogel will be removed, and the optical system replaced to increase the image area of the Cherenkov rings and hence reduce the peak occupancy. This will be achieved within the existing magnetic shielding structure. Wherever possible, services (high and low voltage supplies, cooling and gas systems) will

be re-used for both RICH detectors. Simulation studies have demonstrated that this strategy will allow the excellent current PID performance to be maintained at the increased luminosity.

The outline of this Chapter is as follows. Section 2.2 describes the specifications of the upgraded RICH system and the associated design considerations. Section 2.3 discusses the current status of R&D of the various major components of the RICH system: photon detector, electronics and optical systems, including preparations during LS1 of installing system components into the current RICH 2 detector. The detailed technical design of the RICH system is then described in Sect. 2.4. The simulated performance of the upgraded RICH system is presented in Sect. 2.5, including the effects of the photon detector and optical geometry. The expected PID performance is also described. Section 2.6 discusses the project organization, including the schedule, plans for installation and commissioning, costs and division of tasks between the international collaborators. Finally, the TORCH time-of-flight detector and the back-up HPD photon detector development are discussed in Appendices 2.7 and 2.8, respectively.

2.2 Specifications and overview

In this section the principal features of the upgraded RICH detectors are described, and the primary parameters listed, with a focus on the changes compared to the current detectors.

2.2.1 Design considerations

RICH 1 is required to cover the full LHCb angular acceptance, so to reduce its physical size it is placed upstream of the spectrometer magnet. The focusing of Cherenkov light is accomplished using spherical mirrors, tilted to bring the image out of the spectrometer acceptance. The light rays are again reflected using secondary plane mirrors to focus the ring images on the photon detectors, located above and below the beam, in a region where they can be shielded from the B-field of the spectrometer magnet. The angular acceptance of 300 mrad (horizontal) $\times$ 250 mrad (vertical), and the optical system, result in a RICH 1 gas vessel with dimensions approximately $2 \times 3 \times 1\,\mathrm{m}^3$.

RICH 2 has a reduced angular acceptance of 120 mrad (horizontal) and 100 mrad (vertical). It is located at around $z \sim$10 m along the beam with overall dimensions approximately $7 \times 7 \times 2\,\mathrm{m}^3$. As for RICH 1, Cherenkov images are reflected by a tilted spherical mirror and again by a flat secondary mirror onto the detector planes, which for RICH 2, are mounted on the detector sides.

As described in Sect. 2.1, RICH 1 was originally designed to cover the momentum range $\sim 1.5 - 50\,\mathrm{GeV}/c$, but has been re-optimized for the higher LHC luminosity by removing the aerogel radiator, used for low momentum ($\sim 1.5 - 10\,\mathrm{GeV}/c$) particles. The single radiator medium of C_4F_{10} gas remains, with an increased average path length of $\sim$110 cm. The refractive index for the produced Cherenkov radiation is $n = 1.0014$ and this provides for $\pi-$K separation up to about $50\,\mathrm{GeV}/c$.

RICH 2 contains CF_4 gas with refractive index $n = 1.0005$, providing a path length of around 167 cm. Within the angular acceptance, $\pi-$K separation is extended to $\sim 100\,\mathrm{GeV}/c$.

The principal characteristics, including saturated ($\beta = 1$) Cherenkov angles and threshold momenta for pions and kaons, are listed in Table 2.1 for each of the two radiators.

The resolution of the reconstructed Cherenkov angle for both RICH detectors has the following contributions:

Table 2.1: Characteristics of the radiator materials used in RICH 1 and RICH 2, respectively.

Parameter	C_4F_{10}	CF_4
L [cm]	∼110	167
n	1.0014	1.0005
θ_c^{max} [mrad]	53	32
$p_{thresh}(\pi)$ [GeV/c]	2.6	4.4
p_{thresh}(K) [GeV/c]	9.3	15.6
p_{thresh}(p) [GeV/c]	17.7	29.7

Table 2.2: Contributions (expressed in fractions of a radiation length) to the material in RICH 1 and RICH 2, which fall within the LHCb acceptance.

Item	RICH 1	RICH 2
Entrance window	0.001	0.014
Gas radiator	0.026	0.017
Mirror	0.015	0.079
Exit window	0.006	0.014
Total (X_0)	0.048	0.124

- *Chromatic:* The variation of the refractive index of the radiators with photon energy causes a spread of the Cherenkov angles of the photons produced by each track.
- *Emission point:* Aberrations of the focusing mirror and its tilt lead to a distortion of the true focal plane and hence Cherenkov angles reconstructed at the detector plane appear with a spread. The engineering constraints also may require the detector plane to be slightly offset from the best focal plane, contributing a similar spread. During Cherenkov ring reconstruction, all photons are treated as if emitted from the mid-point of the track through the radiator, which also contributes to smearing of the reconstructed angle.
- *Pixel:* This contribution is due to the finite granularity of the pixellated photon detector.
- *Tracking:* This contribution is due to errors in the reconstructed track parameters, relevant when defining the track position from which the photons are emitted.

The contributions obtained from simulations for the upgraded and current RICH systems are compared in Sect. 2.5.

The removal of the aerogel radiator in RICH 1 has reduced the total material budget from $\sim 7.6\%$ to $\sim 4.8\%$ radiation lengths, whilst the RICH 2 contribution remains at ∼12.4%. The contributions to the total are given in Table 2.2.

2.2.2 Photon detectors

The photodetectors must be sensitive to single Cherenkov photons in the wavelength range from 200 to 600 nm. A good spatial resolution is imperative, and the pixel size should not exceed 3×3 mm^2 in central regions with high occupancies. For good reconstruction, a negligible cross-talk between neighbouring pixels and negligible dark current with respect to the signal rate

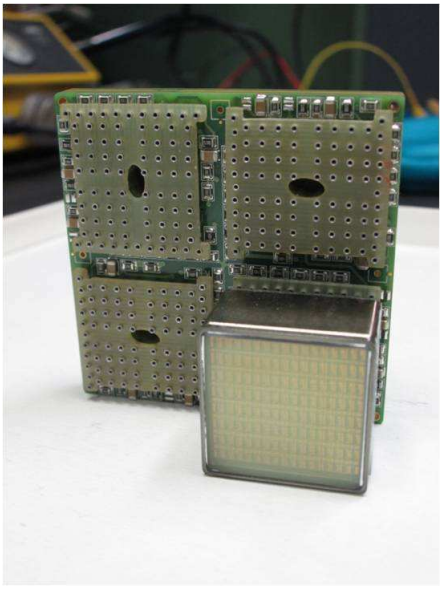

Figure 2.3: A photograph of an R11265 MaPMT, installed into a custom 2×2 socket developed for the RICH upgrade.

are also required. In addition to that, the photodetectors must not be affected by magnetic field fringes of up to 3 mT (30 G).

The baseline photon detector for the RICH upgrade is the R11265 MaPMT from Hamamatsu[1]. The photon detectors must cover a total area of 3.7 m^2, comprising 1.6 m^2 in RICH 1 and 2.1 m^2 in RICH 2. For full detector-plane coverage, the number of MaMPTs required is 1920 in RICH 1 and 2560 in RICH 2. The backup photon detector is a customised HPD with external readout, described in Appendix 2.8.

The R11265 MaPMT is a 26.2 mm square device, with 64 (8×8) pixels and a 0.8 mm thick UV/borosilicate entrance window. The MaPMT, shown in Fig. 2.3, has a SBA/UBA (super/ultra bi-alkali) photo-cathode and 12 stages of dynodes. The minimum active area covered by the photocathode is 23 mm×23 mm, giving a geometrical acceptance for each tube of 77%. The typical gain with a standard voltage divider, optimized for single photon detection, is 10^6 at a 1 kV operating voltage. The quantum-efficiency (QE) is one of the main parameters characterising the quality of the detectors. The QE of the R11265 is well matched to the LHCb RICH application; the response is shown as a function of photon wavelength in Fig. 2.4. The photo-electron collection efficiency at the first dynode is ∼90%. In order to provide magnetic shielding, each MaPMT is housed inside a module of shielding material, as described in Sect. 2.4. The MaPMTs will be grouped into a module of four units (the "elementary cell") and directly plugged in to a custom 2×2 base-board, a prototype of which is shown in Fig. 2.3.

Following optimisation studies, we are confident that we can reduce the numbers of MaPMTs used in the outer regions of RICH 2. This will involve either utilizing lenses, or using a new type of MaPMT such as the H12700 whose area is about four times the R11265 and pixel dimension 2.1 times larger. However the lens setup will need to be designed and studied and the H12700

[1]Hamamatsu Photonics: `http://www.hamamatsu.com`

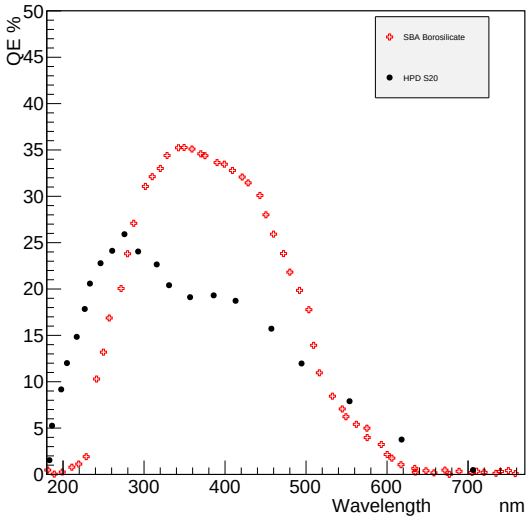

Figure 2.4: The efficiency versus wavelength for the super-bialkali photocathode and borosilicate glass entrance window of the MaPMT (red crosses) used in simulation. The QE values for a typical HPD (black dots) are also plotted.

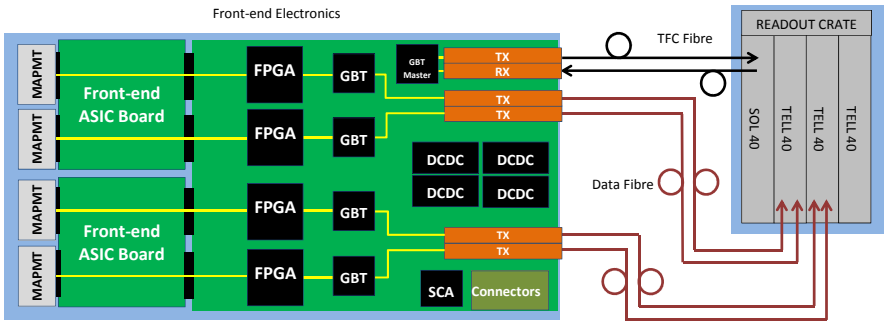

Figure 2.5: A schematic of the RICH readout system showing MaPMTs, front-end ASIC boards, digital board and TELL40s [15].

will need to be tested as the device has only recently become available on the market.

2.2.3 Readout electronics

The MaPMT readout must conform to the upgraded 40 MHz LHCb electronics architecture. An overview of the electronics readout is shown in Fig. 2.5.

The front-end chip will be an ASIC which provides MaPMT-signal shaping and amplification

Table 2.3: The expected maximum annual radiation doses in RICH 1 and RICH 2. "Low" and "High" represent the levels in the low and high radiation regions around the electronic components, respectively. The inner regions, close to the beam pipe, give an estimated average dose of ∼1 Mrad/year and 100 krad/year for RICH 1 and RICH 2, respectively.

	RICH 1		RICH 2	
	Low region	High region	Low region	High region
Neutrons : 1 MeV n_{eq}/cm^2 ($\times 10^{11}$)	4	6	1	2
Ionising radiation [krad]	7	42	1.5	4

as well as discrimination and digitisation. We are prototyping a customized readout chip, the "CLARO", tailored for the R11265, and comprised of an analogue pulse shaper amplifier and a binary discriminator. We have chosen binary readout as baseline, which is the cheapest option and minimizes the off-detector data throughput; the binary choice requires the ability to adjust channel-to-channel gain variations of the MaPMTs prior to discrimination. The readout will provide baseline recovery of the signal ideally within 25 ns, in order to suppress signal spill-over (which can give dead-time into adjacent bunches for binary readout). The CLARO prototype, described in Sect. 2.3, has been fabricated in 0.35 μm CMOS technology. The CLARO chips will be mounted on front-end ASIC cards, which are mechanically mounted to the MaPMT baseboard. The front-end electronics must be radiation tolerant up to the levels given in Table 2.3.

As a backup front-end ASIC, we are also evaluating the MAROC readout chip, again described in Sect. 2.3, which has been developed by the Omega collaboration specifically for MaPMTs [16]. The MAROC has a significantly longer peaking time (15 ns) than the CLARO (<5 ns).

Referring to Fig. 2.5, the signals from the MaPMTs feed into the front-end ASIC boards, two MaPMTs per board, and there into the digital boards. Each digital board serves four MaPMTs and it processes the data, and multiplexes them into a number of high bandwidth fibre-optic serial links. Up to four radiation-tolerant FPGAs will reside on the digital boards and will pipeline, zero-suppress and format the data for the giga-bit optical link (GBT) protocol, and also provide an interface to the Timing and Fast Control (TFC) system. The data are transmitted to TELL40 receivers [15] in the counting room, for which the firmware will be RICH specific, before being forwarded to the online computing farm for event building, filtering and storage.

We will adapt the current RICH Detector ("slow") Control system (DCS), by using the current "ELMB" boards but replacing the temperature sensors and the monitoring software. The Experimental Control System (ECS) of the current RICH system will be re-written for the upgraded detector readout, and for uploading firmware and detector parameters to the front-end cards.

2.2.4 Mirrors and alignment

Cherenkov light is focused onto the photon detector planes using tilted spherical mirrors and secondary plane mirrors. As described in Sect. 2.5, with the current RICH 1 optics, peak occupancy in the MaPMT sensors is expected to exceed ∼30% at the maximum upgrade luminosity, and thus degrade the PID performance. The optics of RICH 1 have thus been re-optimized by increasing the radius of curvature of the spherical mirrors by a factor of $\sim \sqrt{2}$, from 2700 mm to 3800 mm.

Table 2.4: The spherical and flat mirror properties for the current RICH 1, and the specifications for the upgrade. The reflectivity value is averaged over $200 - 600$ nm.

	Spherical RICH 1 current	Spherical RICH 1 upgrade specs	Flat RICH 1 current	Flat RICH 1 upgrade specs
Dimensions x [mm]	835	750	347.5	370
y [mm]	640	650	380.5	440
Area [m^2]	2.1	2.0	2.1	2.6
Thickness [mm]	33	33	8.0	6.0
Radius of curv. [mm]	2710	3800	$> 6 \times 10^5$	$> 6 \times 10^5$
Spot-size D_0[mm]	1.2	<2.5	<2.5	<2.5
Reflectivity	90%	$\geq 90\%$	90%	$\geq 90\%$
X_0	1.2%	$< 2\%$	–	–
λ_I	0.6%	$< 1\%$	–	–

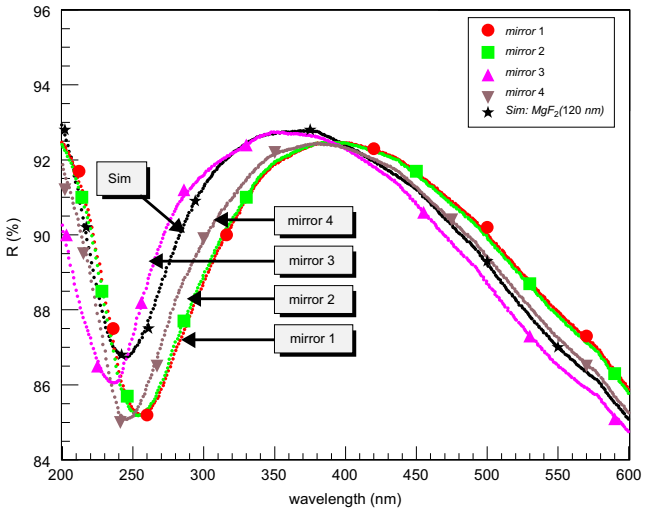

Figure 2.6: Reflectivity curves of "witness" samples for the RICH 1 four mirrors, and the simulation, as function of the photon wavelength.

The position and orientation of the spherical and flat mirrors have thus been modified accordingly within the geometrical constraints.

The RICH 1 mirror surface is segmented into four rectangular quadrants each of size 750 mm×650 mm. The baseline technology for the new RICH 1 mirrors is proven, and is the same as in the current RICH detector, described in the TDR [10]. The spherical mirrors are in the LHCb acceptance are thus made of a thin light-weight carbon fibre composite, segmented into four sections. Figure 2.6 shows the typical reflectivity as a function of photon wavelength for the spherical mirrors. The flat mirrors, outside the LHCb acceptance, are made of SIMAX glass. the mirrors are further described in Sect. 2.4. The RICH 1 spherical and flat mirror properties are given in Table 2.4.

The angular resolutions of the RICH detectors rely on the alignment of their optical compo-

nents. The precisions in reconstruction of the Cherenkov angle are about 0.88 mrad in RICH 1 and 0.5 mrad in RICH 2, respectively. The aim is therefore to maintain alignment errors significantly below these values. Guided by the current RICH detectors, the alignment of the optical components will be achieved in stages. First an *in situ* survey of all mirrors and photon detectors will be performed to a level of < 0.5 mrad in RICH 1, while no further alignment is required for RICH 2. Final alignment parameters will be extracted from data. By reconstructing a large number of rings from $\beta \simeq 1$ tracks in which the ring image is formed via reflection from an unambiguous combination of mirror segments, a precision ~ 0.1 mrad can be attained [12]. Changes to the alignment parameters over time will also be monitored.

2.3 R & D and tests of prototypes

2.3.1 Overview

There has already been an intensive programme of R&D work undertaken for the LHCb RICH upgrade. In addition, the current RICH detectors have demonstrated a reliable proof of principle for the now-established technologies:

- A full characterisation of the Hamamatsu R11265 MaPMT for the RICH application, including gain uniformity, dark count, lifetime and magnetic field sensitivity.
- R&D and characterisation of the CLARO chip, including pulse shape, cross-talk and radiation tolerance.
- The characteristics of the C_4F_{10} and CF_4 gas radiators, the photon yield and chromatic properties.
- The optical characteristics of the flat and spherical mirrors and the stability of their supports, plus the methods used for measuring them.

A summary of the above technologies is described in this Section.

2.3.2 Characterisation of the Hamamatsu R11265-103-M64

Three different tubes made by Hamamatsu have been considered and their performance compared:

- The H9500, rejected due to a non-negligible crosstalk between pixels [17];
- The R7600-03-M64 which gives good performance for single photon detection and meets LHCb requirements [18];
- The R11265-103-M64 MaPMT, that is similar to the R7600-M64 but has an improved detection area.

As described in Sect. 2.2, the baseline candidate, the Hamamatsu R11265, is a 64-channel (8×8) pixel device of active area 23×23 mm^2, a pixel size of approximately 2.9×2.9 mm^2 and a small inactive area at the border of the device. The total active area coverage is 77%, thus allowing the upgraded RICH to be designed without using lenses in front of the photosensitive plane (unless where a reduction in the localized number of tubes is desirable). The MaPMT

square cross-section geometry allows close packing of approximately 90%, providing a good active area coverage.

Unless otherwise stated, the R11265 MaPMT is read out by commercial wide-bandwidth current feedback operational amplifiers and the signals are acquired and recorded with a Tektronics DPO7254 fast oscilloscope. During the measurements the MaPMT pixels are covered with a black mask and black tape. A commercial blue LED is biased with a small current and only a few photons are generated. An optical fibre is positioned laterally to the LED allowing single photons to be sampled by a single pixel of the MaPMT.

(i) Gain variation, dark counts and cross-talk

The first measurements aim at testing and comparing the MaPMT gain, anode uniformity and dark counts with the Hamamatsu datasheet at different bias voltages. During these tests we use the standard bias divider with a 2.3-1.2-1-...-1-0.5 ratio from the first dynode to the last. All of the observed channels exhibited a clear single-photon response, demonstrated by the comparison between single-photon spectra of different pixels in Fig. 2.7. A channel-to-channel gain variation up to a factor of 2.3 is measured, which matches the specifications given by Hamamatsu. In the final configuration the gain-variation effects will be corrected channel-by-channel by the front-end electronics readout and MaPMT-to-MaPMT by the bias voltage supply. The pulse height spectra and the measured gain as a function of HV for a sample of MaPMTs is shown in Fig. 2.8(a).

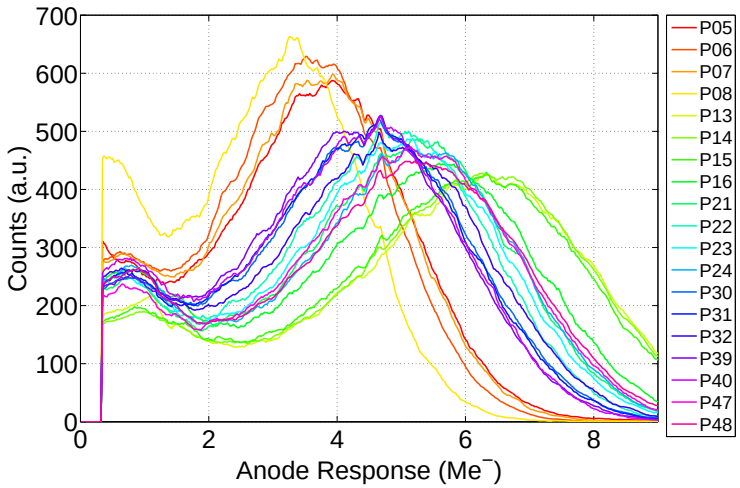

Figure 2.7: The single-photon spectra for a selection of pixels.

We have tested a different bias divider with a 2.8-1.5-1-...-1-1.3-3.3-0.5 ratio where the voltage at the first stage is increased to generate larger signals at the first multiplication stage, helping to improve the signal to noise ratio. Typical pulse-height spectra are shown in Fig. 2.8(b).

The photodector dark current is measured at room temperature by recording the events above a threshold of 300 ke^-. Five MaPMTs have been tested in similar condition and showed the same behaviour. The rate of dark current is below 3 Hz per pixel, or about 40 Hz/cm^2, for almost all anodes. Only a few channels showed a rate slightly higher. The distribution of dark events is acquired and compared with the spectra obtained with the LED setup; the spectra are

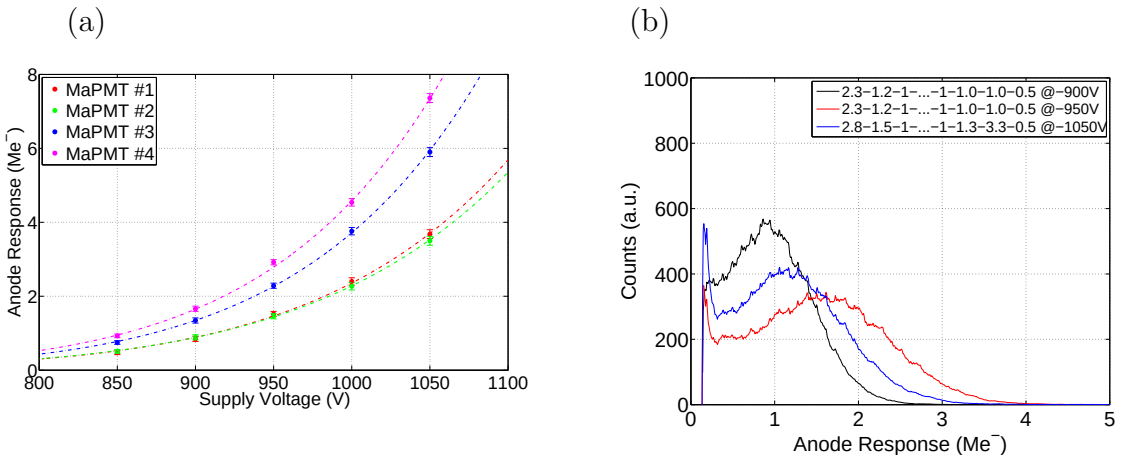

Figure 2.8: (a) The MaPMT collected charge as a function of HV for four different MaPMTs; (b) Single-photon spectra for different HV and bias divider ratios.

in good agreement.

A negligible pixel-to-pixel cross-talk is required for the RICH application. The cross-talk was measured in the R11265 by illuminating one pixel and acquiring in coincidence the surrounding pixels. The pulse heights were fitted and correlated with nearby pixels. At 800 V the typical cross-talk for neighbouring pixels is symmetric in x and y and measured at maximum 3%; for diagonal pixels the cross-talk is less than 1%. At 950 V the cross-talk reduces to less than 2% for neighbouring pixels and less than 0.5% for diagonal pixels.

(ii) Response to a magnetic field

In the LHCb RICH, the photodetectors must be insensitive to residual magnetic fields from the LHCb dipole magnet. These fields have maximum values of about 30 G in RICH 1 and 15 G in RICH 2, within the outer iron shields of the two RICHes. Such fringe fields can deteriorate the MaPMT performance through loss of gain and photo-detection efficiency, and it is therefore necessary to optimize the type of local shielding required. From our experience with R7600 tubes, the worst effects are expected when the magnetic field is longitudinal, i.e. parallel to the MaPMT axis.

The sensitivity of the R11265 to longitudinal magnetic field has been tested within a solenoid ranging from 25 G to 100 G. The behaviour of the R11265 inside the field was measured with and without shielding material. Three field configurations made of layers of 0.2 mm of a high magnetic permeability material were tested [2]: the shields protruded from the MaPMT entrance window by 0.8 cm, 1.6 cm and 2.4 cm ("Shields 1, 2 and 3", respectively, in the following discussion). The shields were wrapped around the MaPMT up to the pins; for Shield 1 the thickness of the shield was varied, each wrap adding 0.2 mm. The MaPMT was operated at 1050 V, corresponding to a gain for the 16 measured pixels of about 2.5 Me^-/photon.

Examples of the loss of gain under the influence of a longitudinal magnetic field are shown

[2]The chosen material was Skudotech^{TM}, which has a relative permeability in excess of 33000.

in Fig. 2.9, which shows the spectra obtained without shielding material for one of the most central pixels (pixel 37), and a peripheral pixel (pixel 63). It can be seen that the single-photon peak moves to lower amplitude as the magnetic field increases. Figure 2.10 shows the detection efficiency for the same two pixels (defined with respect to zero magnetic field) as a function of increasing field and different Shield 1 thicknesses. The performance is also compared to the case of no magnetic shield. Without a shield the efficiency decreases to about 95% at 25 G and to 87% at 50 G for the central pixel and to about 35% at 25 G and to 20% at 50 G for the periphery of the tube. Therefore, without any local shielding, in some areas of the photo-detector plane the fringe field will prevent the observation of a single photon peak for the peripheral MaPMT pixels. However the performance can be almost completely restored by the addition of up to three wraps of shielding, which significantly reduces the spectrum distortion and loss of gain. For three wraps of shielding (0.6 mm thickness) in the Shield 1 configuration, at 50 G the efficiency stays close to 100% for both central and perhipheral MaPMT pixels, and stays above 90% for two wraps of shielding (0.4 mm thickness). The effect of adding more than a single wrap is more effective than increasing the protrusion.

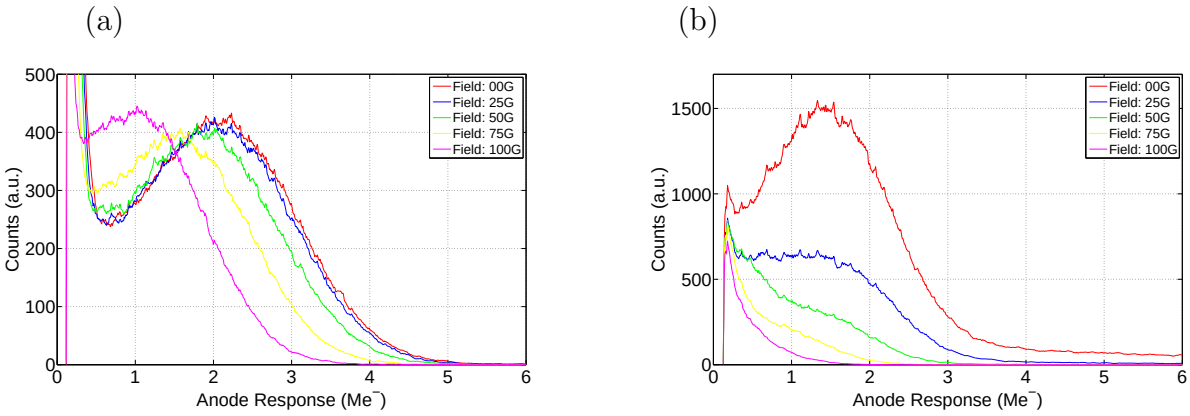

Figure 2.9: Pulse-height spectra of (a) the central pixel 37 and (b) the peripheral pixel 63 for varying magnetic field strengths, without any shield.

Longitudinal field effects have also been studied at a second test site with a different MaPMT, and the same magnetic field effects are observed qualitatively. However the tests indicate that the intrinsic variation of magnetic tolerance between tubes could be significant, although well within the RICH 1 operating limits if shields are used.

The sensitivity of the R11265 to transverse magnetic fields has been studied using a similar setup to that described in [19]. The efficiency, defined as the number of events above threshold in the presence of a magnetic field compared to zero field, is shown as a function of field strength in Fig. 2.11. This is shown for the two possible transverse field orientations relative to the entrance window slits. It can be seen that the R11265 exhibits different behaviour for the two orientations and is less robust than the R7600 series. At the lower operating voltage and at the worse field orientation, the MaPMT maintains an efficiency of above 90% for fields less than 40 G, significantly beyond the field strengths expected in the LHCb experiment. These magnetic measurements are ongoing.

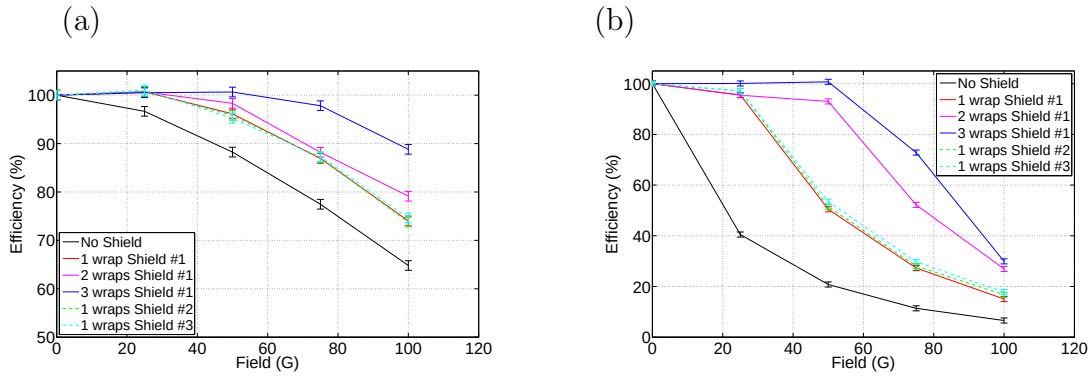

Figure 2.10: The efficiency relative to zero field for (a) the central pixel 37 and (b) the peripheral pixel 63 as a function of magnetic field strength, with the MaPMTs mounted in different thicknesses of Skudotech shields. (The descriptions of Shields 1, 2 and 3 are given in the text.)

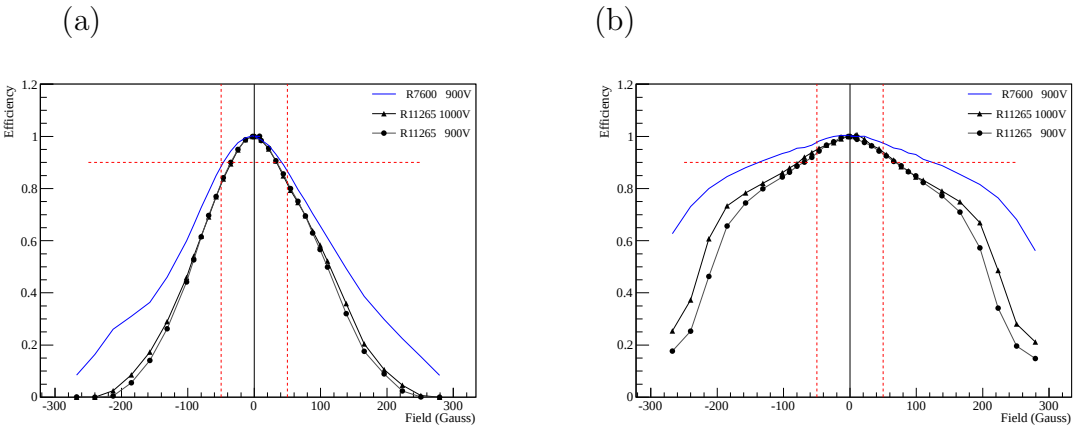

Figure 2.11: Efficiency versus transverse magnetic field strength of the R11265 MaPMT for 900 V (circles) and 1000 V (triangles) operating voltages compared to the previous generation R7600 (solid blue line). The plots are for the cases where the magnetic field is orientated (a) parallel and (b) perpendicular to the entrance window slits of each pixel, respectively.

(iii) Ageing measurements

A long period of exposure to photons may deteriorate the MaPMT performance through wear of the dynodes, ageing of the photocathode, or an increase of dark current. Ten pixels of a R11265 were illuminated with a commercial blue LED emitting single photons over a several-month period. A schematic of the illuminated pixel map is shown in Fig. 2.12. Two reference pixels were also tested with a very low current of a few tens of nA. In order to ensure the current stability, the LED bias voltage was measured every five minutes and was adjusted to keep the current stable to 0.5 μA in the pixel used as reference. The gain was kept stable at about 2×10^6 (this is the gain for the specific MaPMT under test; typical MaPMT gains can have lower values),

corresponding to an operating voltage of $\sim$ 875 V.

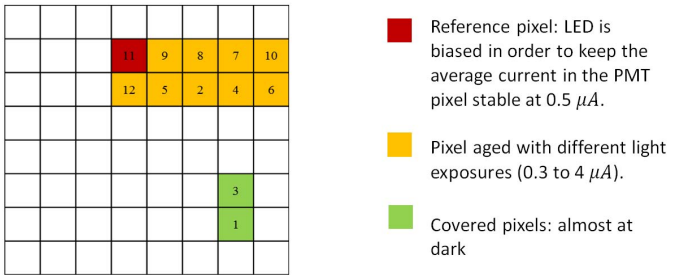

Figure 2.12: A front view of the anode indicating the reference channel and the measured pixels.

Three different measurements were performed:

- The LED measurement, in which the gain loss was measured from the peak position of the single photon spectrum. The corresponding occupancy values ranged from 2.4% to 34%, which should be compared to the occupancy level foreseen for the most illuminated pixels in the LHCb RICH-1 detector ($\sim$25%).
- The noise measurement in which the LED was turned off for one hour and a dark signal was acquired, allowing measurement of the dark-count stability.
- A source measurement made once per month, in which ageing effects of the photocathode efficiency was determined. In this case, the LED was turned off and a ^{232}Th γ-source was placed in front of a PbF_2 crystal, producing Cherenkov photons.

Figure 2.13 shows the relative gain loss as a function of LED illumination time for four of the twelve pixels measured. After the first 200 hours of illumination, the gain loss of all ten pixels under study exhibit a similar rapid fall during a "settling time", by about 10% -15%. After about 1500 hours of illumination, the gain loss plateaus at typically 35%. Interestingly, a loss of gain is also observed for the two reference pixels operating at low illumination, but which exhibit a loss of less than 20%. Hence we conclude that the gain loss does not depend on the DC current nor the integrated charge on each pixel, but only on the LED illumination time. Given that the ageing seems to depend on the illumination time, the $\sim$3000-hour period under study corresponds to about two years of LHC running. In the dark-count studies, for all the measured pixels the dark counts do not show any correlation to the ageing, but only to small changes in temperature. It can therefore be concluded that the ageing does not result in any increase of the dark current.

By increasing the high voltage by 25 V, from 875 V to 900 V, the gain loss can be readily compensated. Therefore a modest increase in HV can be considered to recover any gain deterioration of the R11265 during RICH operation.

The measurements with the ^{232}Th source demonstrated a constant photoelectron production rate. Hence no deterioration of the photocathode efficiency has been observed.

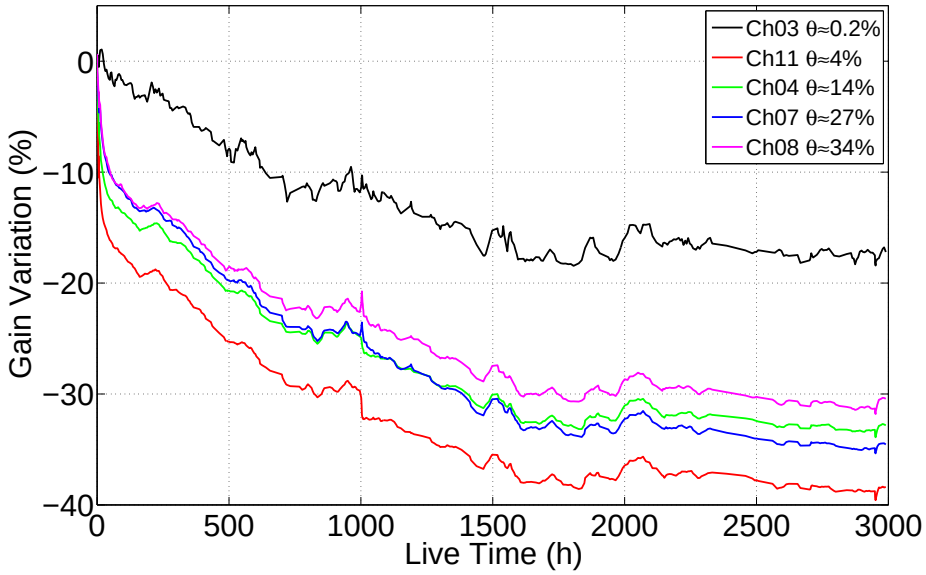

Figure 2.13: The relative gain variation at 875 V versus the LED exposure time for four of the illuminated pixels. The reference pixel operating at low current is shown in black (upper curve). Θ indicates the corresponding level of occupancy in a specific channel.

2.3.3 Electronics

(i) The CLARO chip

A general introduction to the CLARO front-end readout chip was given in Sect. 2.2. Table 2.5 lists the measured properties of the 4-channel prototype CLARO. The reader is referred to Ref. [20] for a detailed description of the CLARO circuit configuration and the measured performance.

CLARO chip Characteristics

A schematic diagram of the single channel of the CLARO is shown in Fig. 2.14. The preamplifier is a current amplifier having a common-base input stage. The CLARO gain is settable on a channel-by-channel basis with 3 bits. A comparator follows the preamplifier and generates the binary output of the channel. The per-channel threshold of the comparator is also adjustable with 5 bits. The gain of the preamplifier and the comparator threshold are set by means of a switch system that affects the bandwidth and power consumption of the chip only very marginally. The gain and threshold settings are stored in a register that can be accessed through a Serial Protocol Interface, SPI. The gain and the threshold settings need to be managed only occasionally and, therefore, the digital part of the chip does not need to be fast. This has two important benefits: digital signals are not present close to the preamplifier inputs during data acquisition, and redundancy can be easily implemented to obtain robustness against radiation.

The pixels of the MaPMT are arranged in a 8×8 matrix with a pitch of about 2.5 mm. The choice of 8 channels for each CLARO was made to match the MaPMT geometry. This approach has two advantages. Firstly the inputs of the CLARO can be placed close to the pixels,

Table 2.5: Specifications and performance of the CLARO chip.

Parameter	**Measured**
Speed, analogue path	< 5 ns peaking time, < 25 ns recovery time
Speed, binary output	< 5 ns rise time, < 25 ns recovery time, (time over threshold)
Noise vs input capacitance (<50 ke$^-$ RMS)	(5 + 1/pF) ke$^-$ RMS
Power dissipation per channel vs hit rate	(0.7 + 0.1/MHz) mW in "low power" mode (1.5 + 0.1/MHz) mW in "timing" mode
Supply voltage	2.5 V
Cross talk vs inter-pixel capacitance (<10%)	(0.1 + 4/pF)% in "low power" mode (0.1 + 2.5/pF)% in "timing" mode
Gain setting	3 bits per channel
Threshold setting	5 bits per channel
Communication protocol	SPI
Robustness to neutrons 1 MeV-equivalent (6.6×10^{12} n_{eq}/cm^2 in 10 years)	Measured to $>10^{14}$ n_{eq}/cm^2 (about 160 LHCb equivalent years)
Robustness to total ionizing dose (400 krad in 10 years)	Measured with Xrays to > 4 Mrad (about 100 LHCb-equivalent years)
Package	8 channels/chip, QFN56
Technology	0.35 μm CMOS (AMS, consumer)

minimizing reciprocal interference (see Sect. 2.4 for the structure of the assembly). Secondly, the engineering time and manpower required for the realization of the monolithic chip are reduced. The disadvantage is the necessity to test a large number of chips (>35k) and the corresponding front-end ASIC boards.

We selected the 0.35 μm CMOS technology [3] that is very stable and widely used in the consumer field, with a production line expected to be active for at least the next 10 years. The irradiation environment in the RICH and the design criteria guarantee an adequate radiation tolerance (see below). The speed of response is one of the major design criteria and we can see in Fig. 2.15(a) that the recovery time of the input preamplifier is within 25 ns, suppressing spillover. Here the data have been downloaded from the scope from the 4-channel prototype and it can be seen that the peaking time is shorter than 5 ns. The small undershoot following the signal has a short (55 ns) time constant, and will not impact the performance even in the high occupancy regions. This feature will be however optimized in the final CLARO chip with respect to the present prototype.

The signals at the binary output of a CLARO channel in response to typical signals from the MaPMT are shown in Fig. 2.15(b). The rise time is a few ns, while the width depends on the input amplitude which allows for a time over threshold measurement. Again the recovery time of the pulse is shorter than 25 ns for a one-photon signal amplitude.

[3] From Austria Micro Systems (AMS).

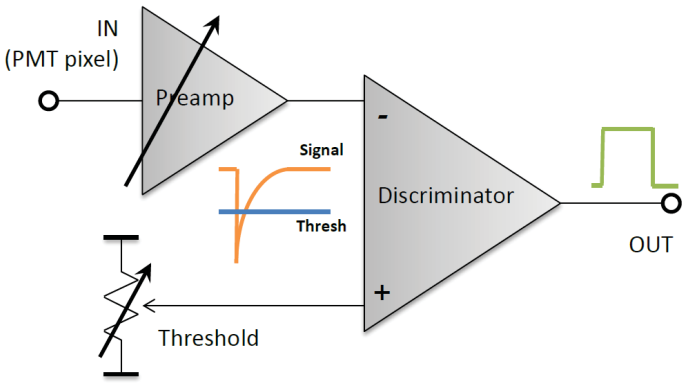

Figure 2.14: A schematic diagram of a single channel of the CLARO chip.

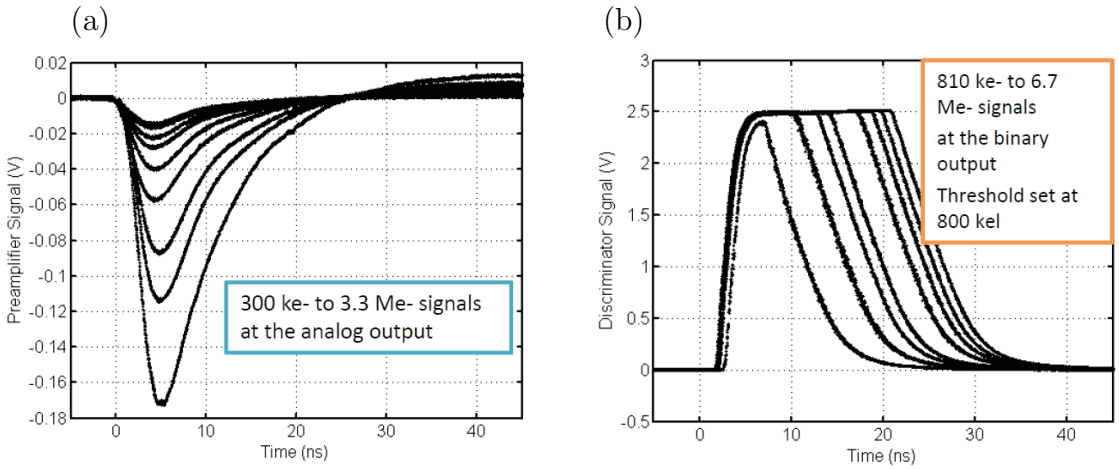

Figure 2.15: (a) Analogue signals measured at the auxiliary output of the in response to injected charges simulating single photons, downloaded from a DCA-X 86100 sampling scope from Agilent (this output is available only for diagnostic purposes). (b) Binary output signals in response to an input charge emulating a range up to more than two photons. The width of the pulses extend beyond 25 ns only for input signals above single photons.

One very important design criterion is to minimize cross-talk at this high speed of response. A small parasitic capacitance present between the inputs of two channels becomes responsible for the injection of cross-talk signals, as can be seen in Fig. 2.16. The two curves of Fig. 2.16 correspond to the two modes of the input stage of the preamplifier: the "low power" mode, optimized for low power consumption (0.7 mW per channel), and the "timing" mode, optimized for higher speed and lower input impedance (1.5 mW per channel). As can be seen, and also listed in Table 2.5, the slope of the cross-talk signal is roughly inversely proportional to the power dissipation. The compact design of the CLARO results in a parasitic cross-talk capacitance less than 1.5 pF.

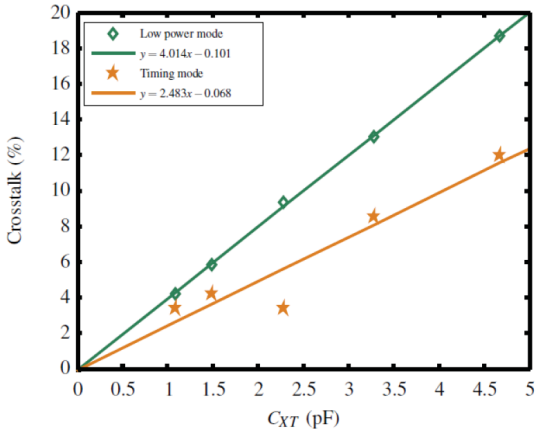

Figure 2.16: Cross-talk signal versus capacitance between adjacent pixels in the "low power" mode and the "timing" mode.

The digital section of the CLARO chip allows the configuration of each CLARO channel such as channel enable, and gain and threshold settings, both of which have configurable digital to analogue converters (DACs). These settings are stored in registers protected by Triple Modular Redundancy (TMR). Some configuration bits are also foreseen to control global diagnostics. The main design considerations for the CLARO configuration register are that it must have no free running clock and that it can be programmed by the Slow Control Adapter for the CERN GBT System (GBT-SCA) [21]. In addition to the TMR protected register, which represents the long term storage for the configuration information, an auxiliary I/O shift register will receive/transmit the serial data being transferred to/from the storage register under control of the GBT-SCA. Whenever a mismatch between the three flip-flops of any TMR cell is present, the output can be monitored by the LHCb slow control system through the GBT-SCA and then cleared. Alternatively the CLARO can be configured to self-reset the Single Event Upset (SEU)-detect condition. The implementation of the CLARO programming interface described above requires a total of 13 I/O pins.

Radiation characterisation of the CLARO

Radiation-hardness tests have been performed on the CLARO chip, guided by FLUKA simulations of the expected LHCb run scenarios of the upgrade. The worst-case dose values that the electronics must tolerate are given in Table 2.3, and are located in the outer regions of RICH 1. Here the accumulated doses in a single year are 6.1×10^{11} 1-MeV n_{eq}/cm^2 and 40 krad for the neutron fluence and total ionising dose, respectively.

Irradiation with neutrons has been performed at the T2 Hall of the Louvain-la-Neuve Cyclotron, where a beam with 23 MeV peak energy and very low γ (2%), p and e^- (0.02%) contamination was delivered to three CLARO chips in a cascaded configuration. The irradiation was performed in three steps, corresponding to about 4, 40 and 160 LHCb-equivalent years (with a total cumulative fluence of $\sim1\times10^{14}$ 1-MeV n_{eq}/cm^2). The chips were biased during irradiation and the chip-bias current and threshold voltages were measured every 5 seconds in order to detect possible SEUs affecting the threshold DAC settings. An additional circuit provided protection

against Single Event Latchup (SEL). Before and after each irradiation step, a characterisation of each chip was performed by measuring so-called "S-curves" at selected thresholds: a burst of 1000 identical test pulses per data point was sent to all the CLARO inputs simultaneously, and the number of discriminated output signals was plotted for increasing input signal amplitudes. An example of such curves for the three irradiation steps (including the measurement before irradiation, labelled "Step 0") can be seen in Fig. 2.17(a). No SEU or SEL was measured during these tests. Full operation of the chip was maintained, and a threshold variation of only a few percent was measured, channel dependent (due to small differences in the design of the comparators in the prototype).

Tests for total ionising dose were performed using an X-ray machine in INFN Laboratori di Legnaro. Three CLARO chips were irradiated in three steps, corresponding to approximately 1, 10 and 100-equivalent LHCb years (a total cumulative dose of ∼4 Mrad). The same measurements described above were performed during this irradiation, and the corresponding S-curves can be seen in Fig. 2.17(b). As before, no SEU or SEL was measured for this type of irradiation, however a clear threshold variation trend was found (a drift towards lower values for channels 0 and 1, and the converse for channels 2 and 3; again due to the small variations in the comparators). Nevertheless this variation is well within the CLARO DAC range.

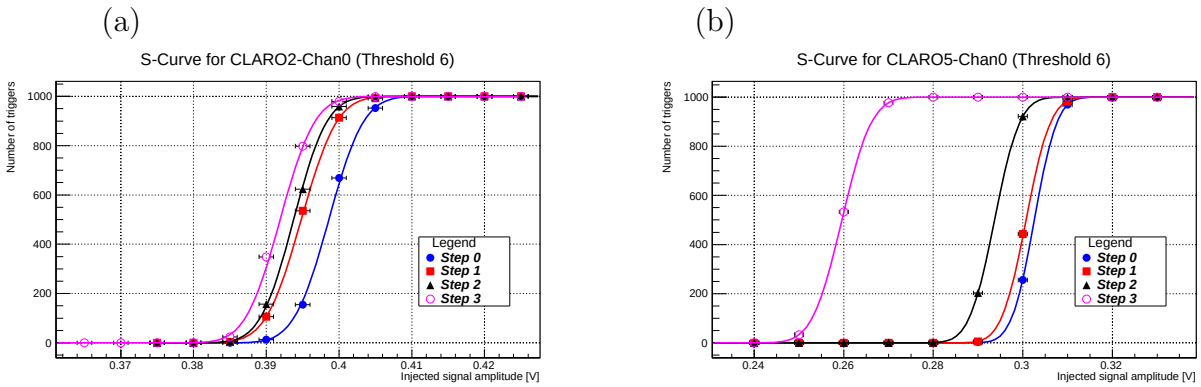

Figure 2.17: (a) Typical S-curves for CLARO2 (channel 0, DAC threshold 6) during neutron irradiation; (b) S-curves for CLARO5 (channel 0, DAC threshold 6) during X-ray irradiation.

(ii) Electronics and LS1 preparations

A programme of R&D towards the upgraded RICH front-end (FE) electronics is underway. Initial prototype modules based on the MAROC family of ASICs [22] have been designed, fabricated and operated in the laboratory. Future prototypes will build on the experience gained with this module as new elements required for the upgrade are progressively incorporated into the design.

LS1 MaPMT module

During 2014, an MaPMT demonstrator module will be installed in the existing RICH 2 detector. This module is compatible with the existing LHCb DAQ architecture and will allow

experience to be gained with the readout of MaPMTs in a realistic RICH environment, albeit at lower luminosity than at the upgrade. The module will also serve as a test-bench for studies of MaPMT performance in various lab set-ups and in future beam tests.

The module, shown in Fig. 2.18, comprises a base-board to support a 2×2 array of R11265 MaPMTs, two readout boards (one shown in photo) each with two MAROC3 ASICs (of which one visible), and a Xilinx Spartan6 FPGA, all mounted on an aluminium support structure. The support structure shown is a double-height version of the module that will be used in RICH 2 in place of a single HPD. Figure 2.19 is a schematic of where the modules will be installed in RICH 2. The space available for these modules is constrained by the existing mechanical and optical layout of RICH 2 and also the constraint of safe operation in the neighbourhood of HPDs operating at -16 kV.

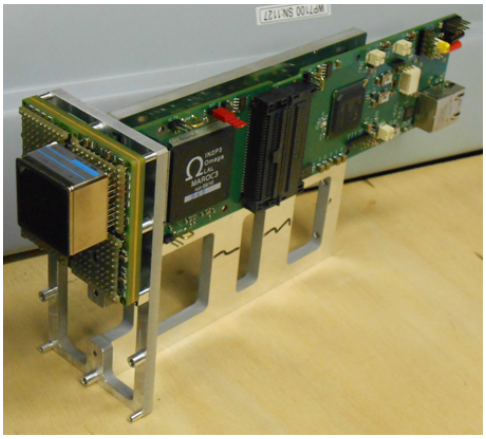

Figure 2.18: A photograph of the LS1 2×2 MaPMT module.

Production module development

The module described above will be used to validate and later to refine the electronic design of all the elements as well as the mechanical design. The GBT chipset will replace the current Gbit Ethernet 1000-BASE-T for the data and controls interface, and CERN DCDC converters [23] will replace the commercial DCDC converters currently used. The MAROC3 ASIC will be replaced with a CLARO front-end ASIC board. The FPGA will also be replaced with one that has been identified as sufficiently radiation-tolerant.

The radiation-tolerance of the front-end FPGA is an important requirement with an expected level of ambient radiation amounting to an expected 20 krad per year (40 krad worst case) at the highest luminosity. The complexity of the FE firmware precludes the use of anti-fuse FPGAs or other non-reprogrammable devices. Therefore SRAM-based FPGAs appear to be the best choice and our R&D programme will include irradiation measurements to identify a suitable device of this type. Studies will also be made on the implementation of scrubbing (periodic reconfiguration of the FPGA logic) which will need to be used to mitigate the effects of SEU.

An early demonstration of a working prototype will be essential in order to fully validate our design by rigorous testing under 40 MHz readout conditions. Such tests will require the use of new readout infrastructure (TELL40, SOL40 or their equivalent prototypes). The final step

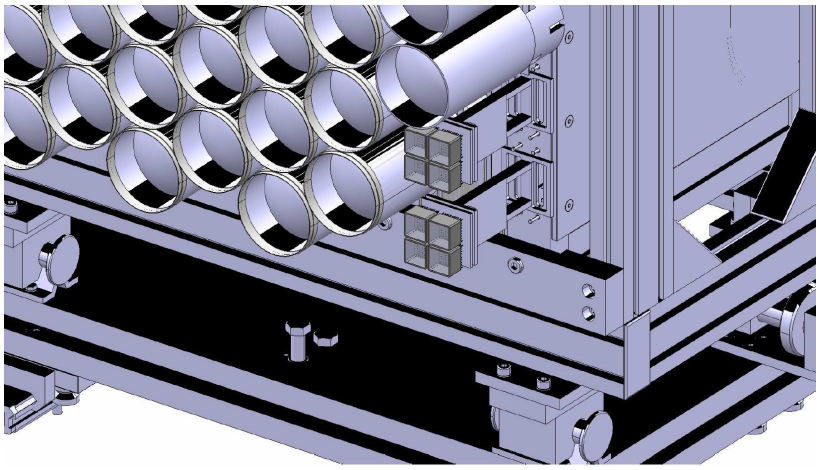

Figure 2.19: Illustration of the MaPMT module in RICH 2 to be installed during LS1.

will be to scale up the design from a 2×2 MaPMT unit to a 4×4 array and to mount the module on a prototype RICH column in order to make a final validation of the integration into the detector, including the integration of cabling and cooling.

Firmware development

The firmware requirements are more demanding than for the existing front-end. Zero-suppression will be required before data transmission in some regions of the detector, and the multiplexing and formatting of the data at the much higher event rate will also be more challenging. The required high performance combined with the need to include TMR to mitigate against SEU is expected to use significant FPGA logic resources. Studies will be performed to estimate this requirement in the coming months.

The development of an effective zero-suppression algorithm will proceed in parallel with the hardware development and can be validated in simulation and in the prototype hardware. Prototype firmware development will also be required to support the operation of the various prototype modules that will be produced during the development phase. This will provide an opportunity to test the implementation of the various DAQ and control protocols required for the upgrade.

MAROC developments

The MAROC series of ASICs, developed by the Omega CNRS-IN2P3-Ecole Polytechnique group over a number of years for the readout of 64-channel MaPMTs, is being considered as a possible backup to the CLARO. Some variants, notably the MAROC3, provide features that are close to the requirements of the LHCb RICH. A future planned development, the MAROC4, will have improved radiation tolerance through the addition of TMR to protect the configuration registers against SEU and will have faster response times that could satisfy the more stringent requirements for the upgraded RICH detector. The RICH group is therefore following these developments and is pursuing a programme of studies to evaluate the performance of these ASICs.

The MAROC4 ASIC is expected to have very similar layout, functionality and packaging to the existing MAROC3. Therefore, when these new ASICs become available, it will be possible to make a new version of the prototype module with only minor modifications to the PCB layout. Submission of the MAROC4 may be as early as December 2013, which would allow initial validation to take place in the laboratory during 2014.

2.3.4 Optics

In both RICH detectors, as described in Sect. 2.1, Cherenkov photons are reflected off a set of slightly tilted spherical mirrors inside the LHCb acceptance, and then a set of flat mirrors outside the acceptance direct the photons onto the photodetector plane. The RICH 1 spherical mirrors have been proven in the existing experiment for their lightweight properties (less than 2% X_0 and a nuclear interaction length less than 1% λ_I), their radiation tolerance, their fluorocarbon compatibility, their optical quality and structural rigidity. The existing mirror technologies therefore satisfy the upgrade's stringent requirements. Further details of mirror properties and procurement will be given in Sect. 2.4.

2.4 Technical design

In this section, the RICH 1 mechanical and optical design for the upgrade is discussed. There follows a summary of the mechanical changes that will be made to RICH 2, in particular the photon detector assembly. As the RICH 2 mechanical system is essentially unchanged, the reader is referred to the RICH 2 Engineering Design Review [24] for the structural detail. The section concludes with a description of the technical design of the electronics readout system, data acquisition and services.

2.4.1 RICH 1 optical design

The optical layout of RICH 1 has to be modified to reduce the otherwise prohibitively large hit occupancy in the central region of the detector, which leads to a degradation in efficiency of the RICH pattern-recognition algorithm. This reduction is achieved by increasing the focal length of the spherical mirrors by a factor of $\approx \sqrt{2}$, and thus halving the occupancy. An illustration of the current geometry is contrasted with the upgraded geometry in Fig. 2.20.

The change of geometry is possible without significantly increasing the area of the photon detector (PD) plane because the removal of the aerogel radiator significantly reduces the maximum ring size. However, as a consequence of the increased focal length, the PD plane must be moved further away from the beam-line, which is feasible within the current geometric constraints of the iron magnetic shielding. The increased focal length does not only reduce the RICH 1 occupancy, but also improves the Cherenkov angle resolution due to the reduced aberrations of the spherical mirrors. Moreover, based on currently understood constraints, the distance between the spherical and plane mirrors can be slightly extended in z, shown in Fig. 2.20(b). This increases the path length of tracks inside the gas radiator, giving more Cherenkov photons, and which also allows a reduction in the tilting of the spherical mirrors. This in turn further reduces the optical aberrations, and allows the PD plane to be kept closer to the beam-line.

The RICH 1 optical layout was optimised within the following engineering constraints:

- The overall real estate for RICH 1 will extend between $z = 985\,\text{mm}$ to $z = 2245\,\text{mm}$;

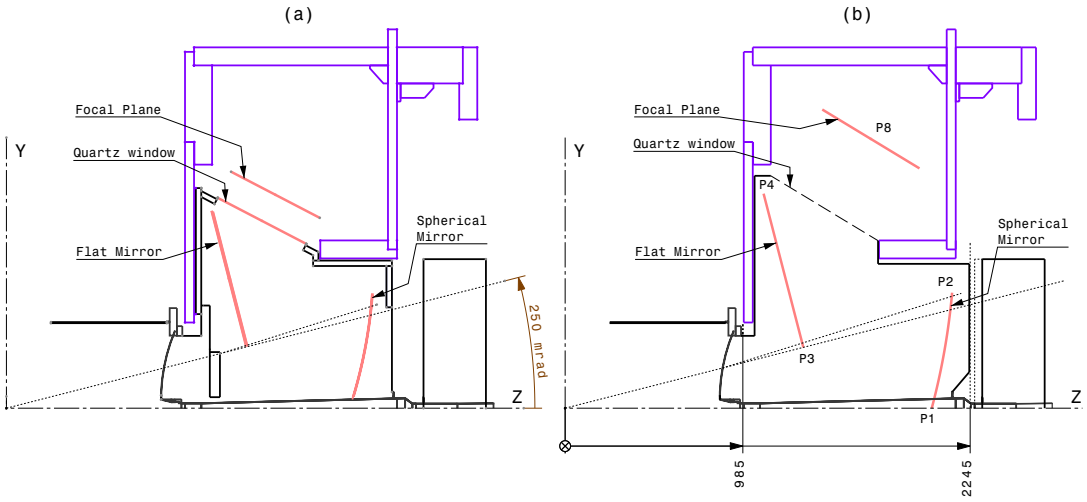

Figure 2.20: The optical geometries of (a) the current and (b) the upgraded RICH 1. The points $P(n)$ in the figure are referred to in Table 2.6.

- The region occupied by the gas radiator in z is: $\sim$900 mm $\leq z \leq$ 2150 mm (Note that the lower limit is not a fixed value, and also it extends slightly beyond the RICH 1 real-estate boundary, since the VELO/RICH interface is hemispherical);
- All the optical surfaces are limited in z by: 1100 mm $\leq z \leq$ 2145 mm;
- The maximum horizontal acceptance for particle tracks is 300 mrad (unchanged);
- The maximum vertical acceptance for particle tracks is 250 mrad (unchanged).

A realistic design has been developed [14, 25] such that the optical components and the PD assembly fits into the currently-understood engineering constraints.

(i) Optimised optical layout

The optics configuration was initially optimized stand-alone, in order to assess the optical performance and to differentiate the various contributions to the total error on the Cherenkov angle. This optimisation was carried out using a fast and flexible professional optical CAD software package[4] using a simplified geometry. Afterwards, this initial optical layout was fed into the full LHCb simulation for a complete evaluation of the system performance (see Sect. 2.5).

The tilt of the spherical mirrors is chosen to be as small as possible to minimise the contribution of emission-point error to the Cherenkov angle resolution, but just large enough to direct all photons onto the plane mirrors. The plane mirrors, located just outside the geometrical acceptance, are tilted such that the centre of the PD plane is approximately positioned to maximize the space available behind it in order to house the MaPMT electronics and services.

The geometry resulting from this optimisation process is summarized in Table 2.6. For tracks uniformly distributed inside the geometrical acceptance, the median photon incidence angle on

[4]Optica 3, `http://www.opticasoftware.com` and Wolfram Mathematica 9, `http://www.wolfram.com/mathematica`

the PD plane is $(2.50 \pm 0.12)^\circ$ and the median magnification is (1.90 ± 0.02) mm/mrad. The space available behind the PD plane for the PD assembly is about 270 mm. The photon trajectories for several simulated tracks in the initial optimisation procedure are shown in Fig. 2.21.

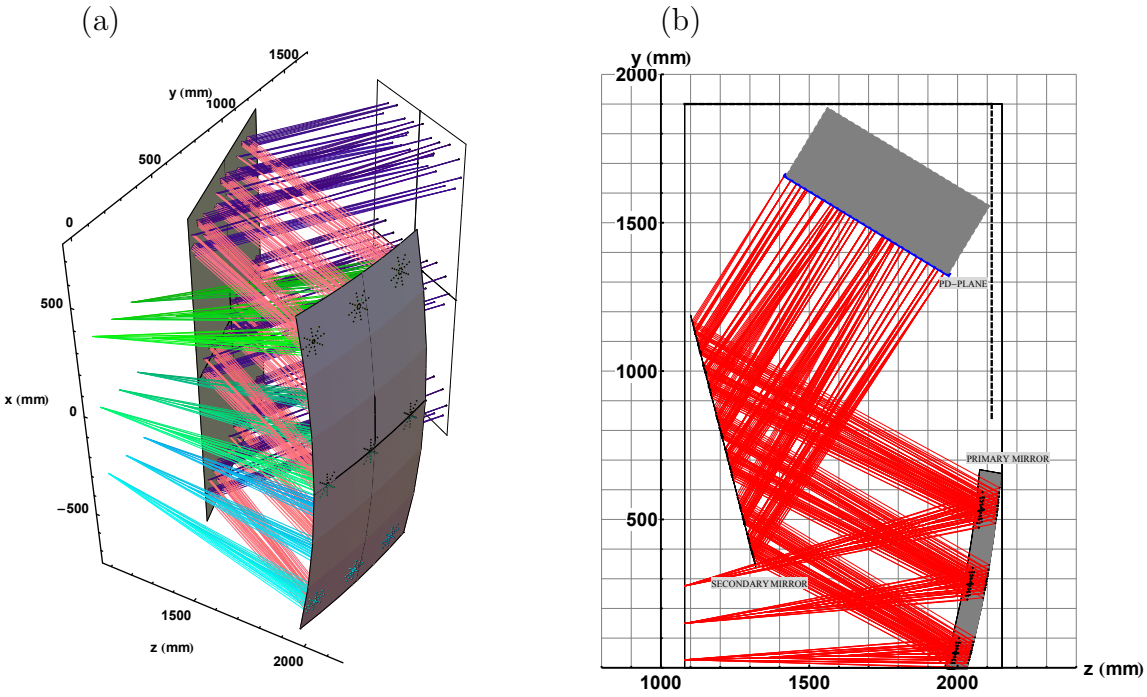

Figure 2.21: Simulated Cherenkov photons in the upper half of the upgraded RICH 1; (a) 3D view, (b) 2D view in the vertical plane.

Table 2.6: Geometrical data of the re-optimized RICH 1 optics. The points $P(n)$ are shown in Fig. 2.20.

Centre of the spherical mirror	$z = -1640$ (mm)	$y = +978$ (mm)
Point 1	$z = +2032$ (mm)	$y = 0$ (mm)
Point 2	$z = +2145$ (mm)	$y = +640$ (mm)
Point 3	$z = +1320$ (mm)	$y = +337$ (mm)
Point 4	$z = +1100$ (mm)	$y = +1189$ (mm)
Point 8	$z = +1695$ (mm)	$y = +1492$ (mm)
Axis of the spherical mirror: angle with respect to the beamline.		10.0°
Normal of the plane mirror: angle with respect to the beamline.		14.5°
Normal of the PD-plane: angle with respect to the beamline.		58.8°
PD-Assembly: x-size (full geometrical acceptance)		≈ 1380 mm
PD-Assembly: size in the $y - z$ plane (full geometrical acceptance)		≈ 630 mm

(ii) Single-photon Cherenkov angle resolution

As already discussed in Sect. 2.2.1, emission, chromatic and pixel errors contribute to the total error on the Cherenkov angle. Table 2.7 shows the different contributions to the Cherenkov angle resolution for the current RICH 1, the upgraded RICH 1, and the RICH 2 detectors. It has been shown via simulation that the three error sources sum in quadrature, confirming the naive assumption that they are uncorrelated. It can be seen that both the emission point error and the pixel size error for the upgraded RICH are smaller than for the current RICH 1 and the chromatic error is the same. The optical performance is stable for shifts/tilts of the PD plane of the order of ± 3 cm and $\pm 3^{\circ}$. The chromatic error assumes the baseline MaPMT with borosilicate glass input window. The use of UV-glass input window would increase the chromatic error up to 0.84 mrad while increasing the number of detected photons by about a third.

Table 2.7: Single-photon Cherenkov angle resolutions resulting from the optics optimisation studies for the current RICH 1, the upgraded RICH 1, and the RICH 2 detectors. As the emission point error is strongly dependent on the angle of the track, the median for a uniform angular distribution is used.

	Current RICH 1	Upgraded RICH 1	Current RICH 2
Emission Point Error	0.54 mrad	0.35 mrad	0.23 mrad
Chromatic Error	0.56 mrad	0.56 mrad	0.23 mrad
Pixel Size Error	0.62 mrad	0.45 mrad	0.20 mrad
Total Error	0.99 mrad	0.80 mrad	0.37 mrad

Effects that worsen the single-photon resolution but which are independent of the optical design are measurement errors on the particle track direction and momentum, low-momentum particle tracks, particle conversions and photon background. The estimation of the Cherenkov angle resolution in a realistic environment requires the full simulation, which is addressed in Sect. 2.5.

Finally, in case the space available for the PD-assembly is not sufficient, the layout can be modified by simply reducing the radius of curvature down to $R = 3600$ mm and shifting the PD plane closer to the beamline by $\simeq 90$ mm, resulting in errors similar to those given in Table 2.7.

2.4.2 RICH 1 mechanics

The mechanical design of RICH 1 is guided by the requirements discussed in Sect. 2.2:

- The limited duration (18 months) of the LHC shutdown (LS2) does not allow sufficient time to remove and replace the current RICH 1 magnetic shield, nor to excavate concrete at the base of the cavern. This means that the design of the new RICH 1 mechanics must be compatible with the existing shield.
- The increase of focal length of the spherical mirror requires an extension of the Cherenkov gas enclosure, which supports the optical system.
- All mirrors and their mounts will be replaced.

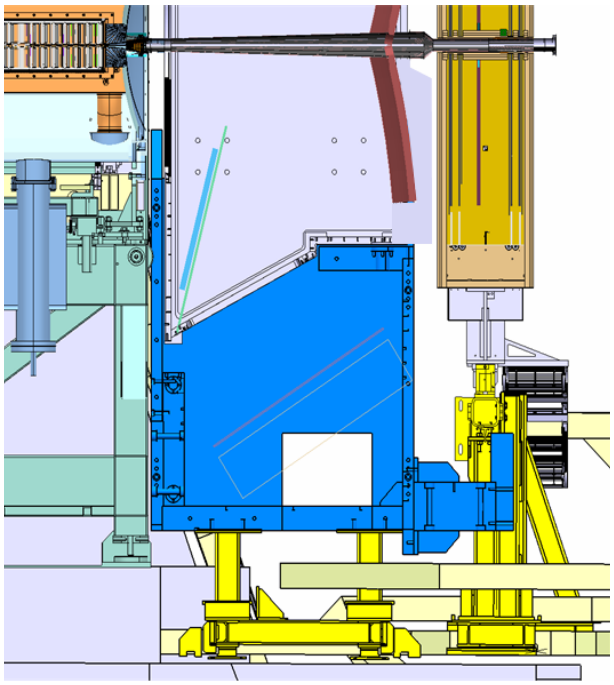

Figure 2.22: Schematic of the existing VELO, TT and RICH 1 magnetic shielding, showing the new RICH 1 optics. The extension towards the TT is required to accommodate the spherical mirrors and allow the photon detector box to come closer to the beam pipe.

- The photon detector mounting frames and the sealed enclosure which houses the frames inside the magnetic shielding will all be replaced.

The LHCb z-axis follows the beam line which is inclined at +3.6 mrad to the horizontal, and the y-axis points upwards, orthogonal to the z-axis, with the x-axis horizontal. RICH 1 will be aligned with the LHCb coordinate axes and extend from $z = 985$ mm to $z = 2245$ mm, as introduced in Sect. 2.4.1 and shown in Fig. 2.20.

The photon detectors are supported from the magnetic shield. Since the photon detector plane now moves further away from the beamline, the amount of space within the magnetic shield for the photon detectors and readout electronics is limited, demonstrated in Fig.2.22. Once the layout of the electronics and services is defined, a suitable box will be designed to provide gas and light tightness combined with ease of installation. In the event of the downstream tracking (UT) detector being re-defined to higher z, a further extension of the RICH 1 gas volume would then be evaluated.

(i) Magnetic shield

There are two magnetic shield boxes, one above and one below the beam pipe. In the absence of magnetic shielding, the photon detectors of RICH 1 would experience a magnetic field from the LHCb dipole of about 60 mT, way beyond the operating tolerance of MaPMTs. The magnetic shield, which reduces the field inside it to 2.5 mT, will stay in place for the upgrade of RICH 1, only slightly modified to support the new photon detectors. Each shielding box consists of three

parts: the main part of the shield, which is mounted on the concrete wall/floor, and two side elements that can be removed with the use of a local 1-tonne crane for the insertion/extraction of the photon detectors. There is scope for a new design of the side elements that would make the access to the photon detectors easier.

(ii) Gas enclosure

The main functions of the gas enclosure are to provide containment of the gas radiator and to act as a stable platform for the mirrors. It must also be light tight and non-magnetic. The gas pressure will be close to atmospheric (this is ensured by the gas recirculation system and protected by local bubblers) but the enclosure must withstand pressure differentials ± 3 mbar without compromising the mirror alignment.

Although the current RICH 1 enclosure cannot be re-used, the new design will retain most of the engineering concepts from the original and, where possible, re-use some of its components. The enclosure is essentially a six-sided box with each face closed by components having very different requirements.

- The upstream face is closed by an element which maintains the gas and provides a light seal between the enclosure and the VELO exit window. This structure must also ensure that minimal force is exerted on the VELO and the upstream wall of the enclosure and that manufacturing tolerances and changes due to temperature can be accommodated.
- The top and bottom faces are closed by quartz windows that allow Cherenkov light to pass through to the photon detectors mounted behind.
- The downstream face accommodates the low-mass exit window which is sealed to a fin on the beryllium beam pipe.
- The side faces are closed by panels that are designed to maximise the access for installation of the internal optical components.

Each face of the main structure is machined from 30 mm-thick aluminium-alloy plate which is then welded at the edges to form the enclosure. All mounting sealing and welding features are machined into the plate and the overall weight will be in the region of 500 kg. The dimensions of the entrance and exit windows are dictated primarily by the the LHCb spectrometer acceptance but the installation sequence also imposes constraints. The VELO exit window, which is integral to the beam pipe, must pass through the gas enclosure entrance window, as must its clamping flange which is a complete ring. Where gas and light-tight seals are required, these are made from EPDM[5] which is radiation tolerant and has been demonstrated to be compatible with the fluorocarbon gas over five years of operation of the current RICH 1.

The overall dimensions of the gas enclosure will be adapted to accommodate the new optics. This will require an extension of the downstream face in the z-direction by 90 mm. Similarly the upstream face will require an extension in the y-direction to accommodate the new flat mirrors. Both these extensions are compatible with the existing magnetic shields and neighbouring detectors.

The gas enclosure is supported by the lower magnetic shield from mounts that allow its alignment to the nominal beam line. These mounts will be the only external points of contact

[5]Ethylene Propylene Diene Monomer (M-class) rubber

and a nominal clearance from the shield of 10 mm all round has been demonstrated with the current RICH 1 to be sufficient to accommodate construction tolerances, movement of the shield and room for alignment.

- *Seal to VELO*: By sealing directly to the VELO, additional material in the path of particles is eliminated. It appears quite feasible to re-use the existing RICH 1 seal [26]. This is based on a stainless-steel bellows structure that provides a longitudinal compliance of order ± 10 mm and a transverse compliance of order ± 1 mm to allow thermal, pressure and vibration movements without generating significant forces on the RICH or the VELO. Access to both sides of this seal is possible from inside the gas enclosure.

- *Exit window and seal to beam pipe:* The exit window of the current RICH 1 is a low mass ($0.7\% X_0$) composite panel made from carbon-fibre-reinforced epoxy skins separated by a 16mm-thick PMI foam core. The seal to the beam pipe uses a diaphragm of silicone rubber loaded with carbon to provide the required opacity to light. This diaphragm fits over the inner aperture of the exit window and a fixed fin machined in the beryllium beam pipe. It appears possible to re-use this exit window at the new z position, but the diaphragm would require a new design and the corresponding injection mould would need to be manufactured.

- *Quartz windows:* The aperture required to allow the Cherenkov light from all particles within the spectrometer acceptance to reach the photon detectors will be larger than that provided by the existing quartz windows. New windows will need to be ordered but their design and specifications will be very similar to those currently in use. In particular the windows will be assembled from two panes glued along the edge and glued into an aluminium-alloy frame that will be sealed to the gas enclosure using an EPDM O-ring. The use of two panes simplifies the application of the non-reflective coating, allowing vacuum deposition facilities that are readily available at CERN and in industry.

(iii) Photon detector assembly

The RICH 1 photon detectors will cover the focal plane which is 690 mm wide by 1150 mm long. The possibilities for a column- or row-like structure will follow the philosophy of RICH 2, and these options are discussed in Sect. 2.4.3. The space requirements for the MaPMTs and services, and the ease of access, are more constrained for RICH 1; the engineering details will be finalized in a future Engineering Design Review.

(iv) RICH 1 mirrors

Carbon fibre spherical mirrors, with an aluminum (Al) and magnesium fluoride (MgF_2) coating, satisfy all the requirements of RICH 1 very well, and have been successfully used in the current detector for several years of LHCb operation. A suitable mirror manufacturer, as for the existing RICH 1 detector, is the CMA company[6] using an optical replication process. The process is illustrated in Fig. 2.23. The mirror surface is built up from carbon fibre sheets, pre-impregnated

[6]Composite Mirror Applications, Inc., Tucson, AZ, USA; www.compositemirrors.com.

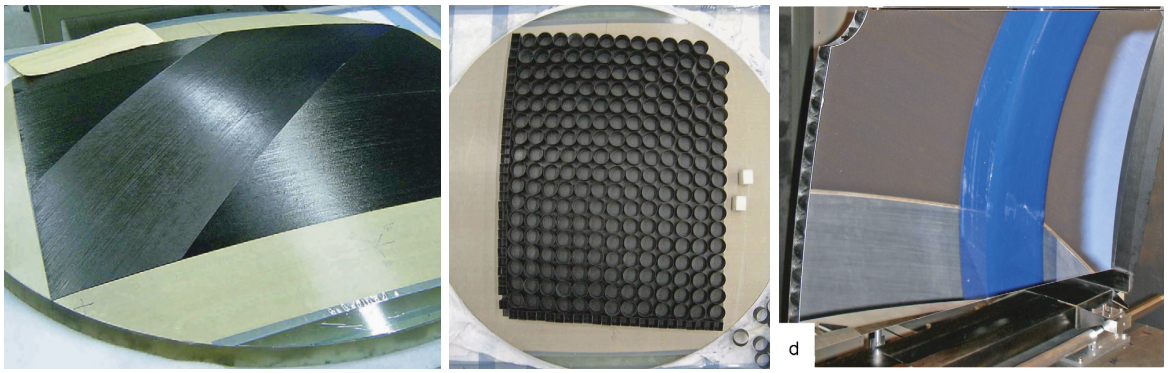

Figure 2.23: Stages of the RICH 1 spherical mirror manufacturing process, from left to right: carbon fibre sheets are being layered onto the mandrel; the front skin and the core structure; the finished product.

with cyanate ester resin, which are layered over a borosilicate (Pyrex) glass mandrel that defines the shape of the mirror's reflective surface. After manufacture, the mirrors are then coated, consisting of a metallic reflective surface, protected with one or more thin transparent layers. The reflectivity of the mirror depends on the coating material and, through interference effects, on the thickness of the transparent layers, which can be tuned to maximise the reflectivity for a given wavelength range and angle of incidence. For the RICH 1 spherical mirrors an Al coating protected with a MgF_2 layer ($Al + MgF_2$) was preferred, and applied by the SESO company[7].

The carbon-fibre mirrors must be radiation tolerant. Prototype RICH 1 sperical mirrors have been exposed to 10 kGy of radiation, somewhat less than the expected dose for the LHCb upgrade. However no deterioration whatsoever of the RICH 1 mirror performance has been observed in the current experiment.

The requirements for the optical quality of the flat mirrors are similar to those for the spherical mirrors, but since the flat mirrors are located outside the LHCb acceptance, they do not have to be particularly light and can be made from glass at lower cost. The flat mirrors will be assembled into two planes, one above and one below the beamline. Each plane comprises eight rectangular mirrors with dimensions 380.5 mm $\times$ 347.5 mm. A spacing of 3 mm between each segment results in a 1.5% loss in coverage. The overall dimensions of the flat mirrors need to be larger (in the y-direction) than the current flat mirrors. This implies that new mirror segments will be manufactured. The flat mirrors can be fabricated, for example, using 6.0 mm thick Simax[8] glass, the material and manufacturer as for the current RICH 1 detector. For the existing glass mirror coating, $Al + SiO_2 + HfO_2$ has been chosen for its high reflectivity in the UV.

The specifications for the optical properties of the RICH 1 mirrors were previously discussed in Table 2.4. For both the spherical and flat mirrors, the mirror geometry is characterized by the radius of curvature R, which should be as large as possible for flat mirrors, and the spotzise D_0. The existing RICH 1 flat mirrors have $|R| > 600$ m and $D_0 < 2.5$ mm; these tolerances satisfy both the spherical and flat mirror upgrade requirements. For the upgrade, the mirror coatings for both the flat and the spherical RICH 1 mirrors will be re-optimised for the changed angle of

[7]Societe Europeenne de Systemes Optiques, Aix-en-Provence, France; www.seso.com.
[8]3.3 borosilicate glass by SKL ARNY KAVALIER, a.s. COMPAS, Kinskeho 703, CZ-51101 Turnov.

incidence of the photons resulting from the new RICH 1 optics, and for the MaPMT quantum efficiency.

(v) RICH 1 mirror supports

The spherical and flat mirrors described in Sects. 2.4.1 and 2.4.2 will be supported from the gas enclosure. Experience of five years operation with the current RICH 1 mirrors has shown that an alignment precision of better than 0.2 mrad can be maintained through off-line analysis of charged particle tracks and their corresponding Cherenkov rings. This allows a relatively simple support system to be used, with initial assembly precision at the mrad level and no requirement for an electro-mechanical alignment feature that can be used during data taking. Owing to the likely need to bake out the LHC beam pipe that passes through the centre of the gas enclosure it will be necessary to provide the means to remove and replace the mirrors. This is most easily done by mounting the mirrors on supports that can move in the x-direction on rails through the opened side panels of the gas enclosure.

The spherical mirrors are lightweight and can be supported with adequate stability using carbon-fibre-reinforced polymer C-frames, with each C-frame supporting one upper and one lower spherical mirror section. The lateral dimensions of the mirror sections are smaller than those currently in use (removal of the aerogel radiator implies a smaller angular acceptance is required), and the space available in the downstream extension of the gas enclosure is sufficient to accommodate the C-frames and their rails which attach to floor of the enclosure.

The flat mirrors are located outside of the spectrometer acceptance and again there is no special requirement for the mirror mounts to be lightweight. Each mirror segment will be glued at its centre to polycarbonate mounts that have a three-point adjustment system. These mounts are bolted to rigid aluminium-alloy plates and V-blocks fixed to these plates sit on horizontal stainless-steel rails fixed to the upstream wall of the gas enclosure.

The increase in height of the flat mirrors implies that the gas enclosure vertical dimensions will need to be extended, as can be seen in Fig. 2.22.

2.4.3 RICH 2 mechanics

It has been demonstrated that the optics layout of the present RICH 2 is well adapted to the expected luminosity foreseen for the LHCb upgrade [14]; simulations of the performance will be summarized in Sect. 2.5. Therefore the RICH 2 superstructure, mirrors, the entry and exit windows, the central tube, the quartz windows and the magnetic shields are retained. Given that the mechanical components have required years of engineering and fabrication, this is a huge benefit in term of cost and human resources. However, this means that the new opto-electronics chain will need to be compatible with the mechanical constraints, and also RICH 2 will need to accommodate a new mounting structure for the MaPMTs. Fig. 2.2 shows a schematic of RICH 2 and its main components and Fig. 2.24 shows the optical layout.

The RICH 2 mirrors will need to retain their optical quality for at least 20 years after fabrication. To measure any ageing effects of the reflective coatings in the experimental conditions, coated glass specimens have been left into the gas enclosure since LHC start-up. These specimens will be eventually re-measured, although the present beam data do not show any signs of degradation. In addition, after years of operation, dust will accumulate on the mirror surface and a contact-less cleaning method is being investigated. For the RICH 2 upgrade, it is not

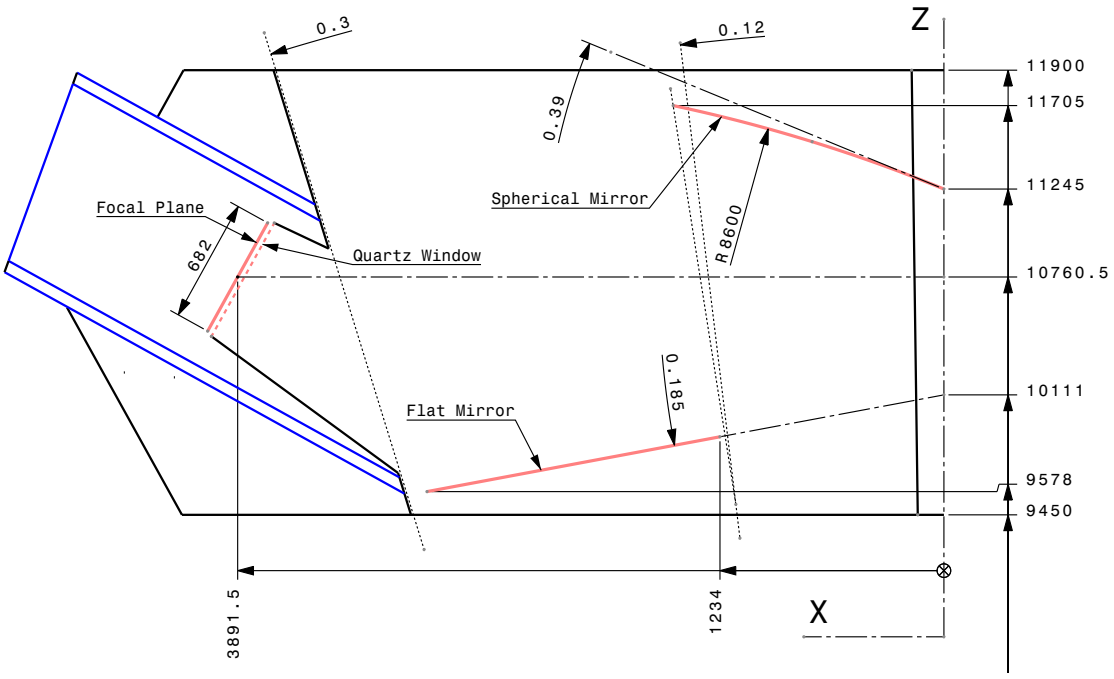

Figure 2.24: Half view of the RICH 2 optical layout in the $x - z$ projection.

foreseen to re-align the mirrors. LHCb RICH mirrors have shown to be stable over the years and no decrease in performance has been observed.

The magnetic shields of RICH 2 [27] are located on each side of the superstructure which house the photon detectors and all the readout electronics. Within the shields the magnetic field strength is as low as 0.5 mT in the region of the photon detectors, hence the magnetic environment is far less hostile than in RICH 1. Nevertheless, as in RICH 1, we also envisage to have local magnetic shielding around the individual MaPMTs.

All components of the upgraded RICH 2 will have to withstand 10 and more years of radiation, which will add to the 8 years of operation up to LS2. An extra ∼1 Mrad in the central region, down to ∼40 krad in the region of the photon detectors is expected (see Table 2.3). The polymer components used are radiation resistant: the polymethacrylimide (PMI) foam used in the windows, carbon fibre-epoxy composites of the central tube and the entry window, polycarbonate (PC) for the mirror supports, rope-moulded EPDM rubber for the assembly sealing, and epoxy glue for bonding many structures as the sandwich panels and mirror supports.

(i) Photon detector assembly

The photon detectors have to cover both RICH 2 photon-detector planes, each of which is 682 mm wide by 1300 mm high [24]. As will be explained in Sect. 2.4.4, the MaPMTs and readout boards are grouped into a module of four (2×2) elementary cells, resulting in 16 (4×4) MaPMTs which form a photon detector module (PDM) . The modules are then arranged to form a matrix with minimum gaps to achieve the maximum active area. With a PDM size of $116 \times 116\,\text{mm}^2$, a minimum pitch of 117 mm is required. To populate the full focal plane, the PDM matrix is 6 columns × 12 rows.

Two scenarios are envisaged for building the photon detector matrix:

- *Column arrangement:* The twelve PDMs are stacked vertically on a support column and six PDM columns are assembled in a structure to obtain the full photon-detector assembly. This arrangement offers a simpler solution for incorporating active cooling components along the height of the column. However the columns are long, 1.5 m, heavy, and consequently difficult to handle during assembly and maintenance.
- *Horizontal row arrangement:* Six PDMs are assembled on a support which has a "rack" layout. Twelve of these rack modules are then stacked into a frame to complete the photon detector assembly. Each of these modules are then half the weight of the column layout but the cooling becomes rather more complicated. In the likely event that the MaPMT granularity is reduced in the outer region of the photon-detector plane to save cost, there would be different PDM types and the photon-detector matrix would no longer have a constant pitch. In this configuration the row arrangement of the photon detector assembly would be chosen.

The complete structure of the photon detector mechanical supports will be made of aluminium and anodised in black. The structure will have a kinematic system to align the full photon detector matrix in respect to the alignment of the optical system. Like in the current RICH 2, the MaPMTs will be in a dry atmosphere of N_2 to avoid any condensation on the cooled elements. A gas flow of 250 l/h (two full volume exchanges of the enclosure per day) is sufficient to ensure good operation conditions.

2.4.4 MaPMT modularity and front-end mounting scheme

A modular arrangement has been adopted for mounting the MaPMTs and front-end readout boards, and a similar layout is proposed for both RICH 1 and RICH 2. Due to the large number of MaPMTs, the design of the modular structure must fulfil several requirements:

- Close-packing of MaPMTs onto a large surface;
- Ease of access for repair and maintenance;
- Structural stability;
- Incorporate electrical and electromagnetic insulation, and interface electrical connections from/to the MaPMT. Interface the Detector Control System (DCS) for monitoring important parameters;
- Incorporate local magnetic shielding;
- Allow thermal dissipation and provide access for heat transfer to the cooling system;
- Allow the mounting of lenses (if necessary) and/or optical filters.

The current modular structure is based on several past developments [28–30]. As discussed in Sect. 2.4.3, the Elementary Cell (EC) assembly consists of 2×2 MaPMTs. The full PDM module is then made of four ECs (2×2 in the current baseline).

(a) (b)

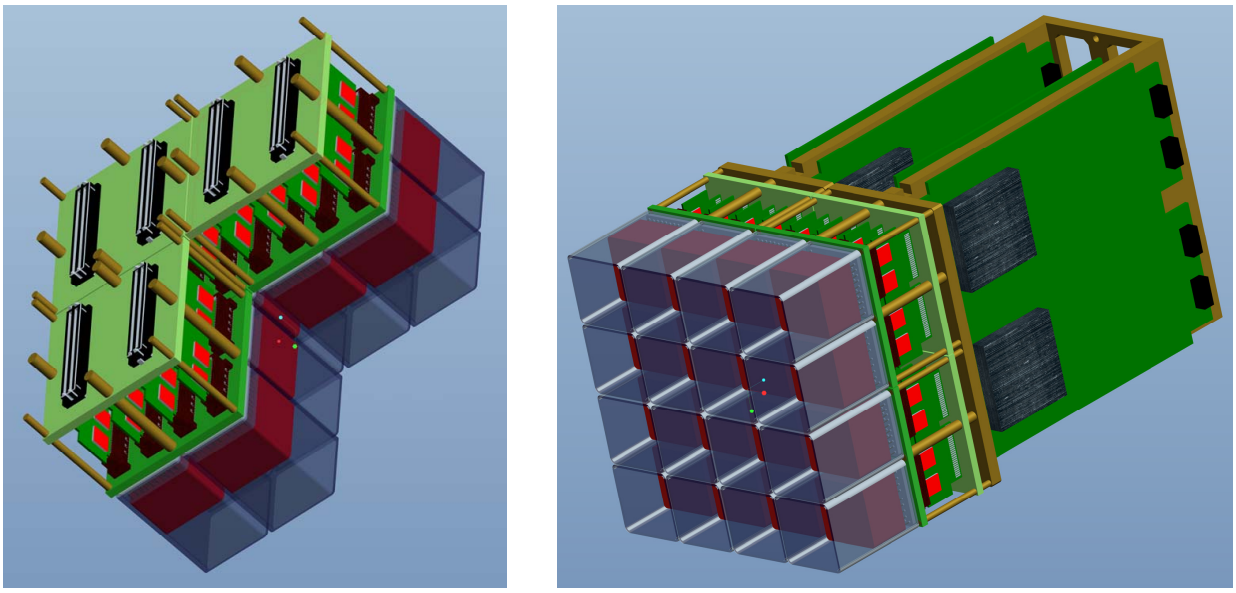

Figure 2.25: The MaPMT modular assembly: (a) back-side of three of the ECs with the connectors interfacing to the DEB, (b) drawing of one full PDM.

The EC is built around a PCB "base-board", with four custom SMD sockets to house the four MaPMTs, as well as the high-voltage dividers feeding the MaPMT dynodes, and a temperature sensor for the DCS. A picture of a prototype base-board with a single MaPMT installed is shown in Fig. 2.3. Thick copper layers inside the base-board are used to take out heat produced by the voltage dividers, via thermal conduction along the screws. On the back side of the base-board, suitable connectors interface to the CLARO Front-end Electronics Board (FEB), each one housing four 8-channel CLARO chips. The FEB mounting minimizes the input capacitance to the pre-amplifiers. Eight FEBs per EC are sandwiched between the base-board and a back-board, interfacing the output of the FEB to the Digital Board. The PDM module is then is formed from four ECs. A drawing of the back-side of three ECs installed into a PDM, showing the connectors interfacing to the Digital Board, is shown in Fig. 2.25 (a). The baseboard and back-board are mounted to a suitably machined aluminium back-plane, supported by two perpendicular aluminium plates (backbones) securing the Digital Board. The PDM is mounted to the support structure which also provides thermal contact with the cooling system.

A drawing of the full PDM is shown in Fig. 2.25 (b). Note that the Digital Boards are modularized to a 4×1 grouping of MaPMTs, with four cards per PDM (visible in the figure).

(i) Use of lenses

For the baseline RICH upgrade, approximately 4500 close-packed MaPMTs will be required to equip the photon detector planes of RICH 1 and RICH 2. The number of MaPMTs, and hence the cost, can be reduced by placing lenses in front of the MaPMTs. One of the available options would be to place a single hemispherical lens with one refracting and one flat surface in front of

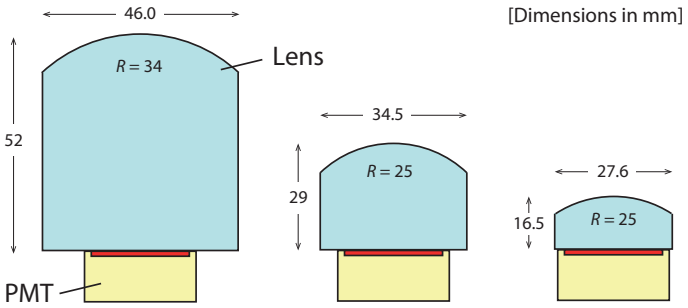

Figure 2.26: Dimensions of the lenses giving demagnification factors of 2.0, 1.5 and 1.2, from left to right, respectively.

an MaPMT as shown in Fig. 2.26. The full geometrical acceptance of the photon detector plane can be projected onto the active area of the MaPMTs by selecting the focal length and the total thickness of the lenses. As proof of principle, a 3×3 cluster of MaPMTs (7600 series) equipped with lenses has been demonstrated [31]. The HERA-B and Compass experiments have also successfully employed optical systems with different lens designs in their RICH detectors [32, 33], and alternative optical systems have been previously studied for LHCb [34].

For RICH 2 the pixel size uncertainty of 0.20 mrad makes only a small contribution to the total Cherenkov angle resolution of 0.60 mrad. Using lenses with a demagnification factor of 1.6 throughout RICH 2 would reduce the number of required MaPMTs by 30%, while bringing only a small reduction ($\sim 10\%$) in photon yield through reflection losses. However the occupancy of Cherenkov photons is largest in the middle third of the photon detector planes and the use of lenses may degrade PID performance. Using lenses with a demagnification factor of 1.9 in the upper and lower third of the planes, together with an intermediate region of 1.6 magnification, could give a reduction up to 40% of the total number. For RICH 1 the pixel size error is comparable to the chromatic and emission point errors. In the peripheral regions of the RICH 1, the employment of lenses with a demagnification factor of 1.6 is under consideration, which could reduce the total number of RICH 1 MaPMTs by up to 27%. Due to high occupancies, no lenses are foreseen in the central region of RICH 1.

Lenses can be made of fused silica (quartz) or produced with the Sol-Gel technology [35]. With the Sol-Gel method, arrays with 4×4 or more lenses can be cast into a single piece. Fused silica lens arrays can also be produced in single modules. This will facilitate the design of the mechanical structure holding the lenses.

Special care has to be taken with the lens design, due to charged particles traversing these and emitting Cherenkov photons. These are predominantly trapped by undergoing total internal reflection. Therefore, by optically separating lenses, by designing them as thin as possible and by decoupling them from the MaPMT input window, this induced background can be controlled and minimized.

Conversely, a larger (4-times the area) 64-pixel H12700 MaPMT could be used instead of lenses, resulting in the same reduction factors and corresponding savings of MaPMTs, as discussed in Sect. 2.2. Simulations of optical systems with lenses are currently ongoing, and we will soon start studies of the H12700. We therefore expect to reduce significantly the number of required MaPMTs, by up to 30%.

(ii) Local magnetic shields

As discussed in Sects. 2.4.2 and 2.4.3 , the magnetic shields surrounding the photon detector planes reduce the fringe magnetic field to a maximum value of 2.5 mT in RICH 1 and ~ 0.5 mT in RICH 2 [12]. Each elementary cell will be fitted with a magnetic shield consisting of a square tube of thickness up to 1 mm of high permeability material with properties similar to that used for the tests described in Sect. 2.3.2. Alternative shielding configurations, such as shielding individual MaPMTs, are also under consideration. It is expected that the shields will protrude by up to approximately 2.5 cm from the surface of the photocathode window. Thus a careful design will be required in order for the magnetic shields not to introduce shadowing of Cherenkov photons or to interfere with the lens system. Studies to determine the minimum value required for the magnetic shields to protrude from the MaPMT entrance window are ongoing.

2.4.5 Access to the beampipe

The two RICH detectors surround the beampipe and the respective gas enclosures cannot be withdrawn/separated to give access to it. This design choice was driven by the requirement to seal the vessels by giving a low material budget in central region. These constraints for the beampipe access will be identical for the upgraded RICH detectors.

As described above, for RICH 1, the beampipe section is connected on the upstream side to the VELO vacuum tank which seals to the RICH 1 gas enclosure, and on the downstream side the exit window makes a seal to the beampipe. Hence the RICH 1 C_4F_{10} radiator gas is in contact with the beam pipe during operation. The insertion or extraction of the beam-pipe section can therefore be made only after the prior installation of the gas enclosure. The RICH 1 mirrors and photon detectors are installed *in situ* around the beampipe, with the appropriate beampipe protection.

RICH 2 has a central tube, approximately coaxial to the beam pipe with a clearance of 45 mm [24] (the central tube is horizontal while the beampipe is aligned along z). The beam pipe is inserted or extracted through the RICH 2 vessel as shown in Fig. 2.27(a). A temporary heating jacket for the bake-out is introduced from the upstream side. For the upgrade, a thin permanent heating jacket and insulation layer are envisaged to simplify the bake-out operation, shown in Fig. 2.27(b).

2.4.6 Readout electronics

The architecture of the front-end (FE) electronics is compatible with the specifications defined in Ref. [36]. An overview of the electronics readout chain has been given in Sect. 2.2.

The FE electronics are located on-detector in a confined space, and rapid access during detector operation will be difficult. Having an optimized system modularity facilitates the efficient removal of components, and isolating localised faults. The chosen 4×4 MaPMT modularity, described in Sect. 2.4.4, leads to a well-organized arrangement of FE electronics modules and data transmission links. The detector occupancy will vary significantly over the detector plane, from less than 1% at the detector periphery to more than 20% in the central region of RICH 1. Given that zero-suppression will not be performed in the highest occupancy regions, the bandwidth requirement, excluding header information, will vary from about 40 Gb/s per 4×4 module to around 3 Gb/s per module in the low occupancy regions. Two variants of the FE digital board

(a) (b)

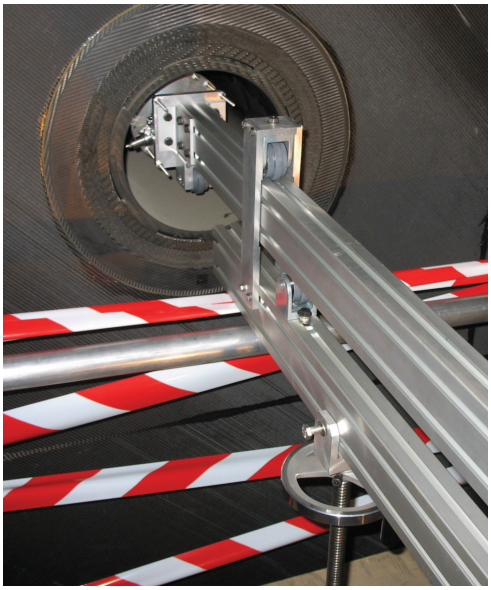

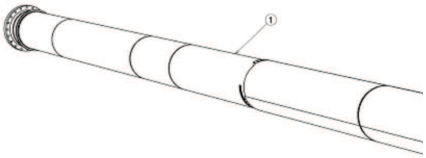

Description	tickness (mm)	density
Aluminium Foil	0.05	2.7
2 layers polyimide tape (Kapton)	2*0.06	1.53
Aerogel insulation (compressed)	4	0.11
2 layers polyimide tape (Kapton)	2*0.06	1.53
heaters	0.2	1.73
vac.chamber wall		

Figure 2.27: (a) View of the entrance window of RICH 2 when inserting the beam pipe (section UX85/3) from the downstream side; (b) The planned permanent heating jacket mounted on the beam pipe, surrounding the central tube of RICH 2.

will therefore be used depending on whether zero-suppression is performed or not, as this allows a better optimisation of the data-flow topology.

Data transmission uses the GBT chipset developed at CERN [37, 38]. Both bidirectional and unidirectional fibre optic links are supported. The bandwidth available per link is 3.2 Gbit/s in "normal" mode. This can be increased to 4.5 Gbit/s if the GBT "wide-frame" mode is used. The GBT links are also used to distribute synchronously the LHC clock to the FE electronics.

(i) Data-flow from the digital board

The data-flow conforms to the scheme outlined in Ref. [36] and is implemented in reprogrammable FPGAs on the digital board. A schematic of the RICH readout system is shown in Fig. 2.5. The CLARO ASIC operates asynchronously and the timing of the digital outputs follow the timing of the analogue signals from the MaPMT anodes. Signals from the CLARO are registered using edge-triggered latches in the FPGA of the digital board. The latches are reset synchronously to the LHC clock every 25 ns. Logic is included to prevent the re-triggering of a channel due to spill-over from a previous bunch-crossing. This introduces a small photon-detection inefficiency but it avoids spill-over hits from polluting subsequent events.

The hits are buffered synchronously in the FPGA and every data packet is tagged with the beam-crossing ID (BXID) to allow downstream validation of the data. The buffered data are then formatted for transmission off-detector with or without zero-suppression, depending on the detector region.

For data transmission, there are 80 (112) bits available per GBT link-frame in the normal (wide-frame) mode. In regions with no zero suppression, transmission of a 4×64-bit hit map requires either four links in normal mode or three links in wide-frame mode; the latter option is preferred since it brings cost saving. The packing of the data in this scenario is straightforward as the GBT frame is always a fixed length and the header and data fields are always at the same offset within the frame. The implementation is therefore expected to require only modest FPGA resources allowing the use of one small FPGA per GBT link.

In the regions where zero suppression is performed, the 4×64-bit hit map is converted into a variable-length list of 8-bit hit addresses. Two possible strategies are under consideration for the data packing. The simplest is to use a fixed GBT frame to encode up to 8 addresses (11 in wide-frame GBT mode) and discard any additional hits in the event. This strategy can result in signal loss in some cases and inefficient use of the available bandwidth on average. A variable length scheme reduces these effects but is considerably more complex to implement, mainly because the header and data fields are not at fixed offsets. The physical implementation of the zero-suppressing module will use a single FPGA connected to 4×64 CLARO outputs and a single (optionally two) GBT link to transmit the multiplexed data. The larger number of IOs and increased complexity of the logic compared to the non-zero-suppressed case means that a larger FPGA is used for this variant of the digital sub-module. In both scenarios, a fast clock source and a fully pipelined architecture are needed in order achieve the required performance.

Off-detector there is the possibility to further process the data in the TELL40 modules before event-building, filtering and storage. At present there is no requirement for this, so generic firmware with only minor RICH-specific processing is expected.

(ii) FPGA and data links

The choice of a reprogrammable FPGA for the digital board instead of an ASIC or anti-fuse FPGA is driven by the complexity of the digital logic; there is significant risk that errors in the implementation may only become apparent at a late stage of the project. Furthermore the use of non-reprogrammable logic would remove the flexibility to adapt the front-end to changes in the DAQ protocols that may become necessary or beneficial in the future. However, the chosen FPGA must be tolerant to radiation and this restricts the choice of device. Studies of some existing SRAM-based FPGAs indicate that they can tolerate more than 100 krad of ionising dose, around five times the expected annual exposure, provided that techniques such as triple modular redundancy (TMR) and scrubbing (periodic refresh of the FPGA configuration) are employed. Further studies of these techniques are planned in order to estimate their impact on the FE design as TMR will significantly increase the required logic resources in the FPGA and the method of implementing scrubbing will depend on the chosen FPGA family.

The data and control links contribute significantly to the overall cost of the FE electronics. The number of links required depends on the number of photon hits and their distribution across the detector plane. There will be a region of the detector where zero-suppression is ineffective in reducing the data size; this region is expected to correspond to occupancies of greater than 1.5%. Simulation studies have been performed using different detector configurations in order to optimise the required number of links. For RICH 1 with a total of 1920 MaPMTs, at a luminosity of $20\times10^{32}\,\mathrm{cm}^{-2}\mathrm{s}^{-1}$ the number of MaPMTs located in the high and low occupancy regions is 711 and 1209, respectively. This particular scenario would require $711 + 1209/4 = 1014$ data links. Since non-zero-suppressed readout is robust against fluctuations in the occupancy,

it is advantageous to populate the largest region affordable with non-zero-suppressing digital sub-modules so that any unanticipated upward occupancy fluctuations do not cause front-end DAQ bottlenecks.

(iii) Power supplies

The existing bulk power supplies will be reused for the upgrade. Individual modules are rated at 40 A at up to 7 V and there are 36 modules currently in use for RICH 1 and 48 for RICH 2. Estimates of the power consumption of the upgraded FE electronics indicate that a modest increase in the power supply capacity will be sufficient. The power supplies are regulated locally on the digital sub-modules using radiation-tolerant DCDC converters or linear regulators.

The existing bulk power supplies can be individually and remotely controlled. If finer grained isolation is required, a switching panel external to the FE electronics volume can be adopted.

Most of the external electronics hardware connected to the RICH detectors will be installed in cabinets/racks, as for the current arrangement. For RICH 1 these cabinets are located on the balcony adjacent to the spectrometer and for RICH 2 they are situated underneath the concrete structure supporting that detector. This comprises the low and high voltage systems, and the detector control system.

(iv) Controls interface

The FE electronics produce data in response to fast control commands received on a "master" link. In addition, configuration and monitoring data are exchanged over the same physical link. This link is implemented using the GBT chipset and using a bidirectional data path. The CERN SCA chip acts as a bridge between the GBT protocol and a number of widely-used standards such as I2C, JTAG and SPI. The controls architecture and protocols are common to all sub-detectors and are defined in [36]. Two strategies for the distribution of these data to the RICH FE modules are under consideration. The preferred strategy is to implement the master link end-point directly on the digital board, but an alternative approach employing an intermediate fan-out module is also being explored. Although being more cost effective, the use of a controls fan-out might introduce an undesirable point of failure.

The SCA interface is used for FPGA-firmware loading via JTAG, for scrubbing control, and CLARO configuration. Each 4×1 digital board configures 32 8-channel CLARO ASICs. Eight bits of configuration data are needed per channel of the CLARO, giving a total of 2k bits per digital board. This corresponds to approximately 2 ms configuration time with a 1 MHz SPI clock.

2.4.7 Alignment, calibration and monitoring

Most of the current RICH alignment, calibration and monitoring systems can be re-used for the upgrade. The monitored parameters can be grouped as follows:

- *Environmental and gas monitoring:* It is desired to monitor the temperature of the gas radiators with an accuracy of 0.1 °C and pressure with an accuracy of 0.1 mbar relative to atmospheric and 0.3 mbar absolute. This allows the refractive indices of the Cherenkov-radiator gases to be scaled as a function of these parameters. An existing gas analysis chamber will be re-used to monitor gross changes to refractive indices during detector

operation, even though the refractive indices will subsequently be measured accurately off-line with data. All environmental sensors, including those which measure ambient temperature and humidity of the environment and of the photon detectors, will be interfaced to the Embedded Local Monitoring Boards (ELMB), as currently.

- *Safety Interlocks:* These are based on Programmable Logic Controllers (PLC) in a closed loop, that can switch off power of the whole RICH detector in the event of any overheating. Two Pt100s in each photon detector box will be hard-wired to the PLC in the control room. A set of thermo-switches (one per photon detector module) will be used for more localized increases in temperature.

- *Photon detector characteristics:* It is very important to constantly monitor the gain and efficiency of the MaPMTs because the gain decreases with light illumination time (see Sect. 2.3.2). By the same token, the readout electronics will be similarly monitored. The presence of the magnetic field also affects the gain of the photon detectors, so it will be important to produce a "gain map" for all MaPMT channels, with the spectrometer magnet switched on and off. A system with a calibrated LED source and/or a calibrated photon detector in each RICH will therefore be developed. Whilst it is not expected that the magnetic field will introduce image distortions of the MaPMTs or cross-talk between adjacent channels, nevertheless a system similar to the current RICH 1 or RICH 2 for the mapping of the magnetic distortions can in principle be build if necessary.

- *Mirror alignment:* All mirror segments that form a common mirror surface must be initially aligned with an accuracy of 0.5 mrad or better. The mirror alignment can be monitored accurately with physics data, however an initial alignment of the mirrors and their continuous monitoring for movement is important. Both RICH 1 and RICH 2 detectors have mirror alignment monitoring systems based on laser beams and cameras, which can both be reused. Although successful, these systems do have their limitations, and it may be beneficial to develop a more advanced system that can monitor all mirrors, based on the imaging of a pattern.

2.4.8 Services

(i) Cooling system

The power dissipation of the FE electronics for the upgraded RICH detectors is similar to that of the present system, therefore the cooling unit with its transfer lines can be preserved. The FE systems will be cooled with C_6F_{14} fluid in a liquid mono-phase state, which works in a closed loop. Table 2.8 summarises the main parameters of the cooling system. For a detailed description see Ref. [39].

The cooling plant allows adjustment of the temperature and the input pressure of the coolant to obtain the appropriate conditions. The targeted total leak rate of the four cooling circuits (detector side) is 0.1 kg/day.

(ii) Gas system

Both gas systems that provide C_4F_{10} and CF_4 to the RICH 1 and RICH 2 detectors, respectively, will be reused for the upgrade. To minimise scintillation light from the RICH 2 gas radiator,

between 4 to 8 % of CO_2 is mixed with the CF_4. One of the challenges of the gas systems is to regulate the pressure into the detector chambers with an accuracy of less than 0.2 mbar. The main parameters of the gas systems are summarised in the Table 2.9 and detailed technical accounts can be found in Refs. [40, 41].

The gas system is composed of the following sub-modules:

- *The mixer module:* fresh gas is injected into the loop via this module. For the RICH 2 system, mass flow controllers allow an adjustment of the ratio between CO_2 and CF_4.
- *The distribution module:* this limits the gas flow in the loop.
- *The pump module:* the pump, coupled with a controlled return valve placed on the outlet of the gas chamber, regulates the flow, hence the pressure, inside the gas enclosure.
- *The buffer tank:* the compressed gas passes into a buffer tank to compensate for atmospheric pressure changes.
- *The membrane module:* this is used to separate the gases (radiator and CO_2, or CO_2 and N_2) during the filling or the emptying procedure.
- *The purifier module:* this removes water, oxygen and other contaminants, where the gas passes through a molecular sieve.
- *The liquefying module:* this module is specifically used to recover the RICH 1 gas. It separates the C_4F_{10} which liquefies, while CO_2, N_2 and O_2 remain gaseous.

In case of failure of the gas system, a backup system maintains the gas pressure. This system is fully pneumatic and will compensate for any atmospheric pressure changes, while waiting for the main system to resume. The pressure inside the detectors must not exceed an over- or under-pressure relative to atmosphere of 1.5 mbar. To prevent such conditions, a second level of safety is provided by means of bubblers close to the detector.

The typical contamination of the gas radiators is due to micro-leaks which lead to air passing into the gas enclosure or into the gas system. To improve the purification of C_4F_{10}, the gas system will be upgraded by adding a new buffer tank to the liquefying module. With this new configuration, the gas flowing in the loop will be liquefied in the buffer tank, and simultaneously, fresh gas from the recovery tank will be evaporated and sent back into the loop.

Particular care will be devoted to the sealing of the new RICH 1 gas enclosure. Leaks are an important issue in terms of gas purity, the cost of gas loss, and the global warming potential

Table 2.8: Characteristics of the cooling system.

Item	Characteristic
Coolant fluid	C_6F_{14}, liquid mono-phase
Number of transfer line:	4 lines
Cooling power	$4\times$ 2 kW
Maximum input pressure	<7 bar
Flow rate	$\sim$ 700 l/h per line (at 4 bar, in the present system)
Input temperature	$>11\,^{\circ}$C

from fluorocarbon gasses in the atmosphere. The leak rate will be lower than 0.2 l/h, which corresponds to a gas loss of about 20 kg/year.

Table 2.9: The main parameters of the gas radiators and the gas systems.

System	RICH 1	RICH 2
Cherenkov radiator gas	C_4F_{10}	92−96 %: CF_4 + 4−8 %: CO_2
Gas density (1013 mbar, 21 °C)	9.85 kg/m^3	3.64 kg/m^3
Boiling point (1013 mbar)	−1.9 °C	−128 °C
Detector Volume	4 m^3	100 m^3
Flow rate	$\sim$ 0.2 m^3/h	$\sim$ 5 m^3/h
Relative pressure, stability	$<$ 0.2 mbar	$<$ 0.2 mbar
Impurity:		
N_2	$<$ 0.4 %	$<$ 0.4 %
O_2	$<$ 0.1 %	$<$ 0.1 %
H_2O	$<$ 500 ppm	$<$ 500 ppm
CO_2	$<$ 500 ppm	–

2.5 Performance

The simulations for the RICH upgrade are performed using the standard LHCb software framework. For this, the *pp* collisions are generated using Pythia [42] with the beam configurations which existed in 2012 and with those expected from 2019 onwards, as listed in Table 2.10. Decays of hadronic particles are described by EvtGen [43] in which final-state radiation is generated using Photos [44]. The interaction of generated particles with the detector and its response are implemented using the Geant4 toolkit [45], as described in Ref. [46].

Throughout this section and defined in Table 2.10, "Lumi4" refers to a luminosity of 3.9×10^{32} cm^{-2} s^{-1} (the nominal 2012 running condition), "Lumi10" refers to 10×10^{32} cm^{-2} s^{-1} and "Lumi20" refers to 20×10^{32} cm^{-2} s^{-1}. Also, for all occupancy and PID-efficiency studies described below, $B_s^0 \to \phi\phi$ events are generated with the appropriate pile-up interactions. The performance plots then include all tracks in the event which are in the momentum range 1.5−100 GeV/c and have transverse momentum above 0.5 GeV/c, and in the polar angle range 0−300 mrad. A set of at least 20000 events is simulated and reconstructed for each configuration considered.

Table 2.10: Beam configurations for the RICH upgrade simulation. Here L_B is the luminosity per bunch crossing and ν is the average number of *pp* interactions per bunch crossing.

Luminosity condition	Luminosity cm^{-2} s^{-1}	Number of beam bunches	L_B cm^{-2} s^{-1}	Beam energy (TeV)	ν
Lumi4	3.9×10^{32}	1300	0.302×10^{30}	4	2.5
Lumi10	10.0×10^{32}	2400	0.417×10^{30}	7	3.8
Lumi20	20.0×10^{32}	2400	0.834×10^{30}	7	7.6

2.5.1 Generation and reconstruction of simulated data

The simulation of the RICH detector is part of the standard LHCb simulation package and is described in [47] for the current RICH system. GEANT4 physics processes govern the production of Cherenkov photons, their transport through the various parts of the detector, reflections and refractions at optical boundaries and the production of photoelectrons. The simulation and reconstruction programs read the information relating to the geometry, material properties and optical properties of the various parts of the RICH detector from the LHCb detector database, where the corresponding RICH-upgrade parameters are stored. Wherever appropriate, the parameters of the current RICH detectors are also used for the upgraded RICH, for example the refractive indices of the radiators and the reflectivity of the mirrors.

The charged tracks reconstructed from hits in the tracking detectors and the digitized RICH hits are input into a log-likelihood algorithm [48] which defines the particle-identification hypothesis. In the first step of this algorithm, each reconstructed track is considered as a pion and, for this assignment, Cherenkov photons are generated and their trajectories are traced through the RICH system onto the MaPMT pixels. The signals created by these photons are compared with the GEANT4-generated hits to create a likelihood function for the event. This procedure is repeated by changing the hypothesis for each track in turn to electron, muon, kaon and proton and the final combination that gives the largest global likelihood is selected. The algorithm produces likelihood values for each track to be any one of the particles above, and these likelihoods are used for assigning the particle type for that track. In practice, the difference in the logarithm of the likelihood (DLL) between kaon and pion is used as a criterion for the particle-type assignment between those two particles. Similarly, log-likelihood differences are used for distinguishing between other particle hypotheses.

The effects of beam-related and other backgrounds have not been included in the simulation. However we have learned from LHCb data-taking that the occupancies in the RICH detectors are higher than predicted, and originate from two sources. Firstly the mean particle density in data is ∼30% higher than in Monte Carlo. This gives additional Cherenkov rings which increase the maximum occupancies in a correlated way. Secondly there is a more general "uniform" and uncorrelated photon background which affects all photon detectors, increasing the total number of hits throughout the RICHes at the $\sim 20-30\%$ level. Whilst this background has a minimal effect on the PID performance, it does lead to an increased average occupancies and hence possibly the need for additional readout bandwith. These two effects are currently being understood from Run 1 and the simulation will be improved to include such effects in the future.

2.5.2 RICH upgrade geometry

The overall geometry structure for the upgraded RICH is the same as that for the current RICH system, as described in the LHCb re-optimisation TDR [49]. However, several detector components have been necessarily changed and are described in the following subsections.

(i) RICH photon detectors

The HPDs have been replaced by R11265 MaPMTs in the upgraded geometry. In order to provide magnetic-field shielding, each 4×4 MaPMT module is surrounded locally by mu-metal which modifies the module pitch; the dimensions of the MaPMTs and the modules are given in Table 2.11. It should be noted that the detailed design of the hardware is still ongoing and minor

Table 2.11: The parameters of the R11265 MaPMTs and shielding modules used in the simulation. The number of modules and MaPMTs are also shown.

Parameter	Value
Anode size	23.0 mm
Pixel size	2.875 mm
MaPMT pitch inside a module	28 mm
Module Size	113 mm
Number of modules	
RICH 1	120
RICH2	160
Number of MaPMTs	
RICH 1	1920
RICH2	2560

variations in these dimensions may be expected in the future. In the simulation, each MaPMT has an 8×8 array of pixels. The MaPMT photo-detection efficiency assumes a super-bialkali photocathode and borosilicate window, and is taken from the manufacturer's specifications. This is plotted as a function of photon wavelength in Fig. 2.4 and peaks at ∼35% at 375 nm. In the simulation, the detector plane is equipped with MaPMTs to completely map the limits of the RICH acceptance for charged tracks. At present, no front-end electronics signal properties are simulated (eg. the loss of signal from binary readout), however a 90% global MaPMT readout efficiency is imposed.

As discussed in Sects. 2.2 and 2.4, there is a possibility in the future for a reduction in the number of photon detectors by using either lenses in front of the MaPMTs, or by replacing the MaPMTs with those of larger pixel size (H12700) in the outer regions of the detector planes. Neither of these options has been incorporated into the simulation at the current time.

(ii) Low momentum PID

As discussed in Sect. 2.2, aerogel will not be used in the upgrade and hence has been removed from the simulation. When reconstructing the data, to recover PID capability in the low-momentum region of RICH 1, the "pion veto" condition is used; if the track in the gas radiator is below the kaon threshold of 9.3 GeV/c, any signals produced must be from low-mass particles such as pions.

(iii) RICH 1 optical arrangement

As described in Sect. 2.4.1, the optical configuration for the upgrade has been re-defined; the following changes have been incorporated into the full simulation and are detailed in Table 2.12:

- The path length of the charged tracks in the radiator has been augmented in order to increase the amount of signal photons produced by each track.
- The radius of curvature of the primary mirror in RICH 1 has been increased from 2710 mm to 3800 mm, its position moved 90 mm downstream, and its angles of tilt and the location and the orientation of the flat mirror and the detector plane are modified accordingly.

Table 2.12: The main parameters of the RICH 1 optics used in the simulation. All the tilts are with respect to the vertical axis and all coordinates are in the nominal LHCb coordinate system where y is vertical, z points along the beam line towards the spectrometer and the origin is at the nominal beam collision point. For the current optics, nominal values of the parameters are quoted rather than the exact survey measurements. All parameters are quoted for the top half of RICH 1.

	Parameter	Current Optics	Upgraded Optics
Primary Mirror	Radius of curvature	2710 mm	3800 mm
	(y, z) of the centre of curvature	(841.2 mm, −672.8 mm)	(977.5 mm , −1640.0 mm)
Flat Mirror	(y, z) of the horizontal edge near the beam line	(349.0 mm,1333.7 mm)	(337.1 mm,1320.3 mm)
	Tilt angle	250.2 mrad	253.1 mrad
Detector Plane	Distance from origin	1738.1 mm	2154.2 mm
	Tilt angle	480.9 mrad	544.4 mrad

- The overall length of RICH 1 gas enclosure along the beam line has been slightly increased by ∼100 mm towards the present TT detector.

Geometries left unchanged in the simulation include the positions of the magnetic shielding iron and the vertical extent of RICH 1. Before converging on the geometrical layout described above, several alternative configurations were attempted [14, 25], and discussed in Sect. 2.4.1.

From here on, two configurations are defined:

- *The "current geometry":* This is the present LHCb geometry with the current optical configuration, however with the HPDs replaced by MaPMTs in the simulation.
- *The "upgrade geometry":* This is the new optical configuration described above, again with MaPMTs replacing HPDs.

The performance obtained is described in the next section.

2.5.3 Results from simulations

The occupancies in the different regions of RICH 1 are plotted for the current geometry in Fig. 2.28(a) for the Lumi4 beam conditions. It can be seen that MaPMT occupancies in the central region of RICH 1 approach 14%, which is comparable to the occupancies observed with the present HPDs, and which is known to give robust PID performance. Figure 2.28(b) shows the same plot with Lumi20 beam conditions. Occupancies increase to 35% in the central region which results in significant background due to the presence of overlapping rings from many tracks. As described in the following section, these effects lead to a degradation of the PID performance, and they have motivated the need for the upgraded geometrical configuration.

The upgraded geometry will now be quantified in terms of the following performance indicators:

- Single photon resolution;
- Photoelectron yields;

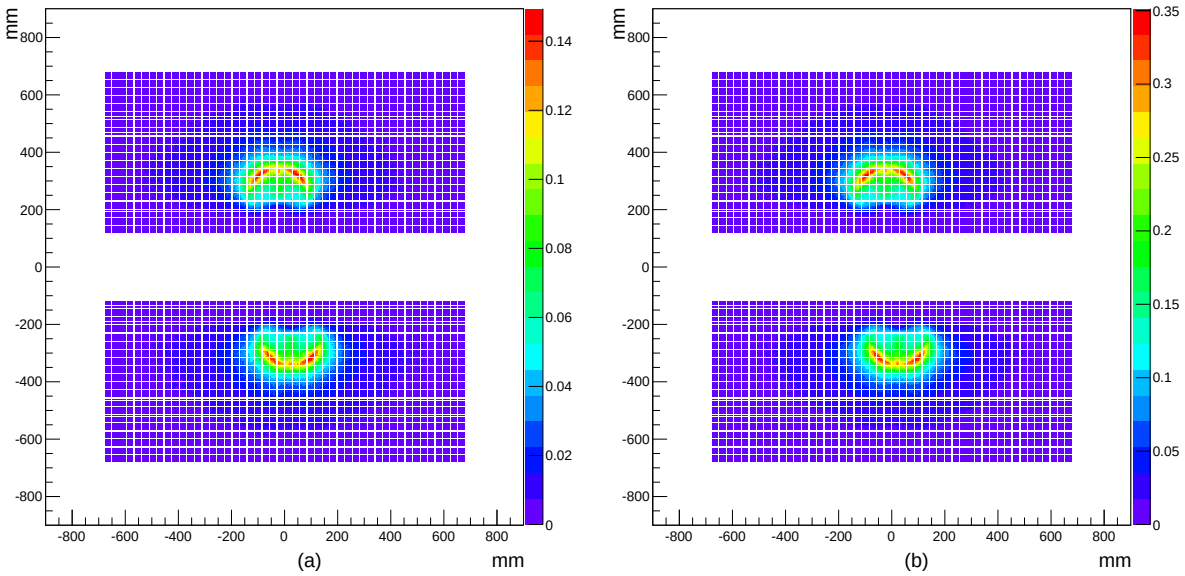

Figure 2.28: RICH 1 hit occupancies as a function of the local x and y coordinates on the photodetector plane for the current optics using (a) Lumi4, and (b) Lumi20 beam conditions. As expected, the distributions look very similar, however the occupancies shown on the right-hand scales are significantly different.

- Occupancies;
- Final PID performance.

(i) Single-photon resolutions and photoelectron yields

The single−photon Cherenkov angle resolution has four contributing terms which were discussed in Sect. 2.2. In Table 2.13 the single-photon angular resolutions are listed from the full simulation for the current and upgraded RICH detectors with MaPMTs, and between the RICH 1 and RICH 2 radiators. For comparison, also shown is the simulated performance of the current RICH 1 detectors with HPDs, and further detailed in Ref. [12]. There are a number of observations:

- *Chromatic error*: Since the peak of the QE is at a longer wavelength and is of narrower bandwidth for the MaPMT than for the HPD, the chromatic error contribution to the total resolution is reduced in the former case.
- *Emission point error*: The upgraded RICH 1 optical geometry is optimized to give the best emission point error within the constraints listed in Sect. 2.4.1. This has resulted in a significant improvement in emission point error compared to the current RICH.
- *Pixel error* : The effective pixel size of the MaPMT (2.875 mm) is similar to that of the HPD (∼2.5 mm). However the HPD has an additional contribution to the overall resolution

Table 2.13: Single photon resolutions and photon yields for isolated tracks from the full simulation in the two RICH detectors with MaPMTs. For comparison, also shown is the simulated performance of the current RICH 1 detectors with HPDs. The various contributions to the resolutions are listed. For the upgraded geometry, the comparison with the optical optimisation (Table 2.7) shows good agreement.

Resolutions [mrad]	Current RICH 1 (MaPMTs)	Current RICH 1 (HPDs)	Upgraded RICH 1	Upgraded RICH 2
Emission point	0.63	0.61	0.37	0.27
Chromatic	0.58	0.84	0.58	0.31
Pixel	0.61	0.99	0.44	0.20
Tracking	0.40	0.40	0.40	0.40
Total resolution	1.12	1.50	0.88	0.60
Photon yield	32	34	40	22

from the point-spread function resulting from the spatial dispersion of photoelectrons as they travel to the HPD anode.

- *Tracking error*: In this study, the contribution from the uncertainty in the direction of the charged particle track is assumed to be unchanged for the LHCb upgrade.

The comparison of the angular resolution contributions from the full simulation in Table 2.13 with those from the fast simulation (Table 2.7), shows good agreement.

Also shown in Table 2.13 is a comparison of photon yields for isolated tracks between the current and upgraded RICHes, showing an improvement in the case of RICH 1. Firstly the quantum efficiency used for MaPMTs is improved compared to that for HPDs, as seen in Fig. 2.4, and this leads to a marginal increase in the photon yield for MaPMTs. Secondly the removal of aerogel and the downstream displacement of the spherical mirror has increased the available path length, further contributing to the yield improvement.

(ii) Occupancy

The (x, y) distributions of occupancies on the photodetector plane obtained with the upgraded optical geometry are plotted in Fig. 2.29 for RICH 1 and RICH 2 at Lumi20. It can be seen that the increase of the spherical-mirror radius of curvature by $\sim \sqrt{2}$ has decreased the peak occupancy in RICH 1 by about 30% compared to that seen in Fig. 2.28. The peak occupancy, now at a manageable level of 24% in a restricted area of the detector, is influenced by an additional contribution from the increased path length of charged tracks when compared to the current geometry.

(iii) PID performance

The PID performance is defined in terms of the efficiency of identifying a true kaon as a kaon and the misidentification probability of a true pion to be a kaon or heavier particle. These quantities are plotted one versus the other for different values of the cut on the delta-log-likelihood (DLL)

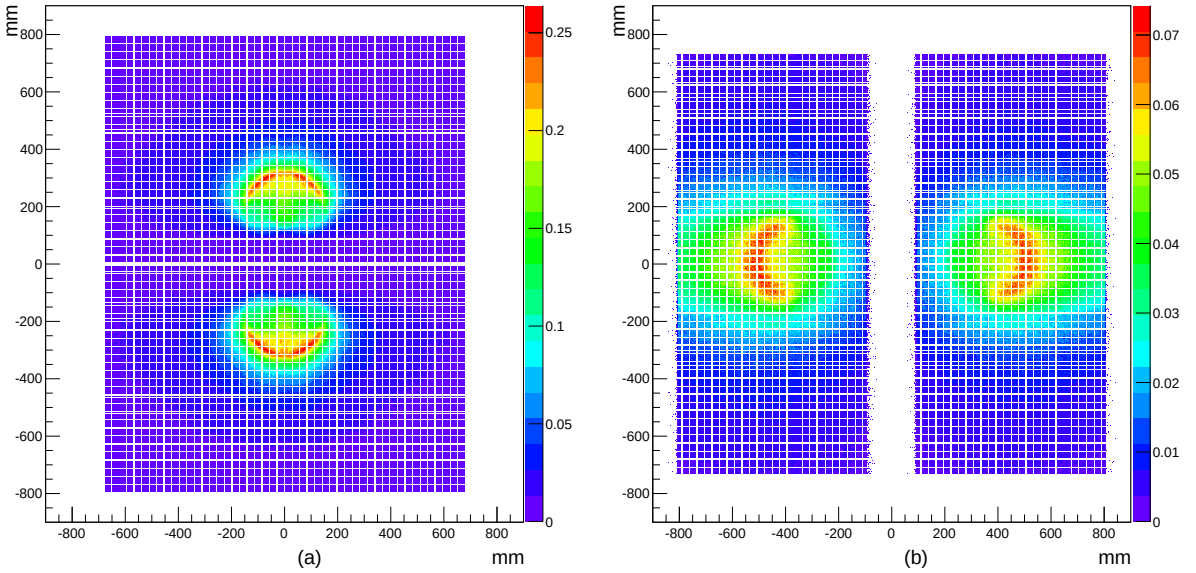

Figure 2.29: Hit occupancies as a function of the local x and y coordinates on the photodetector plane for the upgraded optics and Lumi20 beam conditions in (a) RICH 1 (b) RICH 2. The occupancies are shown by the right-hand scales.

between kaon and pion hypotheses obtained from the PID algorithm. In this way, one can select the DLL cut to choose between a highly pure sample of kaons (or pions) but at reduced efficiency, or a highly efficient sample but with increased background. The results are compared between the current and upgraded RICH geometries for different luminosities. These are obtained by running the full simulation and reconstruction chain in $B_s^0 \to \phi\phi$ events, as explained above.

In Fig. 2.30, the PID performance is plotted for the current geometry at the three luminosities, and compared to the upgrade geometry running at Lumi20. As expected, with the current geometry, there is a steady loss in PID performance as the the luminosity is increased from the present to the upgraded running conditions. However, this performance is mostly recovered when adopting the new RICH 1 geometry. For comparison, the PID performance plots are shown in Fig. 2.31 for the upgraded geometry at the three beam luminosities. The overall improvement in performance compared to the current geometry is apparent.

The robustness of the new RICH 1 geometry to the PID performance was verified by varying the following parameters:

- *The photodetector plane position:* The detector plane was moved towards the flat mirror plane from its standard position by 25 mm, 50 mm, 75 mm and 100 mm, in turn. When setting the level of pion misidentification probability at 1%, the corresponding kaon efficiency decreased by 0.5%, 1.5%, 2.5% and 5.0%, respectively.

- *Mirror radius of curvature:* When the detector plane is moved forward by 100 mm as above, the optimal focal position can be restored by decreasing the mirror radius of curvature from 3800 mm to 3600 mm. This is a useful option in case an extra 100 mm is required for

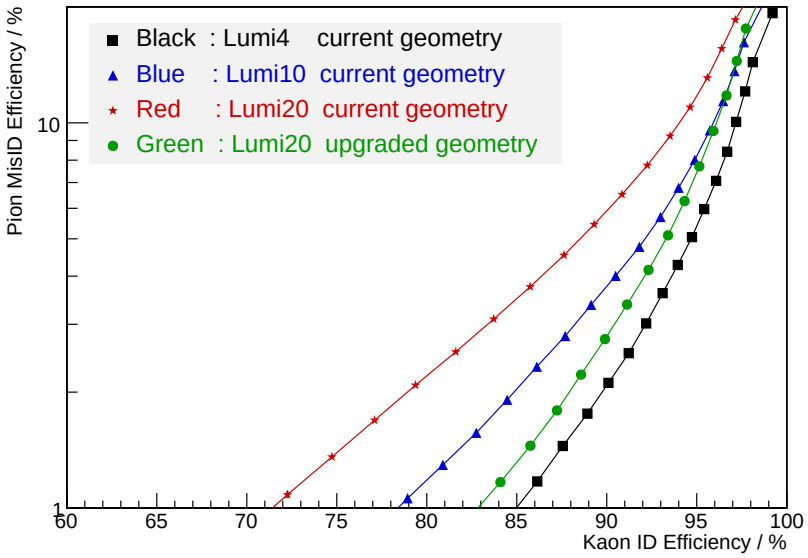

Figure 2.30: The PID performance of the current geometrical layout for Lumi4, 10 and 20. The performance from the upgraded geometry at Lumi20 is superimposed.

additional space for the electronics boards. By making these changes together, the RICH PID performance was restored.

- *Detector plane tilt:* The detector plane was tilted from its standard orientation by +25 mrad and -25 mrad. No change in PID performance was observed.

In Fig. 2.32 the kaon identification efficiency and pion misidentification probability are plotted as a function of the track momentum (with DLL cuts of 0 and 5) for the upgraded geometry and Lumi20 configuration. As the DLL cut increases from 0 to 5, the kaon identification efficiency and the pion misidentification probability both decrease as expected. This demonstrates the excellent performance to be anticipated from the upgraded PID system.

2.6 Project organisation

2.6.1 Schedule

The work programme and schedule of the RICH upgrade project is summarized in Fig. 2.33. It covers the period up to 2019, the time at which LS2 finishes and beam is delivered. The schedule is planned to ensure that the RICH detectors are fully commissioned and operating together with other LHCb sub-detectors at this time.

Critical tasks are the design and production of the new RICH 1 detector and the implementation of the MaPMT technology and its 40 MHz readout. The MaPMT production and testing will be carried out in parallel to electronics manufacture. Work on the backup HPD photon detector (with external readout electronics) and also the backup MAROC readout chip will be maintained until the end of 2014.

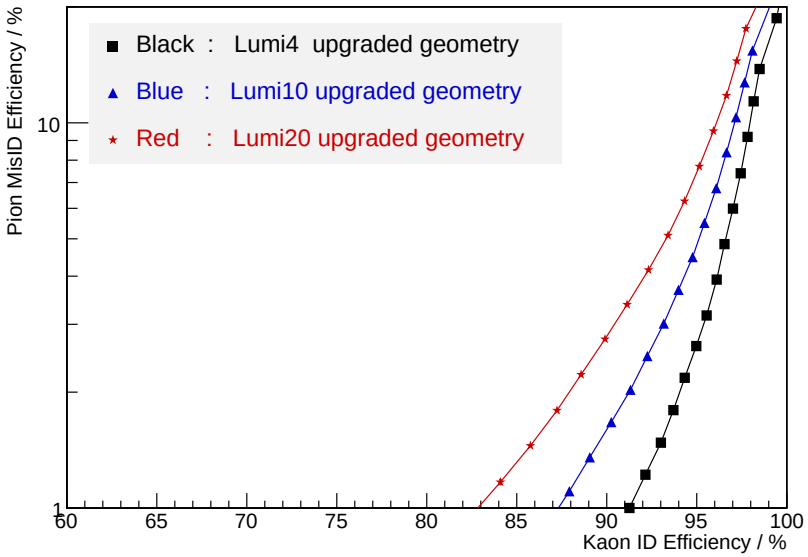

Figure 2.31: The PID performance of the upgraded geometrical layout for Lumi4, 10 and 20.

(i) Completion of R&D

Several of the tasks included in the schedule will involve further R&D prior to production.

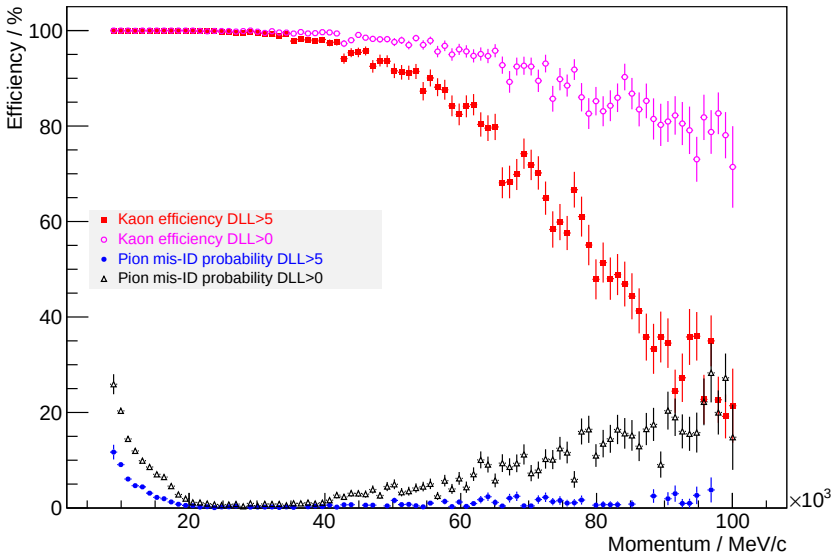

Figure 2.32: The kaon identification efficiency (magenta and red) and pion misidentification probability (grey and blue) as a function of track momentum for the upgraded geometry at Lumi20 (with DLL cuts of 0 and 5, respectively).

- *Final MaPMT qualification:* We foresee further evaluation of the R11265 MaPMT proceeding through Q2 2014. The MaPMT will be read out with the 8-channel prototype CLARO readout chip, studying properties such as signal to noise and cross talk. Extended lifetime tests will also be performed. We will also prototype the new range of MaPMTs, the Hamamatsu H12700 which is a candidate for the outer regions of RICH 2.
- *The CLARO chip:* We foresee detailed evaluation of the prototype 8-channel prototype chip to proceed through to Q3 2014, in parallel with the final chip design. Following a production readiness review (PRR) in Q1 2015, the chip will then be manufactured.
- *Readout electronics:* Prototypes of all front-end electronics components will be evaluated through to Q3 2014, in particular the MaPMT base-board and the MaPMT front-end ASIC boards. The digital board will be prototyped through to Q1 2015. This will culminate in a system test with prototype electronics in a test-beam in Q1 2015 to verify the complete readout chain.
- *Engineering designs:* The designs of the RICH 1 vessel, mirrors and their adjustable mounting system will be completed in Q1 2015, resulting in final production drawings for the RICH 1 PRR in Q1 2015. The design of the RICH 2 mechanics will proceed in parallel, resulting in a PRR on the same timescale.

(ii) Construction

The major construction tasks include:

- *Mechanics:* The RICH 1 vessels, superstructure, optics and photon detector mounting will require a production time of approximately two years, and will be completed during 2015/7. The production time of the RICH 2 MaPMT supports and modifications to the vessel have been estimated at around one year. Assembly of columns of MaPMTs with the associated front-end electronics and services for both RICHes will last around two years and proceed in parallel with MaPMT testing and production.
- *Photon detectors:* We assume a rate of production of ∼150 tubes per month, giving a total time of two years (years 2015-17). Systematic tests and certification of the photon detectors must follow the production process at the same rate. An extensive series of measurements of the photocathode response and the channel-to-channel gains will require at least two test facilities in the collaborating institutes.
- *Readout electronics:* The start of the CLARO chip manufacture is scheduled for Q2 2015, with a period of testing lasting around six months. The MaPMT front-end ASIC boards will be ready on the same timescale for population with the CLAROs, followed by further testing. The MaPMT baseboard manufacture will be completed by Q3 2015 to be ready for module assembly (with four MaPMTs per module in the elementary cell), followed by further testing, before assembly into 4×4 modules. Production of the readout electronics chain (from the digital board to DAQ) is scheduled to be completed by Q4 2016. The digital boards will be populated with chips that involve common LHC developments (TTC chipset, voltage stabilizers and the optical-link GBT chips). FPGA firmware will be written in parallel with board production. The RICH-specific TELL40 firmware will also be written in parallel for completion in 2017, ready for commissioning tests.

- *System tests:* Pre-production electronics components will be brought together in a full system beam test during the first half of 2015. For this test, an already-existing RICH demonstrator will be used, equipped with mirrors, photon detectors and readout. Following a successful system test, all components will be released for production. A second full system test with first production electronics will take place during the first half of 2016.

The aim is to re-use the current gas and cooling plants. The alignment systems for RICH 1 and RICH 2 will also be re-used. It is expected that the current monitoring system for RICH 1 will be replaced by a simple LED pattern generator, similar to RICH 2, to monitor MaPMT channel gains.

2.6.2 Installation and commissioning

RICH 1 installation will begin from early 2018. The upgraded detector will be partially assembled *in situ*. RICH 2 will remain in place, with just the photon detector regions removed for modification. Both RICH 1 and RICH 2 detectors will undergo commissioning during the second half of 2018. By early 2019, commissioning with other LHCb sub-detectors, using common DAQ, will begin. Six months of operation in this mode is foreseen to ensure the RICH detectors will be ready to take *pp* data by mid-2019.

2.6.3 Milestones

Key milestones for the RICH upgrade project are listed in Table 2.14.

Table 2.14: RICH project milestones.

Date	Milestone
	Mechanics and Optics
2015/Qtr 1	RICH 1 mechanical designs completed
2015/Qtr 1	RICH 2 mechanical designs completed
2018/Qtr 2	Begin Assembly RICH 1 in IP8
2018/Qtr 2	Begin Installation RICH 2 in IP8
	Photodetectors
2014/Qtr 2	MaPMT characterisation completed
2015/Qtr 1	Place MaPMT order
2017/Qtr 1	Production/testing completed
2017/Qtr 3	Module assembly completed
	Readout electronics
2015/Qtr 3	Baseboard manufacture and testing completed
2015/Qtr 4	CLARO chip manufacture and testing completed
2015/Qtr 3	MaPMT front-end ASIC boards manufacture and testing completed
2015/Qtr 3	System test of production electronics completed
2016/Qtr 4	Digital boards manufacture and testing completed
	RICH Detector commissioning
2018/Qtr 3	Begin commissioning in IP8
2019/Qtr 2	Commissioning completed

2.6.4 Costs

The costs for RICH 1, RICH 2 and services are shown in Tables 2.15, 2.16 and 2.17, respectively. This geometrical layout of the upgraded RICH system has been optimised for performance, and is the configuration to which all results presented in Sect. 2.5 relate. The cost estimates are based on quotes from industry or extrapolated from the costs of the current RICH system, corrected for inflation and exchange rate where appropriate. The full cost of the RICH system is estimated to be 9549 kCHF, shown in Table 2.18. A 15% level of contingency has been estimated from associated risk tables over the whole project, and includes possible currency fluctuations on the MaPMT purchase. When the above contingency and ∼11% spare MaPMTs are included, the total cost becomes 11644 kCHF.

For comparison, the cost of a scaled-down alternative configuration, is 8306 kCHF. Here the number of photon detectors in RICH 2 is reduced by ∼40% from 2560 to 1500 units with the introduction (and additional cost) of lenses. We are hopeful that this alternative configuration may be a realistic option, but more work is required to validate the geometrical layout and evaluate the PID performance. If the same percentages of spare MaPMTs and contingency are included, the cost of the alternative option becomes 10089 kCHF. The cost summary is given in Table 2.19. The reason for the cost of RICH 1 increasing when going to this option is that the cost of MaPMTs decreases for large bulk orders.

A third possibility is under consideration, where the number of MaPMTs in RICH 2 is reduced by ∼40%, as above, but also the number of MaPMTs in RICH 1 is similarly reduced by the use of lenses, from 1920 units to 1400 units, a ∼27% reduction. The cost would be 7404 kCHF, and when spare MaPMTs and contingency are included, the cost becomes 8970 kCHF. However, this configuration is high risk and will likely degrade the physics performance, but as before, this option has yet to be fully evaluated.

In conclusion, following further studies, we plan to select the most cost-effective solution which at the same time maintains the excellent PID performance.

2.6.5 Division of tasks

Institutes currently working on the LHCb RICH project are: CERN, The Universities of Bristol, Bucharest, Cambridge, Genova, Glasgow, Edinburgh, Ferrara, Krakow, Milano-Bicocca, Oxford, Padova, Imperial College (London) and the Rutherford Appleton Laboratory. A specific INFN section is associated to each Italian university.

The task-sharing matrix for the RICH project is listed in Table 2.20. It is not exhaustive, nor exclusive. For example software is clearly a major task, where it will be necessary to provide all RICH-specific software, for DAQ, monitoring, reconstruction, pattern recognition, and HLT trigger algorithms. The responsibilities for the HPD backup as specified in the table are limited to maintaining its viability until the end of 2014, by when the MaPMT technology, and the tendering process, should be confirmed. We adopt the same principle for the MAROC front-end chip.

There is sufficient manpower and expertise available within the institutes for these tasks to be executed within the required time-frame.

2.6.6 Safety aspects

The mechanical and electrical systems as well as the chemical, radiation and environmental aspects of the RICH detectors will comply with the appropriate CERN and European safety rules. The baseline document for CERN safety policy is the SAPOCO Ref. [50]. The relevant safety procedures are already in place for the current detector, and several issues have already been addressed above. Specific aspects of the RICH detectors subject to safety rules are listed below:

1. The Cherenkov (fluorocarbon) radiators and environmental gases: C_4F_{10} and CF_4, together with CO_2 and N_2. In particular the buffer tanks which are at high pressure.
2. Work procedures inside the gas enclosures of the detectors.
3. Fluorocarbon fluids and preservation of the environment.
4. Interventions close to the beam pipe and Beryllium safety. Also the general protection of the beam pipe.
5. The quartz windows, which isolate the photon detector environment from the gas enclosure.
6. Mechanical and load structures.
7. HV and LV systems.
8. Radiation safety.

For a detailed description see Ref. [51].

Table 2.15: RICH 1 project costs (Full RICH configuration) (kCHF).

Item	Unit	Number of units	Cost (kCHF)	Sub-total (kCHF)
Mechanics:				868
Gas enclosure	Piece	1	125	
VELO seal and exit window	System	1	Re-use	
Magnetic shielding	Piece	1	Re-use	
Spherical mirrors, frame & coating	Piece	4	342	
Plane mirrors	Piece	16	68	
Plane mirror support	Piece	16	38	
Photon detector assembly	Piece	2	130	
Quartz window incl. coating	Piece	2	60	
Photon funnel & quartz mounts	Piece	2	10	
Installation & maintenance tooling	System	1	95	
Photodetectors:				2156
MaPMTs	Piece	1920	2127	
Mumetal shields	Piece	480	29	
Electronics:				1543
CLARO chips	Chip	15360	146	
Base-board for elementary cell	Module	480	176	
MAPMT front-end ASIC boards	Board	3840	163	
Front-end digital boards incl. FPGA & GBT	Board	480	177	
Breakout fibres/connectors/patch panels	System	93	65	
Master links	Links	480	200	
Data links	Links	627	130	
Readout boards (TELL40)	Board	7	238	
TELL40 boards for ECS/TFC	Board	4	136	
Crates and power supplies	Crate	1	11	
HV distribution & cables	System	1	12	
HV power supplies	System	1	52	
LV distribution & cables	System	1	7	
LV power supplies	System	1	30	
RICH 1 TOTAL				**4567**

Figure 2.33: Schedule of RICH upgrade project, up to start of LHCb data taking in mid-2019.

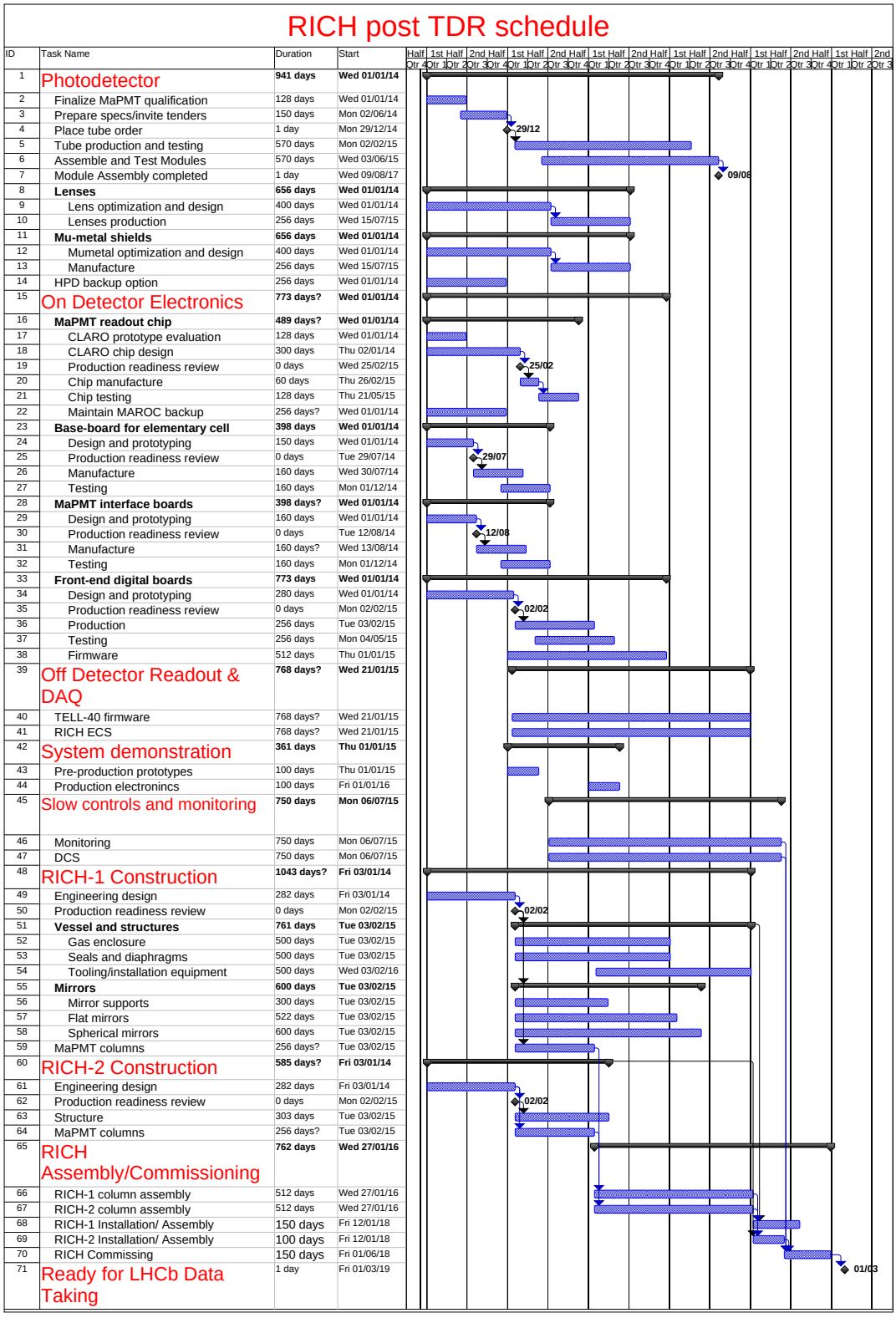

Table 2.16: RICH 2 project costs (Full RICH configuration) (kCHF).

Item	Unit	Number of units	Cost (kCHF)	Sub-total (kCHF)
Mechanics:				180
Gas enclosure, quartz windows & mirrors	System	1	Re-use	
Magnetic shielding	Piece	2	Re-use	
Photon detector assembly	Piece	2	180	
Photodetectors:				2874
MaPMTs	Piece	2560	2836	
Mumetal shields	Piece	640	38	
Electronics:				1873
CLARO chips	Chip	20480	195	
Base-board for elementary cell	Module	640	234	
MaPMT front-end ASIC boards	Board	5120	218	
Front-end digital boards incl. FPGA & GBT	Board	640	236	
Breakout fibres/connectors/patch panels	System	107	75	
Master links	Links	640	266	
Data links	Links	640	133	
Readout boards (TELL40)	Board	7	238	
TELL40 boards for ECS/TFC	Board	5	170	
Crates and power supplies	Crate	2	22	
HV distribution & cables	System	1	17	
HV power supplies	System	1	69	
LV distribution & cables	System	1	Re-use	
LV power supplies	System	1	Re-use	
RICH 2 TOTAL				**4927**

Table 2.17: Cost of services (kCHF).

Item	Unit	Number of units	Cost (kCHF)	Sub-total (kCHF)
Services:				55
MaPMT cooling system	System	1	50	
Detector control system	System	1	5	
Monitoring and alignment systems	System	1	Re-use	
SERVICES TOTAL				**55**

Table 2.18: RICH cost summary (Full RICH configuration) (kCHF).

Item	Cost (kCHF)
RICH 1	4567
RICH 2	4927
Services and DCS	55
Subtotal	9549
Spare MaPMTs (∼11%)	576
Contingency (15%)	1519
TOTAL	**11644**

Table 2.19: RICH cost summary (Alternative RICH 2 configuration) (kCHF).

Item	Cost (kCHF)
RICH 1	4825
RICH 2	3426
Services and DCS	55
Subtotal	8306
Spare MaPMTs (∼11%)	467
Contingency (15%)	1316
TOTAL	**10089**

Table 2.20: RICH project: sharing of tasks.

Task	Institutes
RICH 1 Mechanics:	
Entrance/exit windows and seals	RAL
Gas enclosure	Oxford
Mirror supports	Bristol
Mirror procurement, characterisation and testing	Bristol, CERN
Photodetector mounts and MaPMT housing	Imperial
Installation tooling	RAL
RICH 2 Mechanics:	
Gas enclosure interface & cabling	CERN
Photodetector mounts and MaPMT housing	Genova, Padua, CERN
Installation tooling	CERN
Photon detectors:	
MaPMT contractual issues	CERN
Photodetector test facilities & quality control	Edinburgh, Glasgow, Ferrara, Padua
Mu-metal shields and lenses	Edinburgh, Genova, CERN
HPD backup	CERN
Readout Electronics:	
Baseboard for the MaPMT elementary cell	Genova, Ferrara, Milano-Bicocca
CLARO chip	Milano-Bicocca, Ferrara, Krakow
MAROC chip backup	Bucharest, Cambridge, Bristol
Front-end interface boards	Milano-Bicocca, Ferrara
Front-end digital boards & firmware	Cambridge, Oxford
DAQ interface, links & TELL40	Cambridge, Oxford, Birmingham
HV distribution	Genova, CERN
LV distribution	Cambridge, Oxford
Detector control	Genova, RAL, Oxford
Radiators:	
Gas systems	CERN
Cooling:	
Cooling plant	CERN
On-detector cooling	RAL, Imperial, Padua, CERN
Experimental Area Infrastructure	CERN
Monitoring, Alignment, MDCS:	
Design & production	CERN, Edinburgh, Milano-Bicocca, RAL
Software:	
Monte Carlo	RAL, Padua
Reconstruction	Cambridge, CERN
Calibration	Oxford

2.7 Appendix: The TORCH detector

Due to the increased occupancy that will result from the higher luminosity of the LHCb upgrade, the aerogel radiator will be removed from the RICH system, as discussed in Sect. 2.1. As a result, positive kaon identification will only be possible above the Cherenkov threshold in the C_4F_{10} gas of RICH 1, namely 9.3 GeV/c. Good separation can still be achieved below this threshold for isolated tracks, through the "veto" mode of operation, where those tracks with associated Cherenkov photons are taken to be pions, and those without photons as kaons, but this will become more challenging as the occupancy increases.

An alternative approach to low-momentum particle ID in the upgrade is being investigated, using time-of-flight. The difference in arrival time of kaons and pions over a distance of ∼10 m is about 40 ps at 10 GeV/c, and measuring this will require a resolution beyond the current state of the art. The TORCH (Time Of internally Reflected CHerenkov light) detector has been proposed [53], using the Cherenkov light produced by charged particles as they traverse a thin (∼ 1 cm) quartz plate. The photons will propagate to the edges of the plate by total internal reflection, and their arrival time measured using fast photon detectors. As about 30 photons can be detected per track, the time resolution requirement per photon is not so severe, about 70 ps.

To determine the time-of-propagation of the photons in the quartz plate, their angles need to be measured with a precision of about 1 mrad in both projections. Knowing the impact point of the track, the angle in the plane can be determined with a relatively modest granularity, of about 6 mm, due to the long lever arm. A focusing system is used to measure the other angle, with a cylindrical lens, and fine granularity of the photon detector in the corresponding dimension. The proposed layout of a TORCH module is shown in Fig. 2.34 (a). The time-of-propagation depends on the wavelength of the photons, but this will be determined by measuring their Cherenkov emission angle with respect to the charged particle track. The time-of-propagation through the quartz radiator differs for pions and kaons due to their different Cherenkov angles, and this time difference adds to the intrinsic time-of-flight difference due to the particle flights to the TORCH

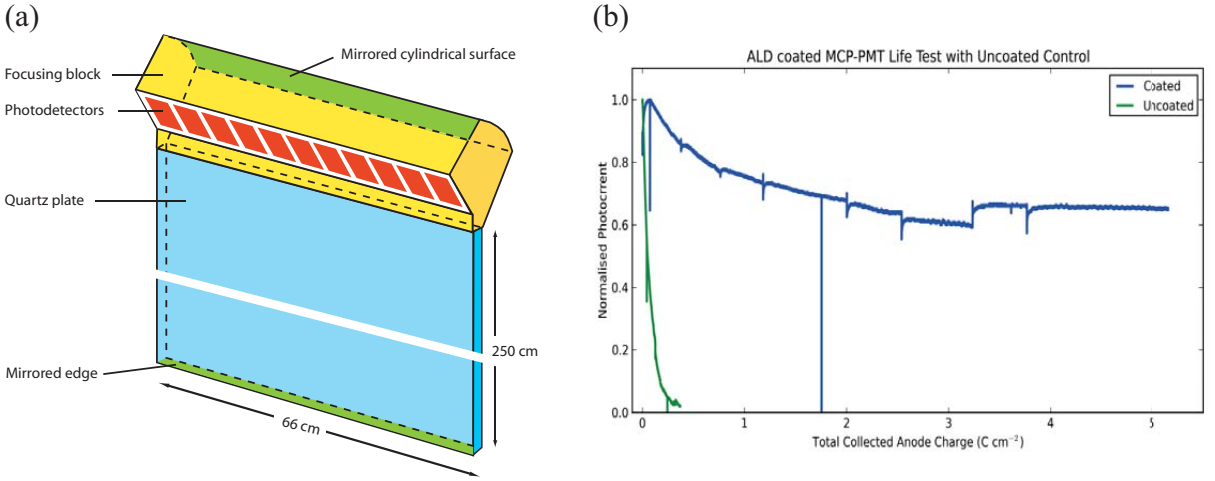

Figure 2.34: (a) Schematic layout of a TORCH module. (b) Photocurrent as a function of total integrated anode charge, in a life test of two MCP tubes, one ALD coated (blue line) and one uncoated as a control (green) [52].

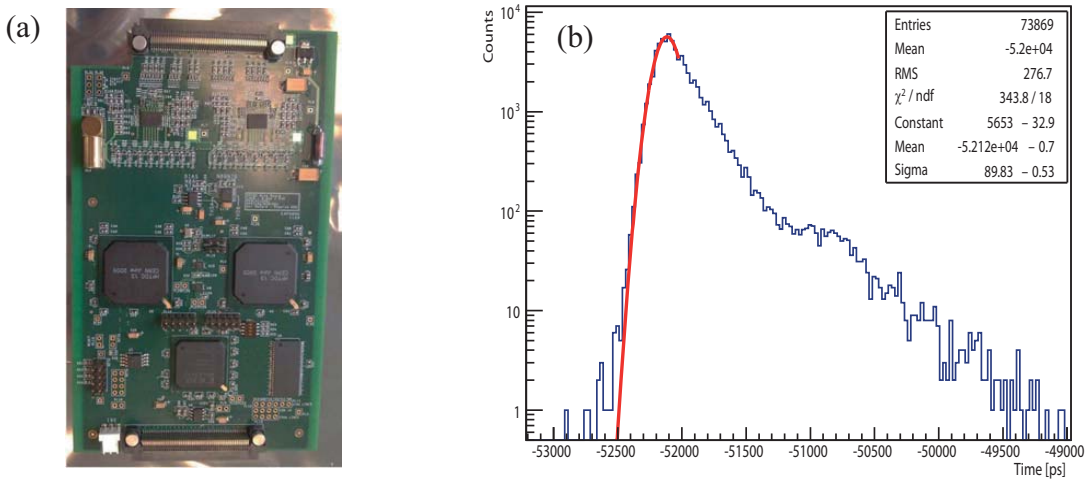

Figure 2.35: (a) Prototype MCP readout board operating at 25 ns and with high resolution (25 ps). (b) Timing resolution achieved for single photons from an MCP tube read out with this board; the tail to longer times has contributions from laser after-pulsing, and from backscattering in the MCP (note the logarithmic scale).

plane. Therefore the overall separation power of the TORCH system is greater than if there was only the time-of-flight alone.

The most promising photon detector for this application is the micro-channel plate (MCP) photomultiplier tube, which has been demonstrated to provide better than 50 ps timing resolution for single photons [7]. High-granularity commercially available tubes exist, such as the Planacon[9] with 32×32 channels, but the high resolution required for TORCH corresponds to 128×8 channels within the same tube dimension (59 mm square, with 53 mm active area). There is also a challenging requirement on the lifetime of the tube in the LHCb upgrade environment, which corresponds to an integrated charge of $\sim 5\,\mathrm{C/cm^2}$ at the anode.

An R&D project has therefore been established, focused on development of a suitable photon detector for the TORCH application. It is a collaboration of groups working on the LHCb RICH system from CERN, Bristol and Oxford Universities, and has been funded by the ERC for a four year period [54]. In the first year (up to present), an industrial partner has been selected[10] and the first tubes have been produced that are currently under study for the lifetime requirement. This has been achieved using an atomic-layer deposition (ALD) technique to coat the micro-channel plates, as shown in Fig. 2.34 (b). Over the next year the high granularity anode will be developed, and finally square prototype tubes will be produced satisfying both lifetime and granularity specifications. In parallel the optical system will be developed, with the final deliverable of the R&D project being a prototype TORCH module in 2016.

The timing performance has been investigated with a version of the Planacon MCP segmented as an array of 8×8 square pads, each ~ 6 mm in size [55]. A front-end electronics board has also been developed [56] and is shown in Fig. 2.35 (a). It comprises fast amplifiers/discriminators

[9] Burle/Photonis, Lancaster, PA17601-5688, USA.
[10] Photek Ltd, St Leonards on Sea TN38 9NS, UK : `http://www.photek.com/`

with time-over-threshold information (NINO [57]) and time digitizers (HPTDC [58]) with 25 ps time resolution. The Planacon is operated at modest gain ($100\,\text{fC} = 6 \times 10^5\,\text{e}^-$). The light source is a pulsed (20 ps) laser diode emitting at 405 nm and the light intensity is tuned to reach the single-photon regime. In this configuration, a time resolution of 90 ps has been achieved for single photons, as shown in Fig. 2.35 (b). No correction has yet been applied for time-walk effects induced by MCP gain fluctuations, nor for the HPTDC non-linearity. The efficiency of detecting a photoelectron is estimated to range between 70 and 80% for a NINO threshold of 50 fC. This efficiency is expected to improve after optimization of the threshold setting. A new iteration of the front-end electronics is under development, that will use an improved 32-channel version of the NINO ASIC [56].

Assuming that the R&D is successful, a proposal will be made for inclusion of the TORCH detector in the LHCb upgrade, although this is unlikely to be in time for the first installation of the upgraded detector in the second long shutdown of the LHC (LS2). However, since TORCH is a thin plane, it should be feasible to insert it at a later date. The planned removal of the first muon station (M1, visible in Fig. 2.1) will provide ample room along the beam direction. The full TORCH system would require 18 identical modules, for a total of about $30\,\text{m}^2$ of quartz and 200 MCP tubes.

2.8 Appendix: An HPD with external readout

The concept of HPDs with external readout electronics has been demonstrated in the past [59–62]. Compared to the pixel HPDs which equip the current LHCb RICHes, external readout has a significant advantage of decoupling photon detector and front-end electronics developments. The overall design of the HPD tube for the upgrade would be similar to the design of the current pixel HPDs, allowing a significant fraction of the existing photon detector infrastructure to be retained. The main difference would be in the anode part; the tube would only encapsulate in the vacuum an array of 490 hexagonal silicon pads, each 0.8 mm flat-to-flat in size (~ 3.2 mm at the photocathode after electrostatic magnification). The pads are connected to signal lines routed out to external readout electronics through a ceramic carrier. The HPD signals are input to a low-noise charge-sensitive preamplifier and subsequently fed to a discriminator for binary readout. The front-end electronics would then be similar to what is required for MaPMTs.

Given the uniform but limited charge signal ($5000\,e^-$) from an HPD and the required signal-peaking time of ~ 25 ns, the key point is to maintain an acceptable signal-to-noise ratio in this configuration. In this respect, the capacitive load to the input of the charge preamplifier should be minimized. Extensive carrier design studies showed that the additional capacitive load from the routing lines may be limited to a few pF while cross-talk effects are kept minimal through the use of transmission lines, each surrounded with guard lines and embedded within ground and bias planes. For the HPD readout, a possible front-end candidate is the SALT ASIC chip [63] under development for the Upstream Tracker. Given the limited charge signal from the HPD, the front-end design of that chip would however require further optimization in terms of noise.

The proof-of-concept has been investigated using an HPD with 163 hexagonal pads [61]. The individual pad size is 1.4 mm flat-to-flat. The HPD also implements getter strips, a feature recently and successfully developed for the re-processing of pixel-HPDs which now results in very low ion feed-back rate. The external front-end electronics is based on the Beetle ASIC chip [64] used in the LHCb VELO detector and the ALIBAVA portable readout system [65]. The HPD is coupled to this electronics through an interface printed-circuit board, wire-bonded to the ALIBAVA daughter board which is populated with two Beetle chips. In this test configuration, the total capacitive load per channel is not fully optimal and is estimated to be at least 10 pF.

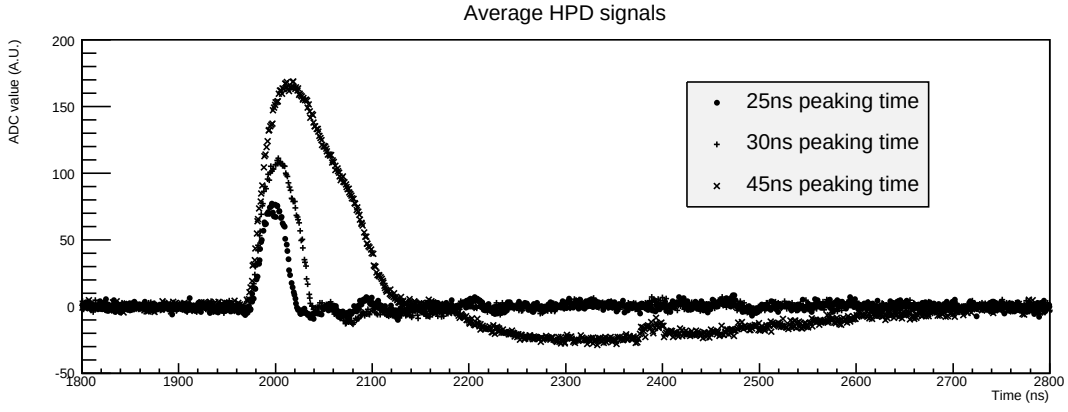

Figure 2.36: Average HPD signals for single photons for three different Beetle settings. The peaking times are 25 ns, 30 ns and 45 ns. Note the long undershoot for the signal with 45 ns peaking time.

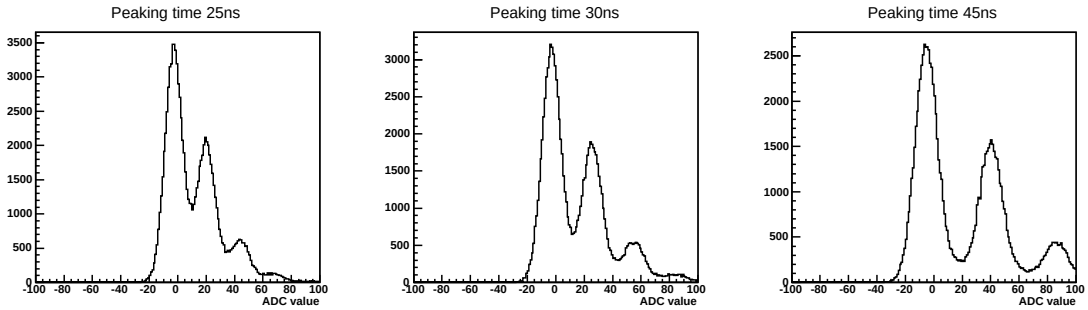

Figure 2.37: Photoelectron spectra corresponding to the three different peaking times of Fig. 2.36. Note the presence of an irreducible background continuum due to photoelectron backscattering on the silicon detector.

The performance for photon counting has been assessed for three different Beetle settings corresponding to the three output signal profiles reproduced in Fig. 2.36. The peaking times are 25 ns, 30 ns and 45 ns. The HPD was illuminated with a fast pulsed laser diode emitting in the blue (405 nm). The light level per pixel was of order 0.5 photoelectron per laser pulse. The resulting photoelectron spectra from the central pad are illustrated in Fig. 2.37. Assuming a charge signal of 5000 e^- per photoelectron, the RMS noise is estimated to be 1390 e^-, 1180 e^- and 860 e^- for 25 ns, 30 ns and 45 ns peaking times, respectively. These preliminary results are in agreement with the estimated capacitive load and the Beetle noise performance. Optimization of the current system is required through e.g. a redesign of the front-end board that would reduce the capacitive load to the Beetle chips. However, a fully satisfactory performance would be achieved only through the availability of a dedicated HPD anode and front-end electronics. Design studies for such dedicated developments are on-going.

Chapter 3

Calorimeter system

3.1 Introduction

The LHCb calorimeter system [66] has performed very well throughout the first years of LHC operation. This good performance has been achieved despite the decision to operate the experiment at a higher luminosity than was foreseen during the design period [67]. New challenges, however, must be overcome at the upgraded experiment. Here, the calorimeter must be able to survive several years of operation at an instantaneous luminosity up to a maximum of $2 \times 10^{33}\,\mathrm{cm}^{-2}\mathrm{s}^{-1}$ and continue to deliver efficient photon and electron identification under these conditions. Furthermore, the readout must be performed at a rate of 40 MHz, and the calorimeter system must contribute to the LLT, the new hardware trigger which will filter the events that are to be processed further in the software-based trigger of the PC farm.

Here we summarise the key points of the calorimeter upgrade programme and highlight certain decisions that will be justified and expanded upon in the discussion that follows.

- The change to the readout strategy necessitates a complete redesign and rebuilding of the front-end and back-end electronics. An additional consideration in this redesign comes from the decision to reduce the gains of the PMTs to ensure a longer lifetime for high luminosity operation. This reduction in PMT gain must be compensated by a gain increase in the electronics. The plans for the electronics of the upgraded detector are presented in Sect. 3.2.

- A measurement campaign and simulation studies have been used to assess the effects of the radiation dose that the calorimeter system will experience. It is concluded that although certain elements of the system will need replacing, the modules themselves will survive throughout the first period of upgrade operation. Eventually some of the cells in the inner region of the ECAL will need replacing, but this operation need not be performed until Long Shutdown 3 (LS3). These topics are discussed in Sect. 3.3.

- As was already proposed in the LoI and FTDR [8, 68] the scintillating pad detector (SPD) and the preshower (PS) of the current detector will be removed. The principal purpose of these components in the current experiment is in the L0 trigger. The LLT of the LHCb upgrade will not have to achieve the same level of suppression, and hence the requirements on the calorimeter system are less stringent. The removal of the SPD/PS simplifies the calorimeter system, with benefits for calibration and project costs. Nevertheless, there are

some consequences for the offline performance. These are assessed in simulation studies, described in Sect. 3.4. In the same Section are reported investigations into the overall performance at high luminosity in terms of clustering efficiency and PID.

Finally, safety consideration are addressed in Sect. 3.5.3 and the project organisation is discussed in Sect. 3.5.

3.2 Electronics

The upgraded LHCb calorimeter system is made of two sub-detectors, the ECAL and HCAL, whose modules remain mostly unchanged with respect to the present system (see section 3.3.1). Likewise, the photo-multipliers (PMT) are kept, their gains being reduced by a factor five after the luminosity increase foreseen in the upgrade to keep the same mean anode current as presently. The 40 MHz readout of the data requires a new design of the front-end and back-end electronics. A total of 238 new Front-End boards (FEB) is necessary to perform the acquisition of the modules. Each FEB is designed to receive the signals of 32 PMTs. The boards are distributed in 18 crates: 14 for the ECAL and 4 for the HCAL. A new control board located in the central slot of each crate must also be designed. It will receive the clock, slow and fast control signals from the Timing and Fast Control system (TFC) of the experiment and propagate them to the FEB via the backplane. This architecture is compatible with the parts of the existing electronics that will be kept for the upgrade (backplanes and crates, for example) in order to reduce the cost of the project.

3.2.1 Front-End board

(i) Analogue processing

The analogue signal processing on the Front-End board is mostly performed by a circuit that integrates the PMT signal pulse. The signals are transmitted through a 12m, 50Ω coaxial cable from the detector to the FEB located in the crates on the platform, above the calorimeter system.

Table 3.1: Summary of the requirements for the calorimeter analogue Front-End.

Parameter	Requirement
Energy range	$0 \leq E_{\mathrm{T}} \leq 10$ GeV (ECAL)
Calibration/Resolution	4 fC/2.5 MeV per ADC count
Dynamic range	4096-256 = 3840 cnts: 12 bits
Noise	$\lesssim$ 1 ADC cnt (ENC $<$ 4 fC)
Termination	$50 \pm 5\ \Omega$
Baseline shift prevention	Dynamic pedestal subtraction
Max. peak current	4-5 mA over 50 Ω
Spill-over residue level	$\leq 1\%$
Non-linearity	$< 1\%$
Cross-talk	$< 0.5\%$
Timing	Individual (per channel)

As the calorimeter measurement must be performed at every bunch crossing (at 40 MHz), the system must minimise any spill-over effects and the PMT pulses are therefore shaped so that the tail extending after 25 ns is not larger than 1% of the signal. Table 3.1 specifies the main requirements on the upgraded front-end electronics.

Compared to the existing design, the gain of the PMTs has to be reduced by a factor five so that they can be kept during the upgrade period, the gain being compensated in the electronics, since the electronic amplifier gain must be increased by a corresponding factor of five. As a consequence, an equivalent reduction of the electronics noise is needed to maintain the same performance. The first step of the pulse shaping consists in clipping the signal [66]. This is performed on the PMT base, before any amplification. Such an early clipping is not compatible with a passive termination at the FEB input stage, if the noise has to be significantly reduced with respect to the previous calorimeter electronics design [69]. However, an active termination will permit the clipping to be kept unchanged and will require no intervention on the PMT base. As the implementation of an active termination requires a transistor level approach and as a FEB serves 32 channels, an ASIC, termed the ICECAL, is being developed.

Nevertheless, a different approach is also under consideration. Currently the PMT signal is clipped in the base, and about 2/3 of the signal charge is lost. An alternative solution would consist of postponing the clipping until after the amplification of the signal, on the FEB. This would relax by a factor three the noise requirement on the frond-end amplifier, thus allowing a passive termination. This solution requires a simple intervention on the detector and is implemented with Commercial Off-The-Shelf (COTS) operational amplifiers and analogue delay lines.

The two solutions are discussed in the following sections. A choice will be made between these options in the middle of 2014, when a significant sample of boards based on both implementations has been assembled and evaluated.

ASIC implementation The stages of the ASIC solution, named the ICECAL, are depicted in Fig. 3.1. It includes two alternated switched signal paths where the input current is first amplified and converted to differential signals in order to be integrated through a fully differential amplifier with capacitive feedback. The integration is performed by two alternate integrators running at 20 MHz, one being readout and reset while the other is active. A fully differential signal processing is adopted in order to minimize the impact of common mode noise, which can be significant in a switched system. The input stage is a current pre-amplifier with an electronically cooled termination (the input impedance being adjusted dynamically by active components) to reduce the noise. A pole-zero filter stage helps to remove the distortions produced by the twelve metre cable. Then, the signal is integrated with the switched integrators. A track-and-hold samples the integrated signal and the analogue multiplexer selects the correct sub-channel to be processed further.

The input amplifier is made of a regulated common base input stage with double feedback and an electronically cooled termination. Two current feedback loops are used to decrease and control the input impedance of a common base transistor with emitter degeneration and provide additional transconductance linearisation. The assets of the current mode implementation are its lower voltage, DC coupling (no external components or additional pads), the low impedance of all nodes (less prone to pick up noise), and improved ESD robustness (no MOS transistor gate or bipolar base is connected to the input pad).

The switched integrator is based on a fully differential operational amplifier (FDOA), feedback

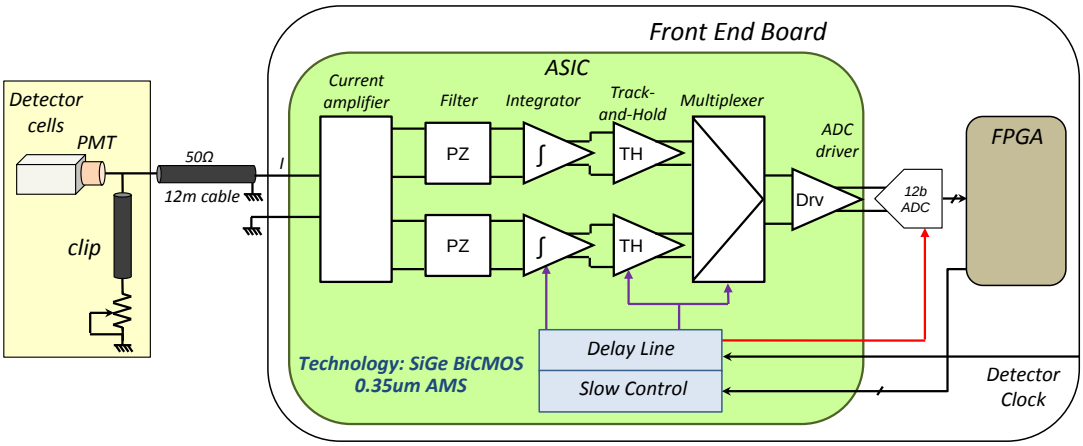

Figure 3.1: ASIC solution schematic.

capacitors, discharge resistors, and CMOS switches to perform the operation. The FDOA consists of a bipolar pair input with emitter degeneration, a folded cascode stage, a second Miller stage with a bipolar output in common-emitter amplifier configuration, and a common mode feedback circuit [70]. It has a gain bandwidth of 500 MHz, a DC gain of more than 70 dB, a phase margin larger than 65° and a slew rate better than 0.4 V/ns, for moderate capacitive loads (below 15 pF). Feedback switches are on during the integration cycle. When the integration finishes, the reset cycle starts: two switches connect the inputs to ground and the feedback switches are off. In order to obtain a fast reset and avoid residual amplification, fast discharge switches are used. The integrator capacitors are discharged in less than 10 ns.

A track-and-hold providing a stable output is added after the switched integrator. Its specifications are defined by, firstly, the accuracy required for 12 bits, and secondly, by limiting the use of half of the clock cycle for settling the output signal. It is based on the flip-around-architecture [71] with bottom plate sampling as this helps in reducing the tracking capacitor charge error and ensuring better linearity. The feedback design is preferred with respect to an open loop to improve the linearity and the accuracy. The FDOA used for the integrator is also used for the track-and-hold.

As each channel of the detector possesses different latencies because of the differences in the PMT high-voltage, the time of flight of the particles reaching the calorimeter surface and the length of the signal cables, it is necessary to adjust the integration time for each one individually. The exact delay is hard to evaluate at design time and thus tunable delays are required. The need to automate the time adjustment procedure and the limited accessibility of the electronics imply using digital programmable delay lines, which are included in the ASIC. Each channel includes a DLL (Delay Lock Loop) which generates three independent LVDS (Low Voltage Differential Signal) clocks with configurable phases in order to delay the LHC clock by intervals of 1 ns, between 0 and 24 ns, for the switched integrator, the track-and-hold, and the external ADC. The DLL implementation is fully differential, so that the switching noise is lower in comparison to a single-ended implementation. This block receives the reference differential CMOS clock

signal that passes through a Voltage Controlled Delay Line (VCDL), then a multiplexer selects the desired output and implements the phase comparator which generates the fine-grain control voltage. Two signals, V_{coarse}, which is an external and fixed bias voltage, and V_{control}, ensure that the introduced delay by each VCDL stage is 1 ns.

Two versions of ASIC prototypes have been designed, fabricated and tested in Austriamicrosystems 0.35 μm SiGe BiCMOS technology. This technology allows a 3.3 V operation and has fast HBT transistors, which are useful for the high dynamic range of our system. In particular the high transconductance versus bias current ratio of bipolar transistors is very useful for achieving good linearity in current mode solutions.

COTS implementation By removing the clipping from the PMT base and performing it at the front-end level, the signal to noise ratio at the input stage is improved. Removing the clipping by cutting a PCB track on the bases is a simple operation but quite time consuming when done for almost 8000 PMTs mounted on the ECAL and HCAL modules. The replacement of the PMT bases is not foreseen as it would require a much more involved operation on the detector with a higher risk for its integrity. Under these conditions the actual clipping-subtraction-integration scheme can be kept, provided all steps are performed at the FEB level. Delay lines are necessary in this case and a discrete component solution, with COTS, is envisaged [72]. Its scheme is shown in Fig. 3.2.

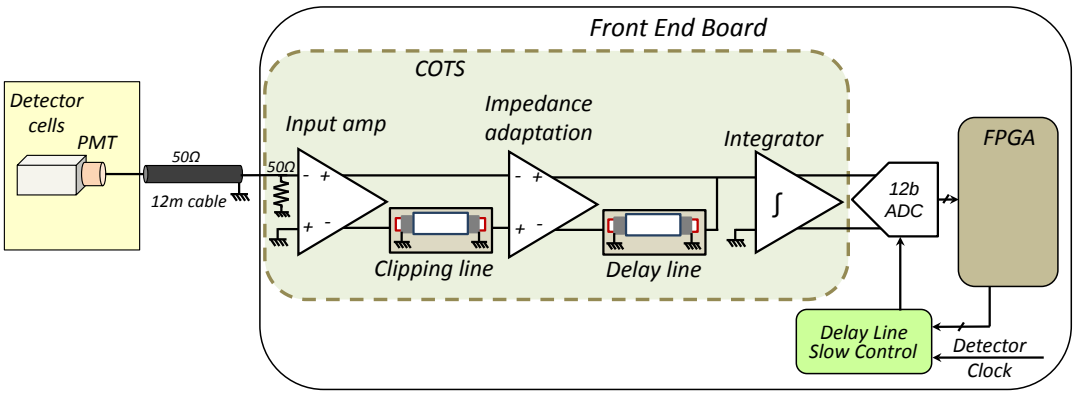

Figure 3.2: COTS solution schematics.

With the clipping being performed on the FEB, the amplification of the input signal takes place earlier. To avoid that the noise is amplified in irrelevant parts of the spectrum, it is important that the first amplifier has low noise and not too large a bandwidth. The scheme used to clip the signal on the FEB is composed of a first amplifying stage followed by an operational amplifier subtracter that receives appropriately scaled and delayed signals. This clipping scheme is similar to the one described in Ref. [66] but using differential operational amplifiers to generate both polarities for the signals instead of using transmission line reflections. The parameter values are chosen after studying the response to the actual signal shape in order to obtain the desired clipping.

The next step in the analogue processing is the integration, which is performed by a differential

operational amplifier with capacitive feedback loop. Its structure is similar to the clipping one. The main difference is that the delay line is much longer (25 ns) and that there is no attenuation. The clipped signal is integrated and then disintegrated dynamically with a 25 ns delay without involving any switch.

Then, the analogue levels are adapted to the ADC input through AC coupling and bias resistances. Some drawbacks must be taken into account. The system is AC coupled and thus will suffer a baseline shift. The shift will depend on the pulse amplitude, the pulse rate and the speed at which the capacitors discharge. Hence, relatively big capacitors have been chosen for this purpose, both because they should have a small influence in the concerned frequency domain and because, in the time domain, undershoots will last longer and have a lower amplitude. However, the related time constant has been limited to 5 μs in order to minimize the effects on the baseline shift of the empty bunch crossings related to the gap in the LHC bunch structure. This affects the ADC adaptation specifically, but may also be applied to the rest of the AC coupling of the system. Five percent of the dynamic range of the ADC has been reserved to prevent any saturation and furthermore an extra two percent have been reserved for the noise.

Finally, special care has been taken to keep the inputs of the operational amplifiers balanced. Both polarities have equivalent impedances. The power integrity and EMI (ElectroMagnetic Interference) have been carefully studied to avoid ruining the low noise performance with external interferences.

Prototype performance results In November 2012, the beam line T4-H8 at CERN Prevessin was used for a test beam. An ECAL module equipped with a PMT and its base was used to detect the signal from electrons ranging from 50 to 125 GeV. The acquisition was triggered using two scintillators in coincidence and the signal sent to the FEB prototype, equipped with the two analogue solutions described above and in parallel, to a Lecroy integrator and a Time-to-Digital Converter (TDC) in the barracks.

Hence, the experimental setup included two parallel measurements of the signal of the PMT to perform the envisaged tests and comparisons. The TDC was needed to measure the phase between the individual particle time arrival and the 40 MHz clock used by the FEB prototype.

The measurements of noise, resolution, linearity, spill-over, and integrator plateau showed behaviour within specifications except for what concerned the integrator plateau and spill-over. The cable and clipping effects had been under-estimated leading to a signal pulse wider than expected. To overcome this problem in future, it is proposed to implement a pole-zero filter for both analogue ASIC and COTS solutions which allows the tail to be reduced and the specifications to be met.

Figure 3.3 shows the detail of two measurements. The low frequency contributions to the noise are suppressed by a pedestal dynamic subtraction (consisting of subtracting the lowest of the two previous samples to the signal) that will be implemented in the digital processing of the FEB but which is performed here offline. The remaining noise is measured to be 1.4 and 2.3 ADC counts respectively for the ASIC and the COTS solutions. The former is shown in Fig. 3.3 (a). In order to cope with the expected time fluctuations of the pulse, the output of the integrator must be stable (*i.e.* must vary by less than 1%) in a $\pm$2 ns wide plateau. To obtain the plateau shape, the data are fitted with a Gaussian function. The relative variations with respect to the maximum at $\pm$2 ns showed a difference of about 1.5% and 1% respectively for the ASIC and the COTS implementations, as can be seen in Fig. 3.3 (b). Simulations indicate that the plateau is improved significantly with the pole-zero filter described above.

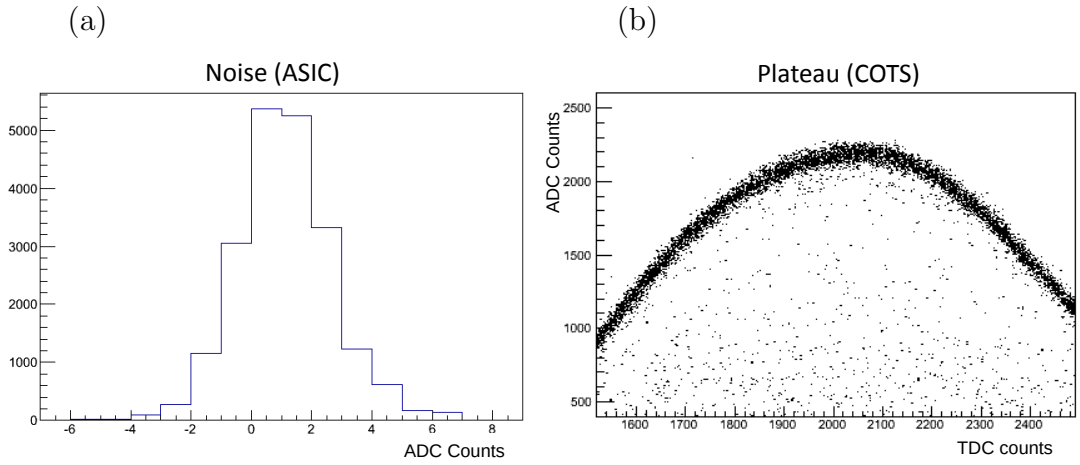

Figure 3.3: (a) ASIC electronics noise after pedestal dynamic subraction. 1 ADC count corresponds to a transverse momentum of ∼2.5 MeV. (b) Data points around the maximum value, in the region of the integrator output plateau, for the COTS solution (ADC vs. time).

(ii) Digital processing

The design of the digital part of the FEB for the LHCb calorimeter upgrade is inspired by the experience with the current electronics FEB [73, 74]. Each front-end board handles 32 channels. The digital part of the FEB is composed of four major components.

- The Front-End-PGA (FE-PGA) [75] processes 8 channels and receives the data from 8 ADCs, each with a 12 bit digitisation. It consists of six firmware blocks: data synchronisation, pedestal processing, trigger processing, event building (bunch crossing identification tag), handling the test and TFC signals and sending the data to the GBT [76] at 80 MHz after serialization. It should be noted that there is no need to pipe-line the data in the FE-PGA as the system is synchronous.

  The analogue chips, the ADC, the GBT and an optical emitter/fibre, and the FE-FPGA together constitute a FE-Block. There are four such blocks on a FEB (see Fig. 3.4).

- The Trigger-PGA (Trig-PGA) [77] handles the processing of the LLT on the board. It receives the results of the trigger calculations of the FE-PGA and sends its data to the fifth GBT/optical link of the FEB.

- The Control-PGA (Ctrl-PGA) synchronises the processing of the components of the board. It is in charge of the global control and correlates information from several FE-PGAs in order to check the overall processing of the FE-blocks. It also distributes the TFC signals to the components of the FEB.

- The power and slow control blocks consist of DC-DC converters, power protection systems, and a GBT-SCA driving JTAG, I^2C, SPI, and parallel bus.

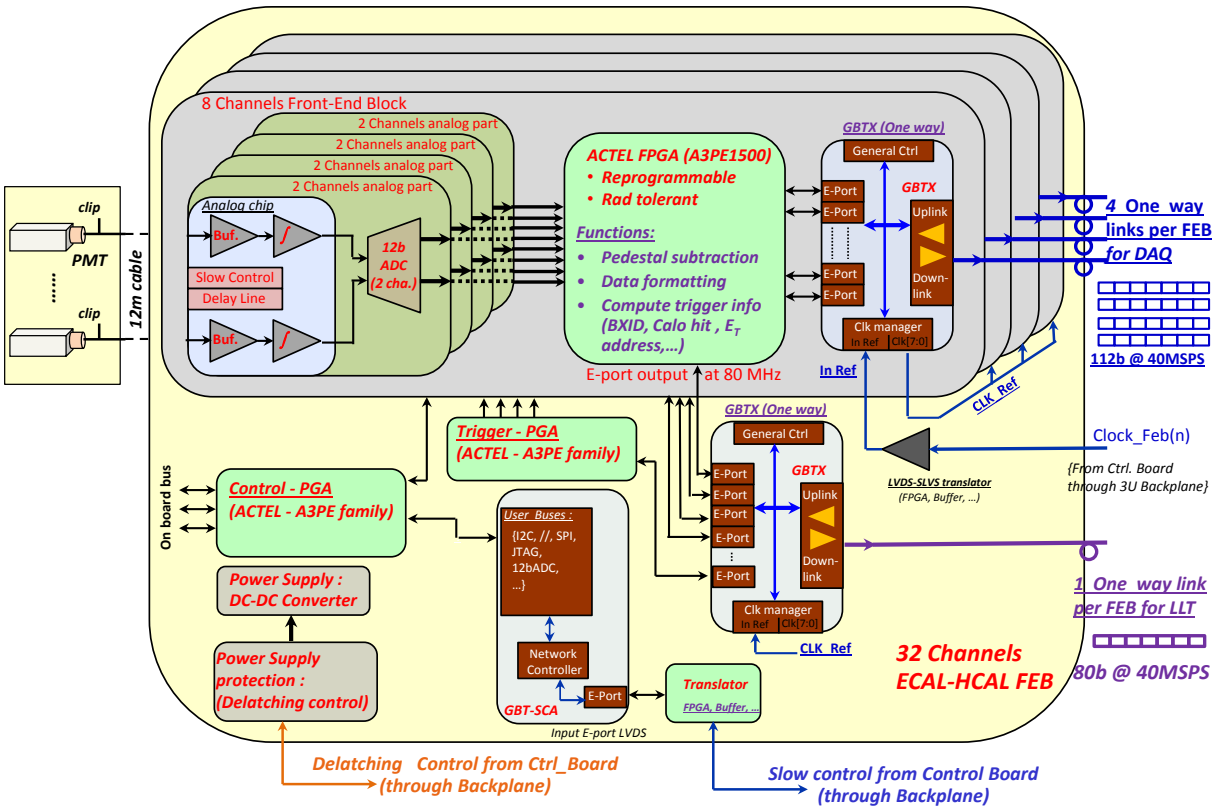

Figure 3.4: Diagram of the constituent blocks of the FEB.

Figure 3.4 shows the different components of the FEB. The radiation tolerance constraints on the PGA of the board are such that the simplest and safest solution is at present the A3PE chip from MICROSEMI. The most suitable FPGA of the A3PE family is the A3PE1500.

Data processing The ADC of the FEB will receive a phase adjustable clock in order to sample the PMT pulse at the proper time. As the timing of the signal from different channels is different (see Sect. 3.2.1 and Ref. [78]), the first step consists of synchronizing the input data before any further processing of the FPGA, avoiding any bunch crossing de-synchronization among the channels.

The low frequency noise removal is performed by using the same techniques as those used for the current electronics and consists of subtracting the pedestal dynamically and synchronously. Two methods are foreseen.

1. The smallest of the two previous measurements for each channel is assumed to be the pedestal and is systematically removed. This method relies on the relatively low occupancy of the channels and slightly under-estimates the mean pedestal (by around 0.5 ADC counts at present) since it preferentially chooses negative noise fluctuations. This small bias can

be corrected in the offline reconstruction.

2. The second method estimates the pedestal by taking whichever is the lowest of the previous pedestal (plus a constant – typically 2 or 3), and the previous measurement. This technique is less sensitive to the occupancy and is robust against big fluctuations. However, it depends on the history of the system and is more difficult to emulate and debug.

Both methods are at present implemented in the current electronics. The former is the default one for data taking in the current experiment. The latter has been tested during the high luminosity and pile-up LHC runs of 2013. From studies performed on the π^0 mass and width, both methods give equivalent results. Notice that in the case of the ASIC analogue electronics the fact that the pedestal could be different for the two interleaved integrators means that the described must be performed per sub-channel.

The subtraction methods could potentially produce negative values that are difficult to treat. Hence, the data will be shifted by a value (~ 256) and treated as a 13 bit number until the subtraction is performed, the final result being in the range $[0, 4095]$ with a mean pedestal of ~ 256 and the effective dynamics being marginally reduced. For debugging purposes only, a third mode will also be implemented where no subtraction is applied.

Trigger processing The task of the trigger processing in the FE-PGA is to provide roughly calibrated 8 bit values of each channel treated by the FEB, eventually multiplexed at 80 MHz, as in the current implementation. The values are obtained by dividing the 12 bit ADC values of the data path by a 8 bit programmable calibration constant, and saturate at 255. The same mechanism will be used as in the current design [79]. These values will be then provided for the calorimeter Low Level Trigger (LLT) computations (see Sect. 3.2.1).

Event building and handling of the synchronous TFC signals The original design of the GBT system from CERN had a data rate of 80 bits at 40 MHz per fibre. This design would have forced us either to add a fifth optical link or to develop a sophisticated packing algorithm in order to send the calorimeter data. The risk in terms of overflow of the packing would be limited at $\mathcal{L} = 1 \times 10^{33}\text{cm}^{-2}\text{s}^{-1}$ but would not be negligible at twice that value. Fortunately, the final design of the GBT includes a new data format (called wide bus) that increases the data rate to 112 bits at 40 MHz. We plan to use this mode for the acquisition path and hence no packing is necessary any more, reducing the risk of data corruption. Finally, four optical links are needed for the data acquisition and each optical link will be part of a FE-block and connected to a single FE-PGA.

With each link treating 8 channels (12 bit ADC), $12 \times 8 = 96$ bits are needed. Out of the 112 bits available, 16 remain that will be used for crate numbering (5 bits), FEB numbering (4 bits) and the bunch crossing identification number necessary to check the data synchronization (7 bits). Note that the LHC bunch crossing number is coded on 12 bits and so not all of them can be sent together. Several options are being considered to include these data into the frame: sending only the 7 lower significant bits would be adequate to test for most of the synchronization problems that we may expect, or sharing the bits among the remaining bandwidth of each link of the board.

The data format described here supposes that the bunch crossing identification number is determined independently by each FE-PGA. This will be done by resetting a clock-incremented

register with the bunch crossing reset synchronous command of the TFC (see Sect. 3.2.2). The bunch crossing identification number would also allow the tagging of the sub-channel used in the ASIC based analogue electronics for calibration purpose.

Control FPGA and slow control on the board The Ctrl-PGA is in charge of the tasks which are common to the channels of the FEB. It ensures that the four FE-PGAs run synchronously, provides the crate and FEB identification numbers to the links and distributes the slow control signals to the different components of the board. This is particularly important as we plan to use the SPI protocol which relies on selection lines (slave selection). The selection line may be activated by the Ctrl-PGA after it has been properly configured in order to address any chip of the board.

The slow control on the FEB can be driven by a GBT-SCA chip (a component of the GBT project devoted to the slow control [76]) which receives its e-links from the backplane and is the only interface with the rest of the system. The protocols that may be used are I^2C, SPI, parallel and JTAG. We plan to implement on our boards the possibility to reprogram the FPGA from the GBT link and JTAG is the protocol that would be used for this purpose.

Optical output The optical output is performed through five GBT components and Versatile Link transmitters [76] from CERN: four for the data path and an extra link for the LLT path. The links are mono-directional. The clock needed by the GBT will be received from the backplane and the control board (see Sect. 3.2.2), which will be equipped with another GBT component.

Front-End prototype A first prototype of the FEB has been designed and used to assess the capabilities of the candidate FPGA (A3PE from MICROSEMI) for our design and also to acquire the data from the analogue electronics in a test beam,*i.e.* close to realistic conditions. We also foresee to check the radiation tolerance of some components by exposing the prototype in a particle beam. However, most of the components we plan to use should be able to sustain the moderate radiation level at the position of the calorimeter electronics (which is expected to reach ~ 5 krad for 50 fb^{-1}) or have been already tested in harsher conditions.

The prototype includes several regulators for powering and delay chips in order to perform all the necessary time adjustments. The acquisition is performed through a USB interface. Two FPGAs are located on the PCB: an A3PE (flash technology) and an AX (anti-fuse) FPGA, both from MICROSEMI/ACTEL. The former is our preferred candidate, the latter being a backup solution. The AX FPGA is not soldered on the PCB but pressed firmly under a metallic piece and on a golden foam making the contact between the balls of the FPGA and the PCB (see Fig. 3.5). This system permits the AX FPGA to be changed without having to unsolder it.

For the upgrade, the bit flipping rate at the FPGA output is large and the GBT requires the clock frequency of the I/Os to be 80 MHz. It was therefore vital to demonstrate that the A3PE can cope with such a rate. This test was important since for the ProASIC FPGA family used in our present boards (an ACTEL predecessor of the A3PE family) some problems had been observed in such tests. Hence, the two FPGA were programmed to exchange a large quantity of data at 80 MHz on many I/Os. No data corruption was observed indicating that the A3PE should satisfy the requirements for our electronics.

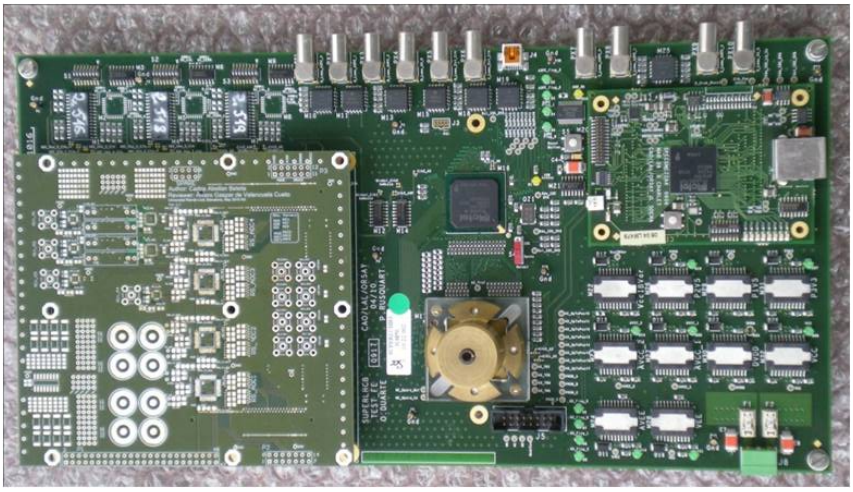

Figure 3.5: Picture of the prototype of the Front-End board. The analogue mezzanine is visible on the left. The two FPGAs (models A3PE and AX from MICROSEMI/ACTEL, see the text) are in the central part of the board, in black and under the copper socket.

(iii) Low Level Trigger

The Low Level Trigger (LLT) is a hardware trigger designed to select interesting events at high efficiency, and to reject very busy events at an early stage, in order to reduce the input rate to the High Level Trigger (HLT) software trigger, during the commissioning phase of the LHCb upgrade running, or in the early period of the data taking, if not enough CPUs are available in the PC trigger farm. It will reduce the 40 MHz LHC bunch crossing frequency to a frequency of about 1–40 MHz.

The calorimeter is one of the systems that provides information for the LLT. Since the current Level-0 trigger architecture is already capable of delivering information at 40 MHz for a hardware trigger, the majority of its features will be kept for the LLT, and will only be adapted to the new architecture of the upgrade.

The goal of the calorimeter part of the LLT is to build ECAL and HCAL clusters of 2×2 cells and to select the ones with the highest transverse energy (E_{T}). The first step of the LLT computation is to obtain for each cell a roughly calibrated transverse energy value, coded in 8 bits. This is realized in the FE-PGA of the Front-End boards, dividing the 12 bit measured ADC values by a calibration constant. This processing is identical for the ECAL and the HCAL.

The obtained transverse energy values are then summed to compute the transverse energy of 2×2 clusters, and these are compared to select the cluster with the highest value. This step is performed in the Trig-PGA of the Front-End boards. Each Trig-PGA handles the 32 channels of the FEB but also needs to access the values of the energies of the neighbouring cells in order to compute the transverse energies of the clusters located at the borders of the 4×8 area covered by the board. The exchange of data between boards is performed via the backplane for the horizontal neighbours, and via ethernet cables plugged on the backplane for the vertical neighbours. The backplane connections and the cables exist already in the current detector and will be kept and re-used during the upgrade phase. Since the scintillating pad detector (SPD) will be removed from the detector, the SPD hit multiplicity will no longer be available

for rejecting busy events at an early stage. Multiplicities computed with the ECAL and HCAL will be used instead, namely the numbers of cells with a transverse energy larger than a given threshold. These multiplicities will be also computed in the Trig-PGA. The processing will be identical in the HCAL and the ECAL.

The result of the LLT computation (highest energy cluster and multiplicity) will be sent from each FEB to the electronics barrack for further processing, via a dedicated optical fibre. These data will be received by four TRIG40 boards whose task is the final selection of the ECAL and HCAL clusters, comparing all the inputs and selecting the cluster with the highest transverse energy over the ECAL or HCAL. These boards will also compute the total ECAL and HCAL multiplicities. These four quantities, the two candidates of highest energy and two multiplicities, will then be input to the final trigger decision.

3.2.2 Control board

The control board will be located in the central slot of the front-end crate. It distributes some critical signals to the boards of the crate: the clock, the slow control signals and the fast and synchronous commands. It will be equipped with one GBT chip and one bi-directional link.

The e-link outputs of the GBT use the SLVS JEDEC standard. We do not plan to propagate directly those signals on the backplane. Hence, the signals from the GBT will first be converted to LVDS before being routed. The FPGA of the control board will be of type A3PE from MICROSEMI, the same type as used for the FEB.

Timing and Fast Control system handling The GBT chip of the control board receives the clock from the LHCb Timing and Fast Control system (TFC) and its optical link and propagates it to the other boards of the crate after SLVS to LVDS conversion. The clock phase adjustment capabilities of the GBT can be used at this level to tune the phase of the front-end signal processing, after configuration by the slow control.

The TFC system also distributes the LLT signal and synchronous commands. The front-end electronics do not require the LLT decision. On the contrary, the electronics provides some information on the energy deposits in the calorimeter to the counting room where the decision is taken. The front-end electronics requires only a sub-sample of the TFC commands defined for LHCb. The TFC system for the upgrade will propagate 44 bits through the GBT at 40 MHz [80]. Most of those bits or commands are used downstream of the front-end electronics. Only eight commands are related to the front-end. This reduced number (without any loss of the electronics capabilities) permits the backplane of the current electronics to be re-used and to propagate through it reset, test and calibration signals.

Slow control As for the fast commands and the clock, the slow control of the upgraded electronics is driven by the bi-directional optical links of the control board. Seventeen e-links are necessary in a crate: 16 for the FEB and an extra link for the board itself. Here also, we plan to convert the slow control e-links from SLVS to LVDS type before propagation to the backplane.

We intend to keep the present backplane for the upgrade [81]. This decision has an impact on the design. The clock, fast commands and power lines will be re-used. The difficulty concerns the slow control where the bus connecting all the FEB to the control board cannot be re-used for the e-links connecting the GBT chip of the control board with the GBT-SCA of the FEB.

However, at the upgrade the LVDS data lines of the backplane become spare lines. They are not necessary any more as there is no longer any data exchange between the FEB and the control board, since each FEB sends its own data through its own optical links. Each data line used at present is made of three differential LVDS pairs and this will be sufficient to operate the slow control on the crate for the future electronics.

3.2.3 High-voltage, monitoring and calibration systems

The high-voltage, monitoring and calibration systems of the ECAL and HCAL are essentially slow control based, and therefore are independent of data taking and can be used for the upgrade without major changes.

The following systems, however, communicate with the current LHCb Detector Control System (DCS) through the slow control SPECS protocol. Since the SPECS will not be available any more for the upgraded electronics, these systems need to be adapted in order to be compatible with the GBT transmissions.

- The HV-LED boards, which control PMT high voltages and LED flash intensities.
- The integrator readout boards (INTEG), which are used to readout the HCAL PMT anode current.
- The LEDTSB boards, which send firing pulses to the LED drivers with the proper sequence.

The HCAL calibration system is based on a capsule traversing the modules of the calorimeter and containing a ^{137}Cs radioactive source. The source motion control communicates with the DCS computers via a CANbus protocol. As CANbus will be available for the upgrade, this system will remain unchanged.

The high-voltage, monitoring and calibration systems include four other types of boards which do not communicate directly with DCS and can remain unchanged:

- The Cockcroft-Walton HV generator boards (CW bases), on which the PMTs are mounted. These boards are electrically very similar for ECAL and HCAL, and differ only mechanically.
- The HCAL integrator boards, which are used to measure the anode DC current of PMTs. One board serves eight PMTs.
- The LED driver boards that produce LED light flashes for ECAL and HCAL calibration and monitoring.
- The PIN-diode modules, including PIN photo-diodes and preamplifiers. They are used to monitor the LED flash amplitude.

Among the seven boards described, only the LEDTSB boards are installed into the readout crates together with the Front-End and control boards. They receive the synchronous calibration commands from the backplane and also use its power lines. The HV-LED and INTEG boards are installed standalone, on the HCAL or ECAL chariots or on the calorimeter platform, and use dedicated MARATON power supplies.The number of boards of each type currently used for ECAL and HCAL are given in Table 3.2.

Table 3.2: Number of control and passive boards for the high-voltage, monitoring and control systems of the ECAL and HCAL. Only the HV-LED, INTEG and LEDTSB boards need to be interfaced with the GBT slow control.

	HV-LED	INTEG	LEDTSB	PMT/CW	INT FE	LED drv	PIN amp
ECAL	34	-	8	6016	-	456	124
HCAL	8	4	2	1488	188	104	104

Each HV-LED, INTEG and LEDTSB board is equipped at present with a SPECS slave mezzanine board [82]. SPECS is designed to drive JTAG, I^2C and parallel buses and the mezzanines have also an ADC on board, which is used extensively to measure various DC voltage levels. All these features are also present in the GBT-SCA component from CERN that will be used for the upgraded slow control. Hence, the natural solution is to develop a GBT-SCA mezzanine with the same pinout and functionality as the present SPECS one. A total of 56 GBT-SCA mezzanines will be necessary to equip both the ECAL and HCAL (see Table 3.2).

As the GBT-SCA chip power supply voltages differ from those used by SPECS (1.2 V core, 2.5 V IO), the GBT-SCA mezzanine will have power regulators on board, either linear or switching DC-DC converters. Moreover, level adapters will be necessary to connect the GBT-SCA to the 3.3V logic of the mother boards.

The LEDTSB boards will use the infrastructure of the FEB crates where they are installed. In the case of the standalone HV-LED and INTEG boards, some intermediate fanout boards based on the GBT are foreseen to ensure communication through a single bi-directional link to several boards. The number of such fanout boards is determined by the e-link maximum length and by the maximum number of GBT-SCAs which can be served by one GBT. For example, if the maximum e-link cable length is 2 m and the maximum number of GBT-SCAs per GBT is 16, then it will be necessary to have 8 GBT fanout boards, considering the present number of HV-LED and INTEG boards to serve and their positions.

3.2.4 Connections to the readout boards

Here we detail the foreseen optical connections between the front-end electronics and the readout boards. Those connections serve the data acquisition, the LLT path and the slow control. The system described here is based on the ATCA (TELL40, SOL40 and TRIG40) technology with four AMC40 mezzanines [15] per board.

Table 3.3 lists the connections between the FEB used either to acquire the PMT signals (physics) or to acquire the pin-diodes (calibration) and the TELL40 boards. The connections have been optimized in order to reduce the number of links while keeping the system simple.

One GBT link per FEB is used to send the results of the Trig-PGA to the LLT-Calo acquisition in the barracks. The connections are listed in Table 3.4.

In addition there must be bi-directional fibres to the control boards in each crate. The two sides of the calorimeter have nine crates each, seven for the ECAL and two for the HCAL. The link being bi-directional and 18 links being necessary per side, two AMC40 mezzanines are needed per side. Apart from the control board, optical links are needed for the high-voltage, monitoring and calibration system. The fanout board described in Sect. 3.2.3, permits the reduction of the number of AMC40 mezzanines to a maximum of two boards. Table 3.5 gives a summary of the

Table 3.3: Connections needed for the calorimeter data.

Detector part	FEB	TELL40
ECAL A	96 (incl. pin-diodes)	4 (full load)
ECAL C	96 (incl. pin-diodes)	4 (full load)
HCAL Inner part	2×16 (incl. 2 pin-diodes/side)	2
HCAL Outer part	2×11	1

Table 3.4: Optical link connections needed for the LLT data.

Detector part	FEB	links	AMC40	TELL40
ECAL + HCAL A	119	119	6	2
ECAL + HCAL C	119	119	6	2

connections for the slow control.

Table 3.5: Connections needed for the slow control of the calorimeter upgrade.

System	AMC40	TELL40
Ctrl-boards	2 AMC40 (22 links) /side	1 ATCA
Cockcroft-Walton/Integrators	2 AMC40	1 ATCA

3.3 Radiation effects and module replacement

3.3.1 Radiation effects and ageing

The radiation tolerance of most of the elements of the LHCb calorimeter system have been studied in dedicated irradiation measurements. In addition, complementary results have been obtained from the 2010-2012 LHC run. The expected dose calculations from Ref. [66] (which are broadly consistent with passive dosimeter measurements performed in 2012) have been used for the lifetime estimates. The dose accumulated in the innermost ECAL cells for 2 fb^{-1} is $\sim$100 krad at the front and rear planes, and reaches 250 krad inside the ECAL at the position of the electromagnetic shower maximum.

The following elements will suffer radiation damage:

- ECAL: modules (scintillators and WLS fibres), light readout elements (light guides and PMT entrance window), PMT Cockcroft-Walton (CW) bases.
- HCAL: here only the modules should be affected, since the PMTs are located behind the HCAL, and hence are screened by the iron.

The PMTs, their CW boards and the light guides can be easily replaced. This can be done during LHC winter shut-downs. The central modules of ECAL, in principle, can also be replaced,

although this is a difficult procedure that can be performed only during long LHC shut-downs, as described below in Sect. 3.3.2. The HCAL modules are not replaceable.

Several tests of the radiation tolerance of the ECAL modules have been conducted. The tests were performed in different conditions, however all results are broadly consistent. The first test performed in 1998 with an ECAL module prototype at an electron beam facility is described in detail in [66]. It was shown that the module performance will remain satisfactory until 2.5 Mrad is accumulated at the position of the shower maximum (equivalent to 20 fb^{-1}).

More recently, two studies have been performed making use of spare ECAL modules.

Irradiation with 24 GeV protons An outer type module was exposed to radiation at the CERN PS IRRAD facility [1]. The fibre density in the inner modules is higher than in the outer ones (144 and 64 per module respectively), so the results obtained should be considered as a pessimistic limit when used to extract radiation tolerance estimations for the inner region. The outer module was irradiated with 24 GeV protons to ~ 2 Mrad in 2010 and again to the same value in 2012 (total of 4 Mrad) and measured several months after each irradiation.

Two types of measurements were performed: a longitudinal scan with a ^{137}Cs source with a measurement of the PMT DC current, and a test at the CERN SPS with an electron beam. A non-irradiated module of the same type was used as a comparison for each measurement (before the first irradiation, the two modules were calibrated at SPS and shown to have equal performances). The tests at the electron beam were performed with a single module, the beam pointing at its centre. The light yield and energy resolution were determined. Considering the module transverse dimensions (12×12 cm^2), the energy resolution measurements are affected by the lateral leakage of the electromagnetic shower and are only indicative.

Table 3.6: Results of the tests of irradiated and non-irradiated ECAL outer modules at the SPS electron beam. The light yield is given in terms of photon-electrons per GeV and the resolution is in percent.

E_{beam}	No irradiation		2 Mrad		4 Mrad	
(GeV)	Light yield	Resolution	Light yield	Resolution	Light yield	Resolution
50	2598 ± 52	1.37 ± 0.04	583 ± 12	2.16 ± 0.04	223 ± 10	2.74 ± 0.04
100	2611 ± 52	1.01 ± 0.03	576 ± 12	1.57 ± 0.03	221 ± 10	2.26 ± 0.05
120	2604 ± 52	0.98 ± 0.03	571 ± 12	1.36 ± 0.03	/	/
125	/	/	/	/	220 ± 10	2.06 ± 0.05
150	/	/	/	/	219 ± 10	1.77 ± 0.05

The results of the SPS tests are shown in Table 3.6. After the first irradiation (2 Mrad, or 16 fb^{-1} for the ECAL shower maximum position), the light yield was found to be lower by a factor $\sim$4.5, with a moderate degradation of the energy resolution. After the second irradiation (total of 4 Mrad or 32 fb^{-1}), the light yield was reduced by a factor $\sim$12 and the degradation of the energy resolution was significant. The results of the ^{137}Cs source scan on the light yield degradation, seen in Fig. 3.6 (a) confirm the numbers obtained with electrons.

[1] We express our gratitude to Maurice Glaser (CERN) for his great help in module irradiation.

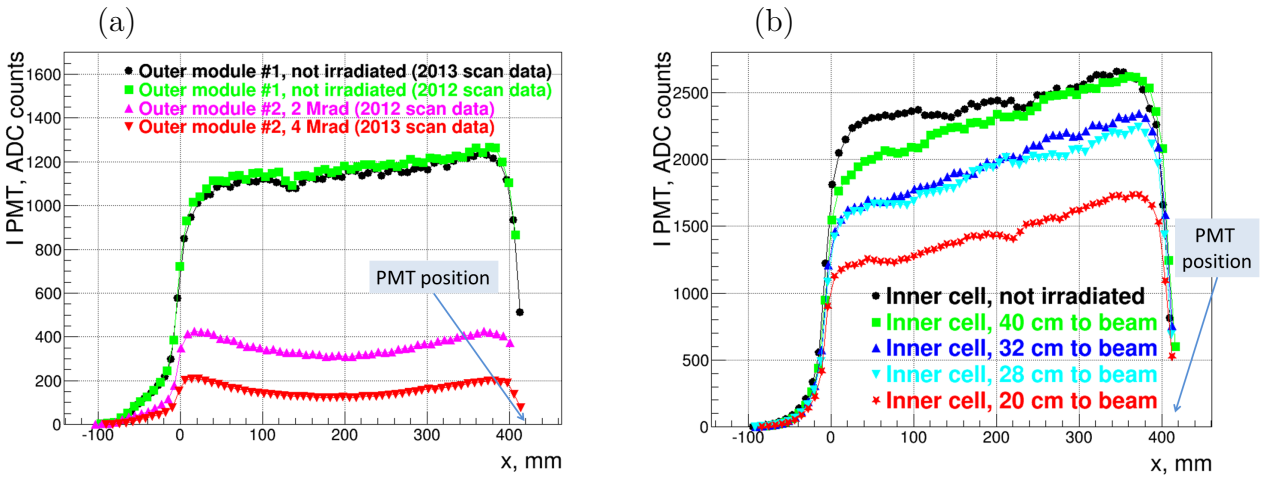

Figure 3.6: Results of irradiated and non-irradiated ECAL modules scan with ^{137}Cs source: (a) outer modules, irradiated with 24 GeV protons; (b) inner modules, irradiated in the LHC tunnel.

Irradiation in the LHC tunnel Another radiation tolerance test was performed with two inner type ECAL modules irradiated in the LHC tunnel, next to the accelerator beam pipe and close to the LHCb cavern, ∼4 m away from the *pp* interaction point. This test is of particular importance as the module type studied is identical to those in the region of interest (inner type module), as is the composition of the radiation. The inner ECAL modules are subdivided into 9 cells of 4×4 cm^2 transverse size. By the end of 2012, the dose accumulated by the cell closest to the accelerator beam pipe was ∼1 Mrad. These modules have been scanned with the ^{137}Cs source, the results being shown in Fig. 3.6 (b). A moderate (40-50%) loss of light yield in the most irradiated cell is observed. The irradiation will be resumed when LHC starts operation again after the long shut-down LS1.

Both measurements, with the IRRAD facility and in the LHC tunnel, indicate that the performances of the central ECAL modules are expected to remain satisfactory until 20–30 fb^{-1}. Replacement of the central modules can hence be postponed until the LHC long shut-down LS3, thereby reducing the number of operations that need to be accomplished during LS2.

The radiation tolerance of the Cockcroft-Walton bases was studied with the 50 GeV proton beam of the U70 accelerator at IHEP (Protvino)[2]. The high-voltage produced by the bases was continuously monitored during the irradiation. They remained operational until 1.5–2 Mrad, corresponding to 30–40 fb^{-1} of integrated luminosity for the ECAL central cells, was accumulated. The CW boards may easily be replaced during shut-downs when necessary, according to the accumulated dose and the degradation in performance. A total of ∼500 boards may have to be replaced over the ten year duration of upgrade operation.

During the same radiation tolerance test, the degradation of the transparency of the PMT entrance window was studied. After 2 Mrad, corresponding to 40 fb^{-1} for the ECAL centre, a minor transmittance loss was observed, which amounts to 5% at 467 nm (WLS fibre KURARAY

[2]Performed during the irradiation run of the ATLAS LAr calorimeter. Many thanks to our ATLAS colleagues.

Y11 emission peak). The radiation damage of the light guides, which are polystyrene blocks of dimensions $30 \times 11 \times 11\text{mm}^3$, was not directly studied, but is expected to be of a few percent.

The radiation damage of the HCAL modules has been studied during the LHC run of 2011-2012 using the ^{137}Cs calibration data. The LHCb HCAL is an iron-scintillator sampling calorimeter arranged parallel to the collider beam direction. It has 6 tile rows (#0-5) along the beam direction. For the central HCAL cells, the relative light yield for each tile row was determined with respect to the rearmost row (#5), which receives the least dose and is not expected to be damaged by radiation.

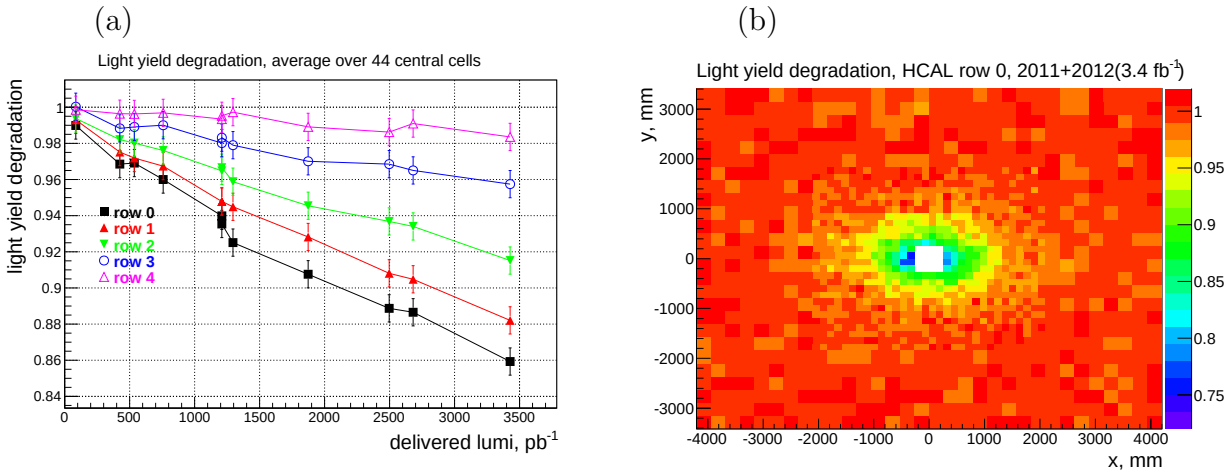

Figure 3.7: Light yield degradation in HCAL during first three years of operation, integrated to 3.4 fb^{-1}: (a) each row, averaged over HCAL central cells, as a function of delivered luminosity; (b) row #0, after 3.4 fb^{-1}.

The results are shown in Fig. 3.7. A sizeable degradation is observed at 3.4 fb^{-1}. Hence, the HCAL central cells are not expected to remain operational for the full life span of the upgrade. However, the LLT, to which the HCAL contributes, will only be used during the early years of upgrade operation. Hence, the eventual loss of the HCAL central cells will not impact upon the physics performance of the experiment.

3.3.2 ECAL module replacement

As discussed, the calorimeter modules are expected to suffer from radiation damage as the integrated luminosity received by the LHCb detector increases. The radiation level is maximum close to the beam pipe, more precisely in the horizontal plane where the magnet sweeps a large number of low momentum particles. According to the foreseen integrated luminosity, the most exposed modules will be replaced during the LS3 shut-down: 32 fully equipped modules are available for this purpose, corresponding to 288 channels.

The ECAL is a wall of modules of square cross-section, each following the classical "shashlik" design of sandwiched scintillator layers and lead absorber plates, pierced by a set of wavelength shifting fibres. The surface covered by one module is 121.2×121.2 mm^2. In the electromagnetic

calorimeter inner section, nine square cells of 40.4 cm in size are contained in a module. The longitudinal size of the sub-detector is equivalent to 25 X_0. Its Pb:Scintillator volume ratio is 2:4 with 132 layers of alternating absorber and scintillator, with a weight of 30 kg per module. Figure 3.8 shows the area corresponding to the 32 modules to be replaced.

The modules on either side of the ECAL are gathered together in two horizontal rows surrounded by a 250 μm thick stainless steel band attached to the side frame and stretched to ensure a precise positioning with 1 mm tolerance. The innermost four columns of each side, above and below the beam-plug, are grouped together in two-columns, a steel band being wrapped around them, and are supported from the top. This design was chosen to ease the foreseen replacement of the central cells. A 1.4 tonne plate at the top of the frame (in red in Fig. 3.8) ensures the uniform distribution of the load onto the modules, except for the four most inner columns where individual plates have been installed. The modules to be exchanged belong to these four columns. In the centre of the module wall a beam-plug of 500 kg protects the modules from a region of very high radiation. Each platform half can slide out perpendicular to the beam axis and gives access to the ECAL wall. In order to execute the module replacement, the following sequences of operations is required:

- Dismount the individual plates located at the top of each inner column. This necessitates disconnecting and removing the LED box system located at the top to easily access the modules. Special tools will be designed in order to ensure a safe dismounting procedure.
- Remove the modules and store them until the region to be exchanged is reached. During this operation the steel band pressure is relaxed and dedicated tools will ensure column stability.
- Remove the beam-plug. The crane will be used for this operation and a specific tool will be prepared.
- Exchange the modules and stack the columns again. A template will ensure the positioning of individual modules.

The un-stacking and re-stacking of the 120 modules can be achieved within three months. Particular attention has to taken to ensure a final positioning of the structure with a 1 mm precision.

3.4 Performance

3.4.1 Effect of pile-up

The rate of multiple interactions per crossing will increase significantly at the higher instantaneous luminosities foreseen for the upgrade. This will lead to a degradation of the energy and position measurements for the calorimetric objects as other particles can contribute to the shower of the object to be measured. In the following discussion 'pile-up' refers to this overlap of showers in the calorimeters.

In order to reduce the resolution degradation due to the pile-up, the size of the clusters used to reconstruct the neutral particles may be reduced with respect to those formed at present.

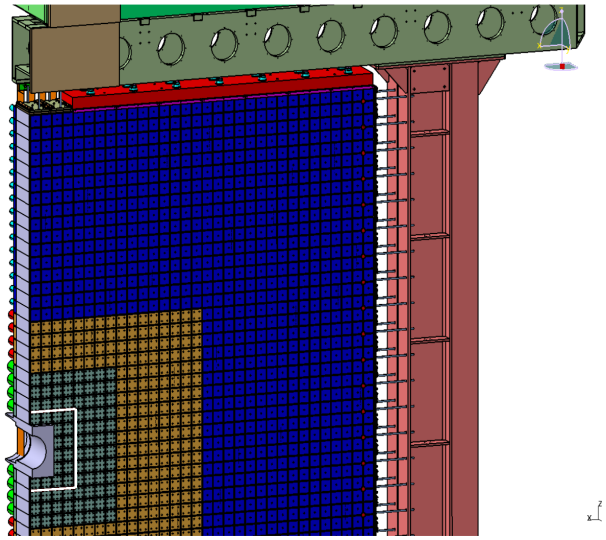

Figure 3.8: The white line delimits the region on one half of the ECAL where the modules will need to be replaced.

Two new shapes of smaller clusters have been analysed, to investigate whether they mitigate the effects of pile-up without degrading the overall resolution.

To estimate the photon energy resolution, three simulation samples of the decay $B_s^0 \to \phi\gamma$ are used. This decay provides a wide spectrum of photon energy. These samples correspond to three instantaneous luminosity conditions, $\mathcal{L} = 1 \times 10^{33}$, 2×10^{33} and 3×10^{33} cm^{-2}s^{-1} and therefore to three pile-up conditions, $\nu = 3.8$, $\nu = 7.6$ and $\nu = 11.4$, respectively, where ν is the average number of pp interaction per bunch crossing. The intermediate sample corresponds to the maximum expected instantaneous luminosity for the upgrade period and the third sample provides extreme conditions in order to investigate the limits of the reconstruction.

From these samples the energy resolution defined by $(E_{\text{true}} - E_{\text{rec}})/E_{\text{true}}$ is determined, where E_{true} is the true photon energy, and E_{rec} is the reconstructed photon energy, for a given cluster. The resolution is computed for each cluster shape and for several photon categories. The categories are related to the three regions of the ECAL (inner, middle and outer zones) and the number of primary vertices (PV) in the event.

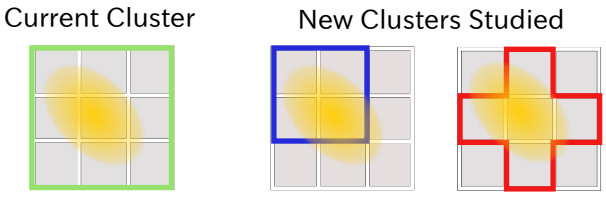

Figure 3.9: Shapes of the three types of clusters considered.

At present, the ECAL clusters have a square shape with 3×3 cells whatever the region being

analysed [67]. Two new shapes are studied as shown in Fig. 3.9:

- 2×2 clusters: out of the nine cells of the 3×3 cluster, only the 2×2 zone made by the four most energetic cells is retained.
- Cross clusters: out of the nine cells of the 3×3 cluster, the four corner cells are removed giving a cross shape to the final cluster.

Intuitively, the pile-up should be reduced by a factor 4/9 and 5/9 for the 2×2 and cross shapes respectively with respect to the standard one. Three types of reconstructed energies are now defined corresponding to the three types of clusters.

Only photon candidates with a transverse momentum $p_{\mathrm{T}} > 250$ MeV/c, originating from the interaction region ($\Delta r < 10$ mm and $\Delta z < 150$ mm) and successfully associated to a true simulated photon are considered in this study. Only non-converted photons are analysed.

As can be seen in Fig. 3.10 the photon energy resolution distributions obtained do not have a Gaussian shape. A tail is present on the left side of the distributions due to the reconstructed energy being larger than the true energy. This tail is a consequence of pile-up effects. The right part of the distribution (reconstructed energy lower than the true photon energy according to the simulation) does however possess a Gaussian profile. To quantify the pile-up effect, these distributions are fitted. The model used is a Crystal Ball [83] function defined by

$$f(x;\alpha,n,\mu,\sigma) = N \cdot \begin{cases} \exp(-\frac{(x-\mu)^2}{2\sigma^2}), & \text{for } \frac{x-\mu}{\sigma} > -\alpha \\ A \cdot (B - \frac{x-\mu}{\sigma})^{-n}, & \text{for } \frac{x-\mu}{\sigma} \leqslant -\alpha \end{cases} .$$

Out of the four parameters of this function, only α and n are related to the left tail and the pile-up effect. The parameters σ and μ are related at first order to the resolution observed on the right tail of the distribution and to the position of the maximum of the resolution distribution, respectively. A positive μ indicates an average energy loss in the reconstruction. The parameter α defines the start and the size of the tail: a smaller α is related to a larger tail. Hence, α is strongly related to the degree of pile-up and a reconstruction that maximizes α reduces the effect of pile-up. The parameter n tunes the amplitude of the tail but has less effect than α in the following.

The energy resolution is measured for the three reconstructions and fitted using the model described above. For all the regions of the detector, energy ranges and number of PVs, the 2×2 and cross shape clusters give larger α values than the 3×3 type. Moreover, cross clusters seem to give slightly better results than the 2×2 types. A plot showing some of the results from this study is given in Fig. 3.11. The fit results are confirmed qualitatively by comparing the distributions of Fig. 3.10.

Smaller clusters reduce the pile-up effect, but they potentially lead to a higher energy leakage and may degrade the resolution, especially in the inner region whose cells are 4×4 cm^2 in size to be compared to the 3.5 cm Moliere radius. The larger the energy leakage, the larger the μ parameter as can be seen from the uncorrected results plotted in Fig. 3.12 (a). This bias is expected to affect essentially the inner region and can be corrected for. A simple correction factor β is evaluated in order to recover the proper energy scale, so that $E_{\mathrm{rec}}^{\mathrm{corr}} = (1+\beta)E_{\mathrm{rec}}$ and $\langle (E_{\mathrm{true}} - E_{\mathrm{rec}}^{\mathrm{corr}})/E_{\mathrm{true}} \rangle \sim 0$. Therefore, $\beta \sim \mu/(1-\mu)$ is computed for each energy bin, in each region but is averaged over the number of PVs. As can be seen in Fig. 3.12 (a), the energy bias

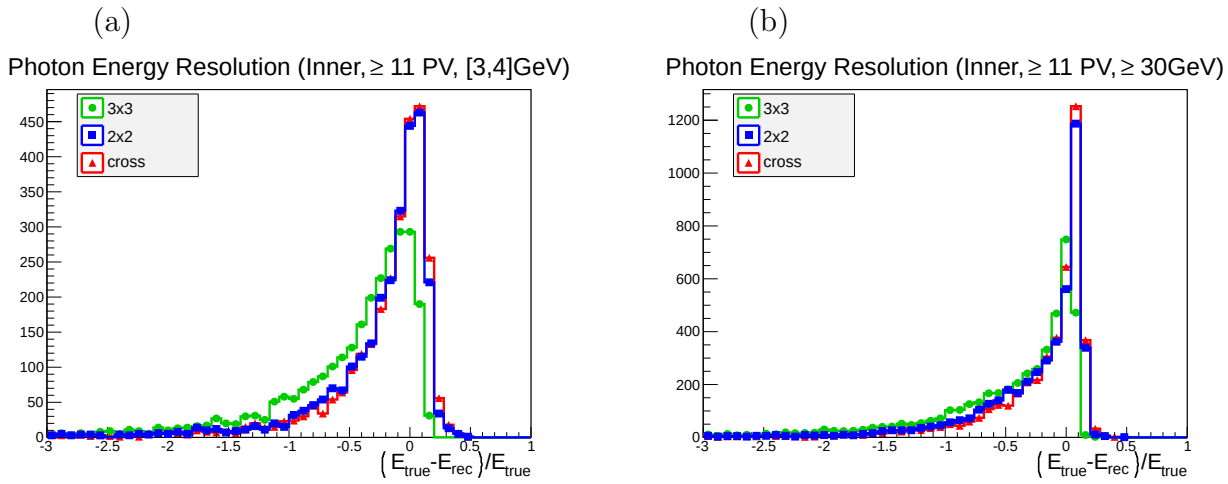

Figure 3.10: Energy resolution in the ECAL inner area, for events with at least 11 PVs, in two energy range $[3; 4]$ GeV (a) and ≥ 30 GeV (b) and for the 3×3 (green), the 2×2 (blue) and the cross shape clusters (red). The pile-effect is clearly visible, especially at low energy.

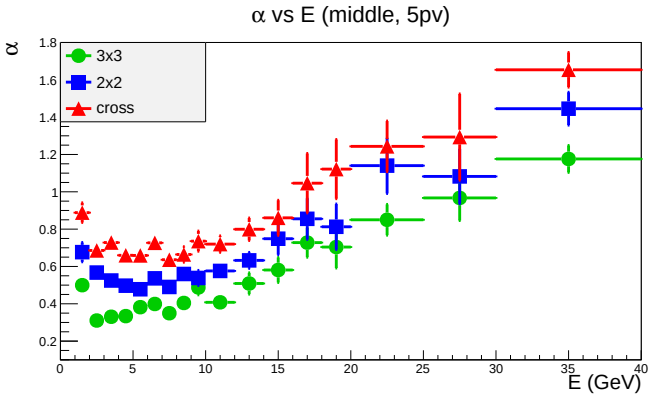

Figure 3.11: Evolution of the parameters α with the energy, in the middle region and for the events with 5 PVs.

is essentially eliminated by this rough correction, however the tail parameters α and n are not changed and so the impact on the resolution is not significant, as is evident from Fig. 3.12 (b), especially in the case of the 2×2 square clusters.

In conclusion, energy reconstruction with 2×2 and cross clusters mitigate to a large degree the effect of the pile-up with respect to the present reconstruction, without significantly degrading the energy resolution. Therefore, one of these methods could be adopted for the upgrade. A study is on-going to evaluate the benefit of using this new strategy already with the current detector after the long shut-down of 2013–2014.

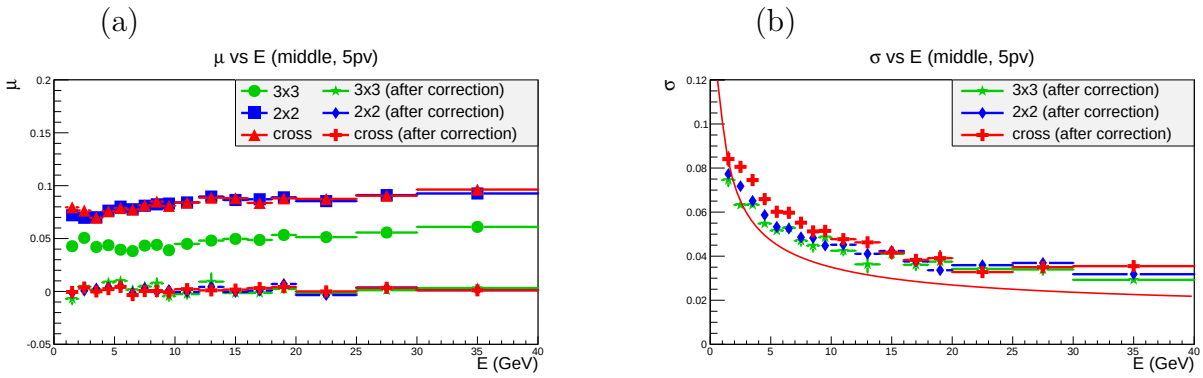

Figure 3.12: (a) Evolution of the parameter μ with the energy (before and after β correction), in the middle region and for the events with 5 PVs. (b) Calorimeter resolution obtained from the parameter σ after applying the β correction on the energy, in the middle area and for the events with 5 PVs. The red curve on the σ plot is an approximated estimation of the calorimeter intrinsic resolution, $\sigma(E) = \frac{10\%}{\sqrt{E}} \oplus 1.5\%$.

3.4.2 Particle identification

(i) Photon identification

Although the energy resolution and the calibration of the calorimeter system should be easier after removal of the SPD and PS, the particle identification will be affected. Here we present results on this topic. Note that the studies presented here use the conventional 3×3 clustering algorithm.

The identification of photons in LHCb is performed in essentially three steps [67]. First, the cells of the ECAL that received a significant amount of energy are gathered to build clusters. Only 3×3 clusters and photons with a transverse momentum $p_{\mathrm{T}} \geq 200$ MeV/c are considered. Then, the clusters which are close to the extrapolation of a track to the calorimeter are removed from the list of "neutral" clusters. The distance between the cluster and the extrapolation of the closest track is quantified by a two-dimensional chi-squared, χ^2_{2D}, that takes into account the uncertainties both on the cluster position measurement and on the track extrapolation. Finally, the photons candidates are selected from the list of neutral clusters by using several criteria: the energy deposited in the preshower, the shape of the ECAL shower, the already defined quantity χ^2_{2D}, the energy in the HCAL corresponding cells, etc. A multivariate method is used to obtain an estimator on the probability that a neutral cluster is associated to a photon.

In the following four simulation samples of the decay channel $B^0_s \to \phi\gamma$ have been used. The first sample corresponds to the current data taking conditions ($\nu = 2.0$) and the current detector geometry. This sample will be referred as "standard" as this corresponds to the current configuration of the detector. The three others are based on a plausible upgraded LHCb (pixel VELO, current upstream tracker, fibre tracker covering the whole T-stations and no SPD/PS), the foreseen upgrade energy ($E_{\mathrm{beam}} = 7$ TeV) and high luminosity conditions ($\mathcal{L} = 1 \times 10^{33}$, 2×10^{33} and 3×10^{33} cm^{-2}s^{-1}, corresponding to values of ν of 3.8, 7.6 and 11.4 respectively). The instantaneous luminosity of the last sample is beyond the maximum foreseen for the upgrade

and permits the margins of the performances of the system to be determined.

Selection of the neutral clusters The neutral clusters are selected with the requirement $\chi^2_{\rm 2D} \geq 4$. Simulation truth information is used to search for any association between these clusters and true prompt photons, defined by a cylinder $\Delta r \leq 1$ cm and $\Delta z \leq 15$ cm around the nominal interaction point.

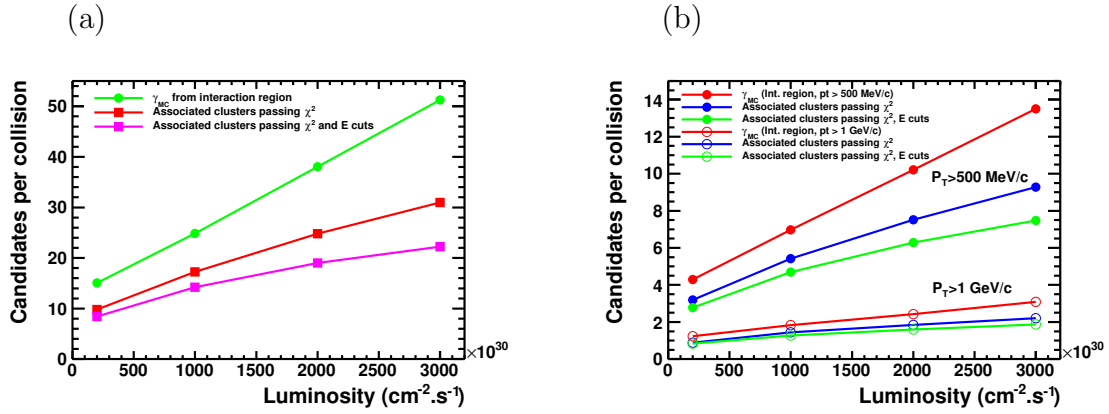

Figure 3.13: The number of true photon candidates per collision in the Monte Carlo, and the number of associated neutral clusters after the $\chi^2_{\rm 2D}$, and the $\chi^2_{\rm 2D}$ and energy requirement cuts, plotted for different values of instantaneous luminosity. (a) is for photons with $p_{\rm T} \geq 200$ MeV/c; (b) is for photons with $p_{\rm T} \geq 500$ MeV/c and $p_{\rm T} \geq 1$ GeV/c.

Figure 3.13 (a) shows the number of true photons per collision and the number of associated neutral clusters seen in the calorimeter system as a function of the instantaneous luminosity, for photons with $p_{\rm T} \geq 200$ MeV/c . A fraction of photons are never associated to any cluster and this component is mainly due to early conversions. Results are then shown for the number of neutral clusters for which the reconstructed energy corresponds to within 50% of the generated value. The curves indicate a slow degradation of the fraction of photons selected, but this degradation is nevertheless limited up to $\mathcal{L} = 2 \times 10^{33}$ cm^{-2}s^{-1} and evolves slowly up to $\mathcal{L} = 3 \times 10^{33}$ cm^{-2}s^{-1}, without any non-linear increase. Most of the photons that contribute to Fig. 3.13 (a) are low $p_{\rm T}$ photons, typically ~ 300 MeV/c, that are most vulnerable to pile-up effects and whose energy is more difficult to measure. The physics analyses usually select higher $p_{\rm T}$ clusters. Figure 3.13 (b) shows the same information after selecting photons with $p_{\rm T} \geq 500$ MeV/c and $p_{\rm T} \geq 1$ GeV/c. The efficiency degradation is here reduced compared to the case when a looser $p_{\rm T}$ cut is applied, as can be seen by considering the ratio of the curves for associated clusters to all clusters, and comparing this ratio to that which would be obtained from Fig. 3.13 (a). Hence, the increase in particle multiplicity due to the large number of collisions per beam crossing does not impact aversely upon the photon finding efficiency, particularly at higher $p_{\rm T}$. Moreover, a fraction of the candidates with badly measured energy is polluted by the pile-up which affects essentially low $p_{\rm T}$ photons. It is expected that adopting the alternative cluster definitions discussed in Sect. 3.4.1, should help recover efficiency.

The contamination in the photon sample at the reconstruction stage can be assessed from

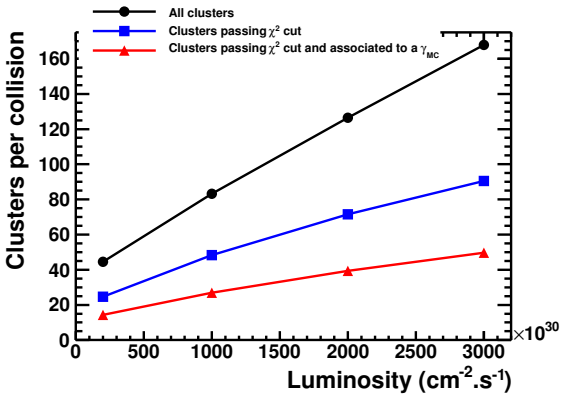

Figure 3.14: Number of clusters reconstructed in the calorimeter as a function of the luminosity. Clusters identified as neutral clusters ($\chi^2_{\text{2D}} \geq 4$) are shown before and after the χ^2_{2D} cut, together with those neutral clusters associated to a simulated photon.

considering the total number of clusters seen in the detector, and seeing what fraction of these are associated to true generated photons. These results are shown in Fig. 3.14 as a function of the luminosity, for the case where the clusters satisfy $p_{\text{T}} \geq 200$ MeV/c. The contamination, typically $\sim 40\%$ with the χ^2_{2D} requirement, does not worsen with luminosity increase and the performance of the detector is acceptable up to $\mathcal{L} = 3 \times 10^{33}$ cm^{-2}s^{-1}. The contamination is reduced further when applying more severe criteria on the candidate p_{T}.

Photon selection Photon candidates selected in physics analysis are combined with other candidates or tracks in order to reconstruct beauty or charmed hadrons. To suppress the combinatorial background, it is beneficial to apply a second-stage selection on the neutral clusters that is based on multi-variate methods. To evaluate the performance of this second-stage selection, and in particular to investigate its dependence on SPD/PS information and on event multiplicity, several boosted decision tree (BDT) [84] algorithms have been developed according to the sample under study.

For the low luminosity ($\nu = 2.0$) sample, two selections have been developed, based on the shape of the energy deposited in the cluster, the fraction of energy in the central cell with respect to the total cluster cell, the energy in the corresponding HCAL cells (extrapolating with respect to the interaction point), the variable χ^2_{2D}, and finally which of the three regions of the calorimeter the signal candidate is found in. One selection considers the preshower energy in front of the ECAL cluster and the hit information from the SPD, the other does not have access to this information. Figure 3.15 (a) shows the signal efficiency and background retention of the two algorithms for candidates with $p_{\text{T}} \geq 200\,\text{MeV}/c$, quantifying the effect of the removal of the SPD/PS. An absolute reduction of 10 to 15% in the efficiency is observed at a fixed background retention.

The occupancy of the ECAL may also have an impact on the photon identification efficiency. Hence, three independent BDT have been trained individually at each of the three upgrade luminosity settings considered. The compared performances of the three algorithms are shown in Fig. 3.15 (b) on their respective samples. No significant difference is observed among the three

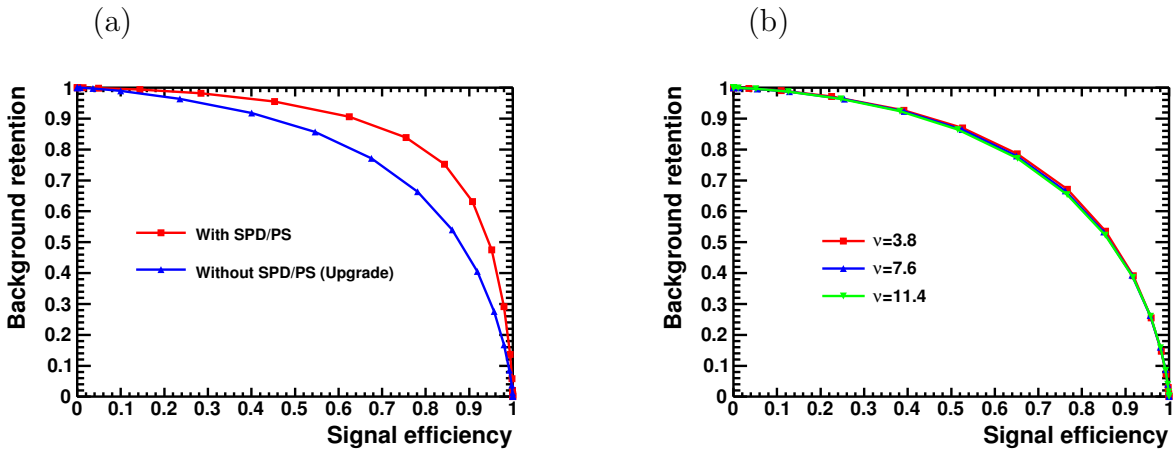

Figure 3.15: Signal efficiency versus background retention for photon selection BDTs with $p_{\mathrm{T}} \geq 200\,\mathrm{MeV}/c$. (a) compares BDTs with and without SPD/PS information; (b) compares BDTs without SPD/PS information trained at three different luminosities, here specified by the pile-up parameter ν.

algorithms both for the signal and the background. It is concluded, therefore, that only the removal of the SPD/PS has a significant impact on the photon identification performances of the upgraded calorimeter.

(ii) Electron identification

The electron identification performance has been studied using the same samples as already discussed, plus two supplementary samples based on the upgrade pile-up conditions $\nu = 3.8$ and 7.6, but where the SPD, PS and lead converter were not removed. The signal was selected using upstream photon-conversions without relying on the true information of the simulation. The background sample is selected through simulation truth matching information. The conversion signal candidates are built from oppositely-charged pairs of tracks, having a di-electron mass $\mathrm{M}(\mathrm{e}^+\mathrm{e}^-) \leq 50$ MeV/c^2, a vertex $\chi^2_{\mathrm{vtx}} \leq 5$, a z position of the vertex $Z_{\mathrm{vtx}} \geq 900$ mm and pointing to a primary vertex. The transverse momentum of the electron candidates is required to be larger than 100 MeV/c and the probability of the track fit must satisfy $\mathrm{Prob}(\chi^2_{\mathrm{tr}}, \mathrm{NDF}) > 1\%$. The hadron tracks of the event (as defined by the true simulation association) constitute the background sample. They are also required to pass the $p_{\mathrm{T}} \geq 100$ MeV/c and $\mathrm{Prob}(\chi^2_{\mathrm{tr}}, \mathrm{NDF}) > 1\%$ criteria.

The background E/p distribution is essentially smooth at the position of the signal peak and a rather clean photon-conversion signal is obtained. Two momentum ranges have been considered: $0 < p < 10$ GeV/c and $p > 10$ GeV/c.

The mis-identification rate has been studied for a signal efficiency of 80% or 90%, using the standard LHCb electron selection method based on the calorimeter and the RICH detector information and without any specific tuning related to the particular geometry of the upgraded detector. Table 3.7 shows the electron mis-identification rates obtained for $\nu = 2.0$, 3.8 and

Table 3.7: Typical electron performance in terms of mis-identification rate (in %) at $\varepsilon = 80$ and 90% for $\nu = 2.0$, 3.8 and 7.6 samples and the two studied geometries.

Momentum (GeV/c)	SPD/PS $\nu = 2.0$	SPD/PS $\nu = 3.8$	no SPD/PS $\nu = 3.8$	SPD/PS $\nu = 7.6$	no SPD/PS $\nu = 7.6$
selection efficiency $\varepsilon = 80\%$					
$0 < p < 10$	0.62	0.57	4.6	3.2	9.0
$p > 10$	0.16	0.12	0.16	0.29	0.32
selection efficiency $\varepsilon = 90\%$					
$0 < p < 10$	2.1	2.5	11	12	18
$p > 10$	1.1	0.73	0.72	1.3	1.4

7.6 and the two geometries (for the last two conditions only). Two regimes clearly appear. For low momentum electrons the background rejection worsens significantly as the luminosity increases. An additional degradation is seen when the SPD/PS is removed. However for the higher momentum sample, which is of relevance for most LHCb physics studies, the absence of the SPD/PS has very little effect, and also the performance is much more stable as the luminosity is raised.

3.5 Project organisation

3.5.1 Responsibilities and costs

The responsibility for the project is shared among the institutes listed in Table 3.8. The manpower effort of the contributing institutes will cover the hardware developments and the need for engineers. The LHCb calorimeter software must evolve from the present simulation and reconstruction code to that required for the new beam and detector conditions at the upgrade. The manpower for this task will be assigned in the near future and will mostly come from those physicists working on the current calorimeter software.

Table 3.8: List of the work packages and division of responsibility between institutes.

Work package	Institute(s)
Analogue electronics	Univ. Barcelona (Spain)
Digital electronics (FEB, Control Board)	LAL Orsay (IN2P3) (France)
High-Voltage, Control and monitoring	IHEP, INR and ITEP (Russia)
Radiation tolerance studies	IHEP, INR and ITEP (Russia)
Mechanics	LAPP Annecy (IN2P3) (France)

Table 3.9 summarises the present cost estimation for the calorimeter upgrade project. A 15% contingency has been added to the cost of the Front-End boards, the control boards, and the ECS adaptation of the HV, monitoring and calibration systems. This is to account for associated risks, related for example, to the impossibility to have a shared engineering run for the ASIC analogue electronics production.

Table 3.9: Cost estimate for the calorimeter upgrade.

Calorimeter			Costs [kCHF]
Electronics			
	Front-End	270 boards	770
	Control boards	21 boards	62
	Optical Links	five links/FEB	323
	Readout boards	TELL40/SOL40	653
	ECS (HV, control and monitoring)	Mezzanines and GBT fanout	54
	Crates		40
TOTAL			**1902**

Table 3.10: Calorimeter upgrade project milestones.

Date	Milestone
2014/Qtr 3	Analogue design choice
2016/Qtr 1	Complete FEB design
2016/Qtr 3	Complete control board design
2016/Qtr 3	Complete GBT mezzanines/fanout design
2018/Qtr 1	Ready for installation

3.5.2 Schedule

Figure 3.16 presents the schedule for the remaining R&D work, construction and commissioning. The most important milestones in this schedule are summarised in Table 3.10.

3.5.3 Safety aspects

The ECAL and HCAL sub-detectors comply with the safety policy at CERN (see Ref. [66]) and we will follow the safety rules and codes that are relevant for their modifications and operation. This concerns essentially the safety instructions

- for the "use of plastics and other non-metallic materials at CERN with respect to fire safety and radiation resistance" (use of polystyrene scintillator material in the modules),
- the dynamic behaviour under seismic excitation,
- the high-voltage to power the photo-multipliers,
- and the radioactive ^{137}Cs source used to calibrate the HCAL.

The removal and installation procedures for the modules of the ECAL during the LS3 will be determined according to the agreed safety measures and all lifting tools will be constructed according to the appropriate norms.

During operations on the detector itself and especially for the replacement of the ECAL inner modules, dose planning for the intervention and optimization following the ALARA principle

will be applied. All material removed will be traced and checked for radioactivity. Similarly, new installed material will be registered into the traceability database. Disposal of radioactive material will follow the rules and pathway established at CERN. Evaluation of the amount of radioactive waste expected due to the installation of new upgrade components and final disposal at decommissioning will be carried out as part of what is expected of the LHCb upgrade project as a whole.

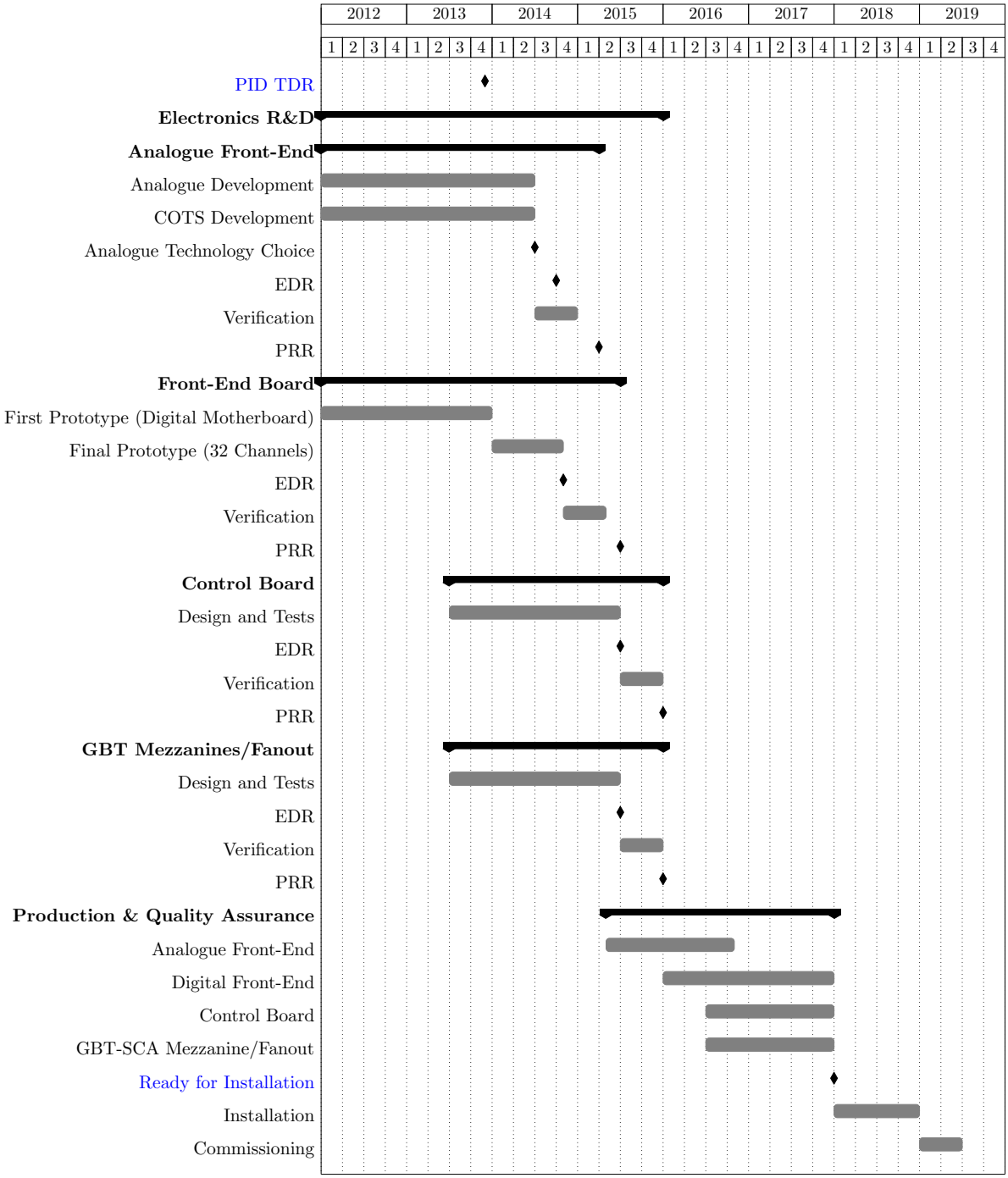

Figure 3.16: Gantt chart for the remaining work on the calorimeter upgrade R&D, the construction and commissioning.

Chapter 4

Muon system

4.1 Introduction

The reconstruction and identification of muons are key attributes of the particle identification system of LHCb, since decay channels of b– and c–hadrons with muons in the final state represent a crucial part of the physics programme of the current and upgraded LHCb detector. In particular, the study of very rare decays such as $B_s^0 \to \mu^+\mu^-$, $B^0 \to \mu^+\mu^-$ and $B^0 \to K^*\mu^+\mu^-$ can provide indirect evidence of New Physics effects. In addition, many other key channels of the precision physics programme envisaged for the upgraded LHCb experiment have muons in the final state, such as decays involving J/ψ mesons and semileptonic modes.

4.1.1 Physics requirements

The LHCb muon detector uses the penetrating power of muons to provide a robust muon identification. The heavy-flavour content of selected events is enhanced by requiring the candidate muons to have high transverse momentum, p_{T}. The same unique properties are used to provide a powerful B-meson flavor tag.

The present LHCb muon system [11], shown in Fig. 4.1, consists of five stations: the first station, M1, is located in front of the calorimeters and is important for the p_{T} measurement at the earliest trigger level; the remaining four stations, M2 to M5, are placed behind the hadronic calorimeter and are interleaved with iron walls that act as muon filters. The stations are equipped with Multi–Wire Proportional Chambers (MWPCs), except for the innermost part of station M1 where Gas Electron Multiplier (GEM) detectors are used. The stations are divided into four regions, each one equipped with chambers of different granularities to cope with the large variation in particle rates passing from the central part to the detector periphery.

The main requirement for the muon system at the upgrade is to guarantee a high reconstruction and identification efficiency for muons, while keeping the misidentification of pions and other particles as low as possible, up to luminosities of $2 \times 10^{33}\,\mathrm{cm}^{-2}\mathrm{s}^{-1}$. The performance of the present detector meets or even exceeds [85, 86] the specifications imposed in the TDR [87, 88]. However, since the upgraded LHCb will be readout at 40 MHz and deploy a flexible software-based trigger, the momentum resolution requirement imposed upon the current muon trigger can be relaxed for the upgraded detector.

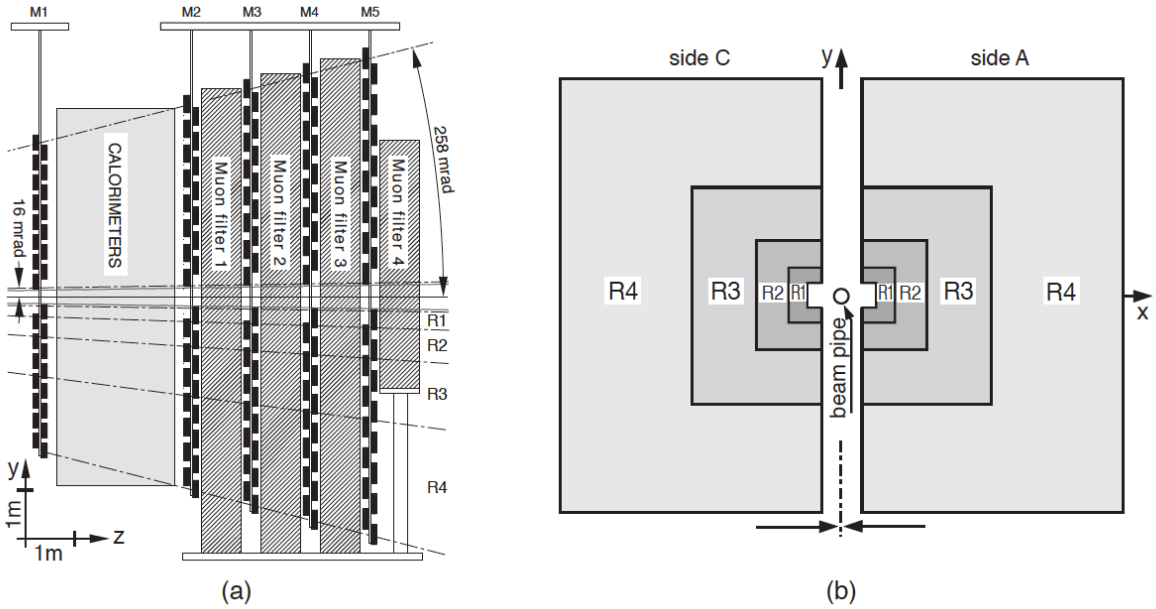

Figure 4.1: (a) Side view of the LHCb Muon Detector. (b) Station layout with the four regions R1−R4 indicated.

4.1.2 Upgrade overview

The muon system is the most shielded sub-detector of LHCb and particle rates will be tolerable up to an instantaneous luminosity of 2×10^{33} cm^{-2} s^{-1} at 14 TeV collision energy in all stations apart from M1, which will be removed in the upgraded experiment. The particle flux experienced by the innermost regions of station M2 is expected to be very high, and so additional shielding will be installed around the beam-pipe behind the HCAL to reduce the occupancy in these regions. The existing front-end electronics is already read out at the rate of 40 MHz intended for the upgraded experiment, in order to provide information to the current L0-muon trigger. On the other hand, the off-detector readout electronics provides full hit information (position and time) only at a rate of 1 MHz, and is not compliant with the new fast communication protocol based on the GBT chipset. Hence the off-detector readout electronics must be completely redesigned.

The upgrade programme for the muon system can therefore be summarized as follows:

- removal of station M1;
- design of new off-detector readout electronics compliant with full 40 MHz readout and the new GBT–based communication protocol;
- installation of additional shielding around the beam pipe in front of station M2.

Ageing of detectors is a concern after LS3, especially in the innermost regions of station M2. An R&D programme on new more radiation tolerant detectors is therefore ongoing.

This document is organized as follows: Sect. 4.2 discusses the detector requirements and specifications; the technical design of the new readout electronics is described in detail in Sect. 4.3,

as this is the only part of the upgraded muon system that will be fully redesigned; the expected physics performance of the muon detector in the high-luminosity running conditions is described in Sect. 4.4; finally, in Sect. 4.5, the project organisation is presented, together with details on planning, manpower and costs.

4.2 Detector specifications and overview

The basic function of the muon system is to identify and trigger on muons with high efficiency. This requirement must be maintained up to an instantaneous luminosity of 2×10^{33} cm^{-2} s^{-1} and for an integrated luminosity of 50 fb^{-1}. The detector efficiency is mainly limited by the intense flux of charged and neutral particles especially in the innermost regions close to the beam pipe. In the same regions, detector ageing must also be taken into account, especially in view of the large integrated luminosity foreseen. Because of the importance of these issues, this section opens with a brief overview of the relevant results concerning the performance of the muon detector at high luminosity.

4.2.1 Muon detector performance at high luminosity

The high-rate performance of the MWPCs for the muon detector was tested using a 100 GeV muon beam superimposed upon the 662 keV γ flux of variable intensity produced by the ^{137}Cs radioactive source at the CERN Gamma Irradiation Facility (GIF) [89]. The detectors were tested with current densities of up to approximately 30 nA/cm^2 which is the value expected in the most irradiated chamber of station M2 at 1×10^{33} cm^{-2} s^{-1}.

By means of the muon beam it was also possible to study the behaviour of the front-end electronics in the high rate environment. The muon detection efficiency and the response time resolution were studied as a function of the hit rate up to 1 MHz per front-end electronics channel. Once the detection efficiencies have been corrected for the effect of dead time (2.0 to 2.5% at 1 MHz per front-end electronics channel), both parameters show a behaviour in the presence of high particle fluxes that is very similar to that measured without photon background. Therefore, except for dead time effects, no deterioration is expected in the performance of the detectors. Based on these results we expect that possible space charge effects that may arise at $\mathcal{L} = 2 \times 10^{33}$ cm^{-2} s^{-1} will be minor. Potential inefficiencies can be recovered since the chambers are composed of four gas gaps which provide the necessary redundancy in the system.

The behaviour of the muon detector in upgrade conditions was also studied in 2012 with two dedicated tests: a run at a luminosity of 1×10^{33} cm^{-2} s^{-1} and a run at lower luminosity but with 25 ns bunch spacing. Results from the run at high luminosity [90] confirm that very little space-charge effect is visible and that the inefficiencies are dominated by the dead time alone.

MWPC ageing has been studied in tests at the CERN GIF and at the ENEA Calliope Gamma Facility [91]. A total charge of about 0.45 C/cm was accumulated by the detectors under test with no degradation in performances. However, this value is only 70% of the maximum integrated charge expected in the inner region of station M2 over the 50 fb^{-1} of integrated luminosity foreseen for the upgrade [7]. The average values for the expected accumulated charges in the most irradiated chambers for each region are summarized in Table 4.1. Detector ageing is therefore a concern for after LS3, by when about half of the luminosity will have been collected. An R&D programme focused on more radiation tolerant chambers is ongoing [92], as briefly described in Sect. 4.2.4.

Table 4.1: Average deposited charge (C/cm of wire) after 50 fb^{-1} in the most irradiated chamber of each station and region of the muon system.

	R1	R2	R3	R4
M2	0.67	0.42	0.10	0.02
M3	0.17	0.08	0.02	0.01
M4	0.22	0.06	0.01	0.004
M5	0.15	0.03	0.01	0.003

4.2.2 Upgraded detector layout

As already explained in the LoI [68] and the FTDR [8], station M1 will not be needed at the upgrade. While it is crucial for guaranteeing an adequate muon momentum resolution in the current L0 trigger, the huge hit occupancy expected at upgrade luminosities would make a correct association of M1 hits to the muon track segments virtually impossible and thus reduce the usefulness of this station for triggering and reconstruction purposes. On the other hand, in the context of the foreseen Lower Level Trigger (LLT) in the initial phase of the upgrade, the muon momentum resolution requirements can be relaxed. In addition, M1 is not used for the muon identification algorithms, which will be a fundamental part of the High Level Trigger (HLT) and are widely used in the physics analysis.

The physical layout of stations M2 to M5 will not be modified, as it provides the required trigger and particle identification efficiency. However, the outermost region (R4) of station M5 will be subject to a high background coming from particles that are back-scattered from a corrector magnet located in the LHC tunnel just behind station M5. The large logical channels[1] [87, 88] in M5R4, which have an area of up to about 0.5 m^2 resulting from the logical-OR of 24 front-end channels, already have a high occupancy because of this background, which induces inefficiencies at the level of a few percent due to dead time. To mitigate this effect additional shielding [93] has been installed during LS1 behind Muon station M5, as shown in Fig. 4.2.

To reduce further these inefficiencies, which will become more severe at upgrade running conditions, it is planned to increase the granularity of the logical channels in M5R4 by eliminating the so called Intermediate Boards (IB) [94] (where the logical-ORs between front-end channels are performed) and replacing them by off-detector electronics boards (ODE).

Extra shielding

Additional shielding will be installed around the beam-pipe behind the HCAL to ensure a better absorption of shower particles and to reduce the particle flux in the innermost part of muon station M2.

In the present detector the nuclear interaction length in front of M2 is about $6.8\lambda_I$. This is 33% less compared to the thickness of the hadron absorber foreseen at the time of the Technical Proposal of LHCb [95], when the total calorimeter and hadron absorber thickness before muon station M2 was 10.4 λ_I.

[1] In the muon system the logical channels are logical combinations (OR) of front-end readout channels that ultimately provide the spatial information

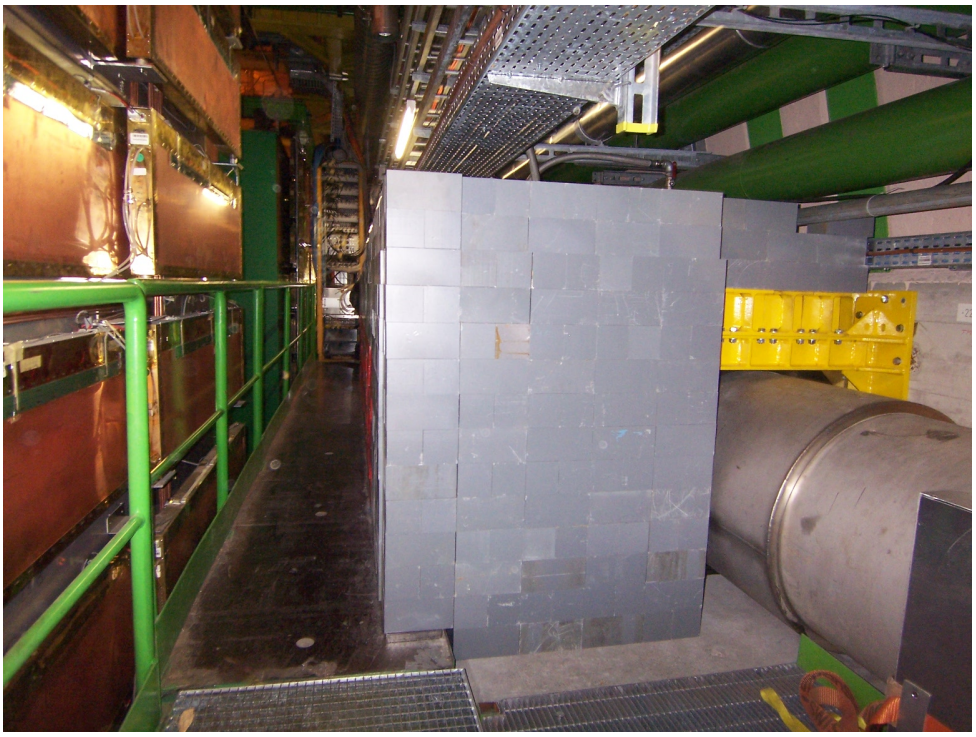

Figure 4.2: Additional shielding installed behind M5 during LS1.

The reduced absorber thickness is an acceptable solution for LHCb when running at luminosities up to at least 5×10^{32} cm^{-2}s^{-1}. However, with the planned luminosities for the LHCb upgrade, the hit rate in the innermost muon chambers will be very high, mainly due to insufficient absorption of particles produced in hadron showers close to the beam pipe. Therefore a study has been carried out to increase the nuclear interaction length before the chambers of station M2 close to the beam-pipe. Different types of shielding were considered and assessed using Monte Carlo simulations [96].

The innermost cells of the hadron calorimeter contribute substantially to the rate of the current L0 hadron trigger, while at the same time providing a negligibly small fraction of the triggers for genuine hadronic B decays. These cells were therefore already disabled in the L0-hadron trigger at the end of the 2012 LHC pp physics run. Taking advantage of this opportunity, a solution has been studied where the Cockroft-Walton bases and the PMTs of the four innermost cells of the hadron calorimeter left and right of the beam-pipe are removed and the space is filled with an iron or tungsten absorber, as indicated in Fig. 4.3. The depth of the additional absorber is about 30 cm. Simulations have shown that this modification allows the rate in the chambers of region R1 in station M2 to be reduced by 26% on average when tungsten is used as absorber material. Hence, inconveniences due to the high hit rate in this part of the muon system can be mitigated substantially. Studies on how to implement this shielding are in progress. The basic idea is to attach it to the present beam plugs under the hadron calorimeter. As the amount of work to realize this shielding is minor, it might be implemented already before LS2. Studies are also ongoing to extend the size of the additional shielding further.

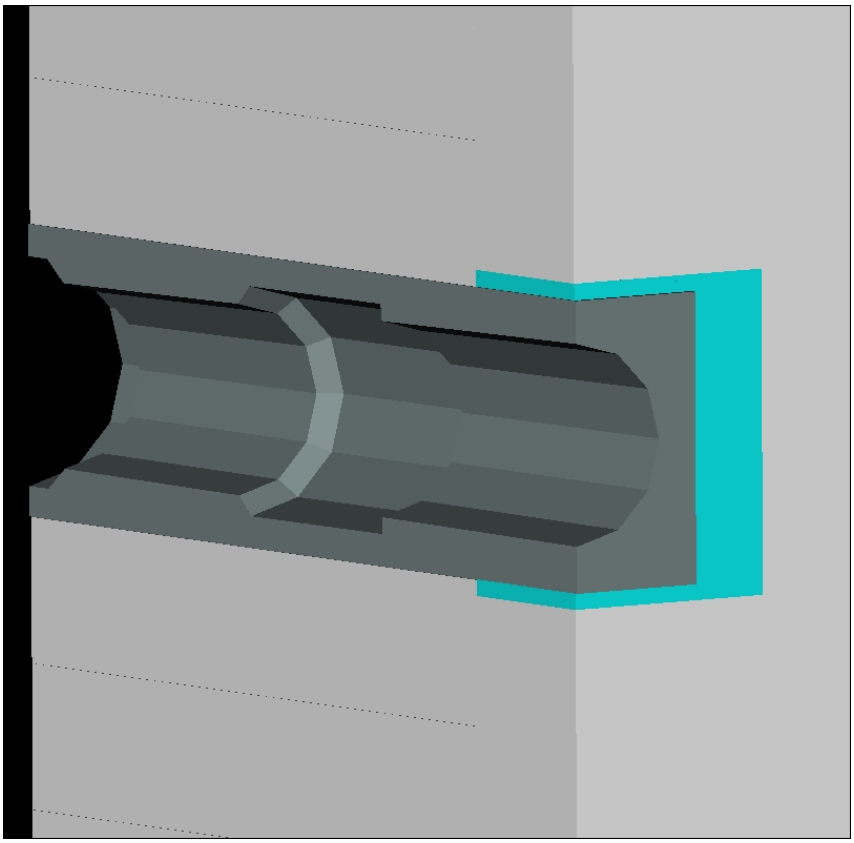

Figure 4.3: Location of the extra shielding (shaded rectangular area) foreseen around the beam plug at the location of the HCAL readout.

Spare chambers

In order to operate the muon detector safely for the foreseen ten years of data taking at high luminosity, it will be necessary to have an adequate supply of spare MWPCs. The number of detectors required has been estimated from the current replacement rate. Five MWPCs were replaced after the 2010 data taking period, two after 2011 and six are now being replaced after the end of LHC Run 1. There is no evident correlation between the replaced MWPCs and the average particle rate at which they operated before they got damaged. This implies that, at least for the time being, there is no evidence of damage induced by radiation.

Possible ageing effects are expected only in the innermost regions of station M2, so that a MWPC replacement rate similar to the one observed until now is foreseen. As a consequence 33% MWPC spares for the R1 and R2 regions, 20% MWPC spares for the R3 regions and 10% MWPC spares for the R4 regions are planned. The number of spares for the LHCb upgrade phase, together with the new MWPCs that need to be built, are summarized in Table 4.2. The spare MWPCs will be identical to those currently installed in the muon system.

Table 4.2: Muon system spare chambers for the LHCb upgrade. The number of installed MWPCs is given in the second column; the number and percentage of available spare MWPCs are given in the third and fourth columns; the total number and percentage of spare MWPCs needed (target) are given in the fifth and sixth columns; the number of MWPCs to be built is given in the seventh column.

Region	Installed	Avail.	Avail. (%)	Target	Target (%)	To be built
M2R1	12	4	33	4	33	0
M2R2	24	3	13	8	33	5
M2R3	48	6	13	10	20	4
M2R4	192	14	7	20	10	6
M3R1	12	4	33	4	33	0
M3R2	24	3	13	8	33	5
M3R3	48	6	13	10	20	4
M3R4	192	18	9	18	9	0
M4R1	12	4	33	4	33	0
M4R2	24	4	17	8	33	4
M4R3	48	8	17	8	17	0
M4R4	192	23	12	19	10	0
M5R1	12	4	33	4	33	0
M5R2	24	3	12	8	33	5
M5R3	48	10	20	10	20	0
M5R4	192	2	1	20	10	18
Total	1104	116		168		51

4.2.3 New muon system electronics requirements

The muon readout electronics [87, 88] convert the analogue signals extracted from the detector front-end channels into logical channels (essentially X and Y strips), which are input to the L0–muon trigger processors.

The analogue signals are amplified, shaped and discriminated by means of a custom ASIC named the CARIOCA [97]. The digital outputs of the CARIOCAs are combined in logical-OR both on the front-end boards (via another custom ASIC, DIALOG [98]) and in the Intermediate Boards (IB) [94] to generate the logical channels. The logical channels are processed in the Off Detector Electronics (ODE) system [94, 99, 100], based on the custom SYNC chip [101], where they are synchronized with the master LHCb clock and grouped in trigger units. These data are serialized through GOL chips [102] and sent to the L0 muon trigger processors at a rate of 40 MHz by means of optical interfaces. The arrival time of each channel with respect to the bunch crossing is measured through a 4 bits TDC with a resolution of about 1.5 ns. The data are buffered in internal memories and sent to TELL1 [103] boards at a maximum rate of 1 MHz. The TDC information is of fundamental importance to synchronize all the readout channels and ensure the required time resolution [87, 88]. The front-end chips (CARIOCA and DIALOG) are controlled via the Service Board (SB) system [104], which implements also a pulsing system (PDM), used to synchronize and to time align the detector. Both ODE and SB systems rely on

the TFC system [105] from which they receive the master clock, the synchronization signals and the L0 commands. A CANBus based ELMB board [106] is used for the ECS interface [107].

This architecture, although well matched to current operation, is not suited to the requirements of the upgrade. The TDC information is in fact extracted at a rate of 1 MHz only and the current optical communication system, based on the GOL chipset, needs to be replaced with the new GBT chipset [**?**, 108]. In addition, to provide all the synchronization signals the present clock distribution system (the TFC), would have to be maintained in operation or emulated for the muon system alone. Concerns about obsolescence of certain electronic components have also to be taken into account.

To address these problems, while also optimising manpower, effort and costs, it has been decided to replace the ODE, the SB and the PDM with new electronic boards, maintaining the present crates and power supply system.

The new electronics must be electrically and mechanically compatible with the existing system, in order to guarantee a simple and fast replacement. It will use the new GBT and Versatile link [37, 38] components to implement the trigger, DAQ, TFC and ECS interfaces and to be fully compliant with the LHCb upgraded electronics specifications. Finally the upgraded electronics, maintaining the present functionalities, will also have to:

- allow the TDC readout at a rate of 40 MHz;
- allow for a possible increase in readout channel granularity;
- minimize the number of readout links to allow the trigger implementation in the new data acquisition readout boards, the TELL40s [15].

4.2.4 R&D on new detectors for the inner regions

To cope with the high particle rates in the innermost regions of stations M2 and M3 and with the possible problems of ageing and of inefficiency induced by large dead time, an R&D programme on more radiation tolerant and higher granularity detectors is ongoing. This programme, detailed in Ref. [92], is briefly outlined here for the sake of completeness, but is not considered part of the upgrade project described in this TDR.

The main objective of this R&D study is the design of new high granularity detectors for regions R1-R2 of stations M2 and M3 and of their front-end electronics. The baseline detectors currently foreseen are anode-pad triple-GEM detectors for the R1 regions and cathode-pad MWPCs for the R2 regions. These detector technologies, according to the experience acquired during the LHC Run 1, appear to be a promising solution, both from the point of view of their rate capability and their radiation hardness. These detectors will have high-granularity pad readout to reduce the particle rate on each physical readout channel, in order to overcome the efficiency losses due to increased dead-time when operating in upgrade conditions. The new readout granularity will remain compatible with the current muon detector projective layout to allow the operation of the LLT without major modifications. New high-granularity MWPCs will be equipped with the current CARDIAC front-end boards based on the CARIOCA and the DIALOG chips. The very high channel density needed for the triple-GEM detectors in R1 will require the development of a new highly-integrated front-end ASIC, which will be built in modern radiation-hard technologies. To simplify the installation and the readout of the new high-granularity triple-GEM detectors, special readout boards will be developed. These boards will be directly read out via optical links. This R&D programme will continue until 2019.

Recent tests performed at high luminosity suggest that the muon system performances should not degrade significantly at instantaneous luminosities of up to 2×10^{33} cm^{-2}s^{-1}. However it is mandatory to develop additional solutions to guarantee an efficient muon system during the LHCb high luminosity phase.

4.3 Upgraded readout and control electronics

The general layout of the upgraded muon readout and control electronics is very similar to the present system and the new boards are electrically and mechanically compatible with the existing ones to guarantee a simple and fast replacement and minimize the recabling. The main component of the new readout is the new Off-Detector Electronics Board that will be equipped with a new custom ASIC, the SYNC chip which is an evolution of the present ASIC. The front-end electronics will be controlled and configured through a newly designed control system that will make use of the GBT and Versatile link components to implement a TFC interface and of the GBT-SCA chip to interface the GBT to the I^{2}C control lines for the front-end boards. A schematic view of the upgraded muon electronics is shown in Fig. 4.4.

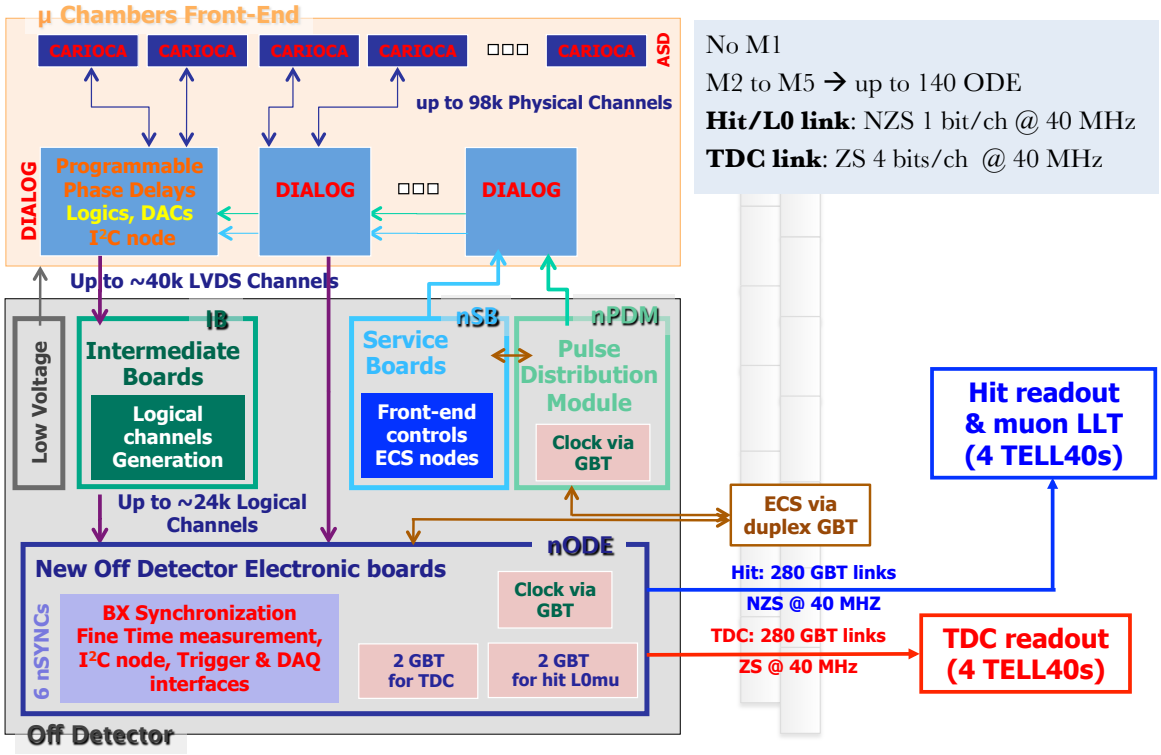

Figure 4.4: Upgraded muon system electronics architecture.

4.3.1 New off-detector readout board

The nODE

A new Off Detector Electronics board (nODE) will replace the present ODE board and will be mechanically and electrically compatible with the current electronics. The nODE will have up to 192 input channels and will be based on a new radiation tolerant custom ASIC, the nSYNC, which will integrate all the required functionalities (clock synchronization, bunch crossing alignment, trigger hits production, time measurements, histogram capability and buffers). The nSYNC will also handle the zero suppression algorithm for the TDC data and the interfaces to the data acquisition and TFC/ECS systems. Such interfaces will be based on the GBT and Versatile link components to guarantee full compatibility with the new electronic systems foreseen for the LHCb upgrade. The so-called DAQ interface must allow a unidirectional data transfer of the binary hit information to the corresponding TELL40 boards, where also the LLT muon trigger will be implemented. The hit map must be sent at a rate of 40 MHz with minimum data latency and without any kind of zero suppression or data truncation. All the logical channels belonging to the same Trigger Unit (TU) will be grouped in a single data frame and will be sent to the trigger processor on the same link.

The so-called TDC interface must allow a unidirectional data transfer of the TDC information to the TELL40 boards. The TDC data need to be zero suppressed and formatted before transmission to optimize the number of required links. The processing and transmission time is not fixed and it fluctuates in each bunch crossing depending on the detector occupancy. Therefore, pipeline stages and buffers will be implemented and data truncation is foreseen.

The zero suppressed TDC data require a geographic addressing to be identified. This information is contained in the hit map that is also used for the trigger purposes. Therefore in order to avoid duplicating such information, the same hit map will be used both for trigger algorithm and for TDC data address decoding. Such a choice allows an optimization of the bandwidth usage and a reduction in the number of links. The hits and the TDC data will use separate links for the transmission (hit links and TDC links respectively) to minimize the latency of the data for the trigger system and to allow a much simpler management of the zero suppression, data truncation and data buffering.

Only a single type of nODE board is foreseen for all muon stations/regions, therefore a modularity of 96 bits per hit link is required to fit all types of trigger unit topologies. As shown in Table 4.3, in different stations/regions, the TU can have 10, 14, 16, 24 or 28 logical channels and the nODE can have 6, 8 or 12 (120, 168 or 192) active TUs (active input channels). The 96 bits modularity is the only one that fits all the possible combinations.

Such a modularity necessitates the use of the GBT in WideBus mode, where up to 112 bits of data are available without any kind of Forward-Error-Correction (FEC) capability. Taking into consideration the expected error rate performance of the versatile link and considering that the present trigger links use with good efficiency an 8b/10b data encoding (having no correction capabilities and only a minimal capability of error detection), the WideBus is a reasonable choice. The 112 bits also allow a header (12 bits) to be included, containing some bits of the bunch-counter and/or other information. Two links per nODE are enough to transmit the hits information.

To measure the arrival time of the signals within the bunch crossing period, a 4-bits TDC with a resolution of about 1.5 ns will be used. To be consistent with the hits transmission, the TDC data will be sent out using two links per board with the GBT in WideBus mode (16 bits for

Table 4.3: Active logical channels and TU topology per nODE in different detector regions.

station	region	Active ch. per nODE	Logical ch. per TU	TU per nODE	TU per GBT
M2 or M3	R1	168	28	6	3
	R2	192	16	12	6
	R3	168	28	6	3
	R4	168	28	6	3
M4 or M5	R1	96 or 192	24	4 or 8	4
	R2	168	14	12	6
	R3	120	10	12	6
	R4	120	10	12	6

header and 96 bits for data). A data encoding without error correction capability is usable also for TDC data because such information is typically used for time alignment and data integrity is not an issue. A maximum sustainable detector occupancy of 25% can be reached.

The TFC/ECS interface will be implemented with a dedicated full duplex link per board. It will use a GBT in transceiver mode which acts as master and distributes the main clock to the other GBT and to the nSYNC chips. The TFC commands will be received and decoded by each nSYNC chip. The master GBT also provides the local ECS interface via a GBT-SCA chip. The ECS interface will be used to configure the electronics components of the board, to monitor their status and to download the time histograms.

The present crate and power architecture will be maintained in the upgrade. It is based on the MARATON system and it foresees three power lines with voltages from 2 V to 7 V. The electronics components of the nODE will require many different power voltages (1.2 V, 1.5 V, 1.8 V, 2.5 V and 3.3 V), therefore a dedicated power section with radiation tolerant DC-DC converters will be implemented on each board. Figure 4.5 shows a block schematic of the nODE board.

To match the future running conditions in terms of higher granularity and occupancy, the nODE will be compatible with the present IB board. In such a way a simple replacement of an IB with a nODE board will reduce the logical channels dimension and their occupancy. This is equivalent to the increase of detector granularity and leads to an increase in number of logical channels to be sent to the trigger system. The nODE architecture will also be compatible with any future higher granularity chambers if the present logical pad dimension will be maintained.

The nSYNC chip

The nSYNC will be the core of the nODE. It will receive the data coming from the detectors, synchronize them with respect to the bunch-crossing identification number (BXid) and send the binary information of the hits (that will also be used by the muon trigger) and the time information to the TELL40s. Data will be transmitted by interfacing the nSYNC to the GBT.

The nSYNC will have 32 input channels from which it will receive the LVDS data from the front-end electronics and from the IB system. Each channel will be equipped with a 4 bit TDC to measure the phase of incoming signals with respect to the LHCb master clock. The TDC information will be used internally to build a histogram of the incoming signal phase in order to perform the so-called fine-time synchronization that is crucial to achieve the required muon

system efficiency. The histograms will be read back through the ECS interface (I^2C or SPI). The TDC data will pass through the data flow together with the related hit information. These complex data will then be synchronized with respect to the BXid. In the nSYNC we foresee a 12-bit BXid counter that will be synchronized with the LHCb one by using the synchronization signal coming from the TFC through its own interface. The TFC information will come from a GBT housed in the nODE board. This information will be decoded inside the nSYNC. A block diagram of the nSYNC ASIC is shown on Fig. 4.6. After the proper BXid assignment to the complex data set, a frame header will be generated according to the requirements of the Electronics architecture of the LHCb upgrade specification document [36]. The frame header and the binary hit information will be sent via a GBT interface to the TELL40 recording the binary muon hits information, where also the muon LLT will be implemented. Using this information, the TDC data will be zero-suppressed (ZS) to reduce the required bandwidth. The frame header and the ZS TDC data will then be sent to the TELL40 recording the muon hit time via another GBT interface. Some programmable buffers are foreseen before the two GBT interfaces to guarantee the synchronization between data coming from different nSYNC.

The nSYNC chip will be configured and controlled through ECS using a standard interface such as I^2C or SPI. All the registers inside will be triple-voted and the configuration register will also have an automatic refresh system.

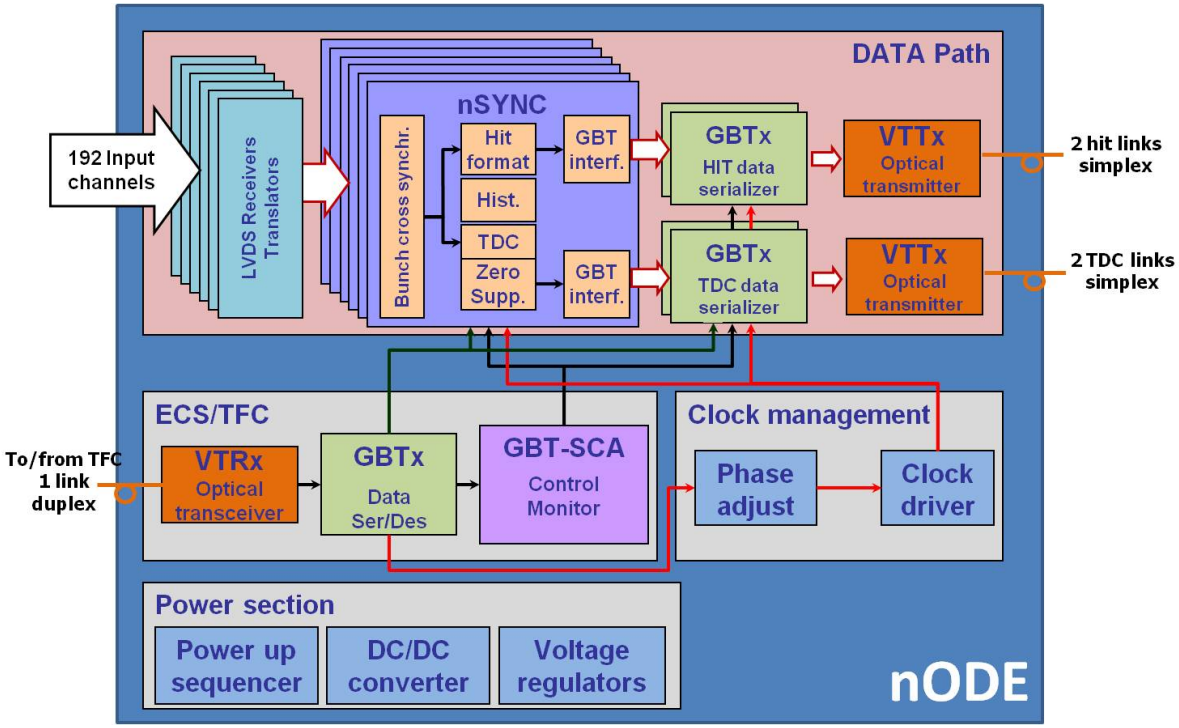

Figure 4.5: nODE block diagram.

4.3.2 New front-end control and pulsing boards

The current Muon Front-End Control (MuFEC) electronics is based on two custom boards, the Service Board (SB) and the Pulse Distribution Module (PDM), that communicate between themselves through a custom backplane. They are used to control, monitor and test every single channel of the detector front-end. The MuFEC allows the threshold and the counter registers of every single channel to be accessed and plays a fundamental role in the noise measurement and the threshold adjustment of the whole muon system. The MuFEC, together with the ODE boards, is also essential in detector time alignment, a procedure needed to achieve the required system efficiency. It allows the injection of calibration pulses at a specific bunch crossing and the delay calibration of every single muon detector channel.

The control electronics is housed in crates located close to the muon detector. In total, ten crates are used, each equipped with one PDM and up to 20 SBs. The PDM receives four CAN ports and distributes them to the SBs through the custom backplane. The programmable components of the boards are based on microcontrollers and flash memory technologies, which are fully radiation tolerant. The current system uses a total of 600 microcontrollers. Each microcontroller performs well defined tasks when specific commands are received via CANbus. The timing information is received from the TFC system via a TTCrx chip used to broadcast timing signals to the full muon system.

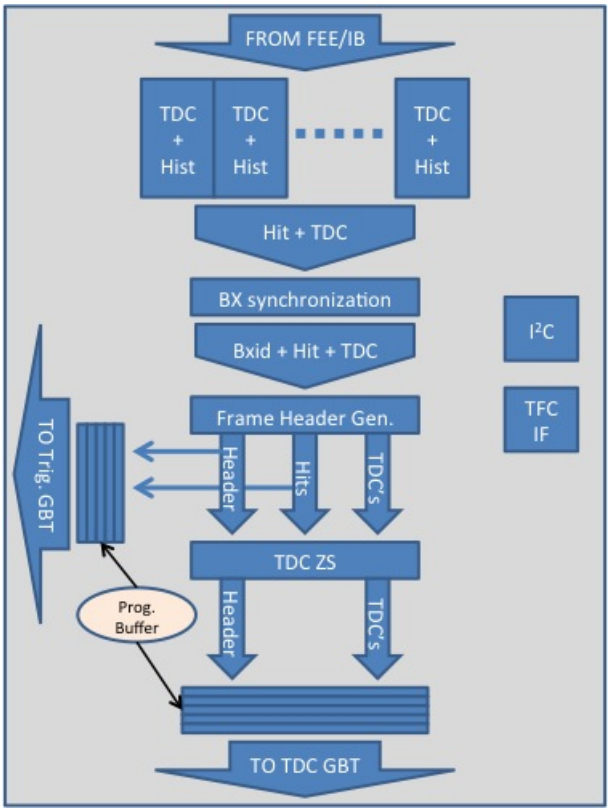

Figure 4.6: Block diagram of the nSYNC ASIC.

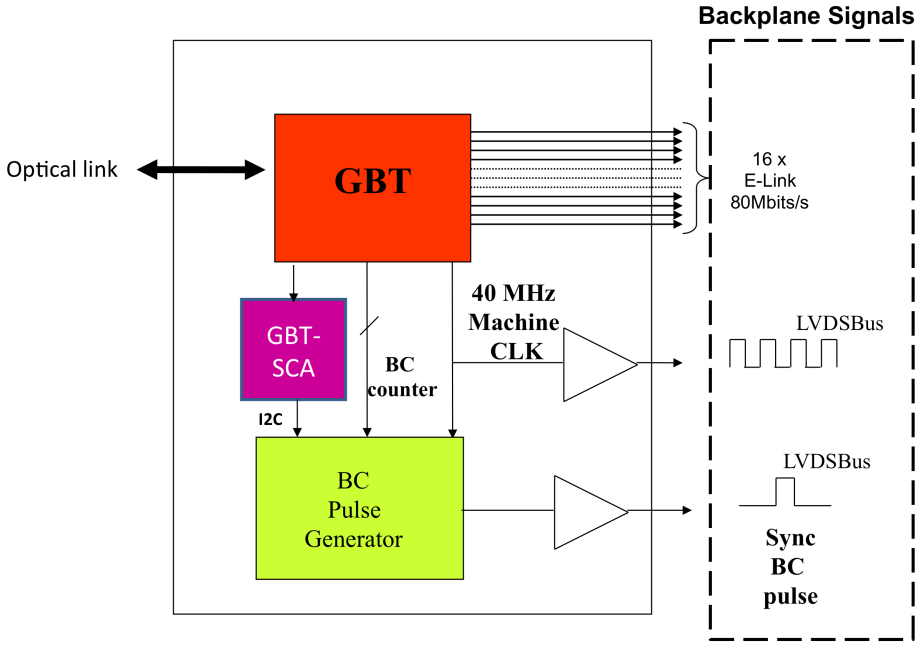

Figure 4.7: Block diagram of the nPDM board.

While maintaining the original architecture of the system for crate allocation and module partitions, the new MuFEC will use the GBT and Versatile link components to implement a TFC interface compliant with the new standard foreseen in the LHCb upgrade. Such an interface will not only allow the broadcasting of trigger and timing information, but will also provide a fast bidirectional data link for the experimental control system. An additional radiation hard chip, the GBT-SCA, will be used to control the I^2C lines to the front-end boards.

The new system will be built using three new components: a new PDM (nPDM) board based on the GBT and GBT-SCA chips; a new SB (nSB) board mainly based on the GBT-SCA and a radiation tolerant Actel FPGA (based on flash technology) to provide some external logic; and a new backplane to dispatch the communications channels (E-link) from the nPDM to the nSB boards. The block diagrams of the nPDM and the nSB are shown respectively in Figs. 4.7 and 4.8. The replacement of the CANbus with a faster data link will allow the removal of the local intelligence (the microcontrollers) from the control boards, and all system operations will be perfomed directly via software.

The MuFEC upgrade will largely benefit from the new timing and fast control architecture developed within the LHCb collaboration for the upgrade, avoiding the use of obsolete components.

4.4 Performance

The performance of the muon detector in the first LHCb running year has been studied in detail as described in Ref. [85]. The data consist of pp collisions at $\sqrt{s} = 7$ TeV taken during the 2010 LHC run. Due to the continous progress of the LHC machine operations, these data span a wide range of luminosity values, from 10^{27} to 10^{32} cm^{-2}s^{-1}. These sets of data have allowed a detailed

analysis of the observed rates, including the contribution of the spill-over, and of their scaling with luminosity and energy. These studies are the basis of the extrapolations to the upgrade conditions described in the following section. The results on rates and efficiencies described in Sect. 4.4.1 will be used in Sect. 4.4.2 to estimate the muon identification performance at the upgrade.

4.4.1 Expected rates on muon system

The particle rates measured in the various stations and regions of the muon detector are found to scale very well with the luminosity over several orders of magnitude. This allows a safe extrapolation of the rates expected at the upgrade luminosities. The projections to the upgrade conditions however require additional assumptions that are summarized here:

- for luminosities of 10^{33} cm^{-2}s^{-1} and 2×10^{33} cm^{-2}s^{-1} we assume $\nu = 3.8$ and $\nu = 7.6$, respectively, where ν is the average number of pp interactions per bunch crossing;
- as shown in Fig. 4.9 [85], the hit multiplicity per minimum bias trigger observed in data increases with the collision energy $E_{\rm cm}$ as $E_{\rm cm}^{a}$ with $a = 0.35 - 0.6$ depending on region and station. For a conservative extrapolation we assume $a = 0.6 \pm 0.2$;
- the in–time rate will increase with 25 ns bunch spacing due to spill-over.

The scaling behaviour of hit multiplicites is confirmed by looking at several multiplicity counters such as the number of tracks and the number of hits in various subdetectors. Each

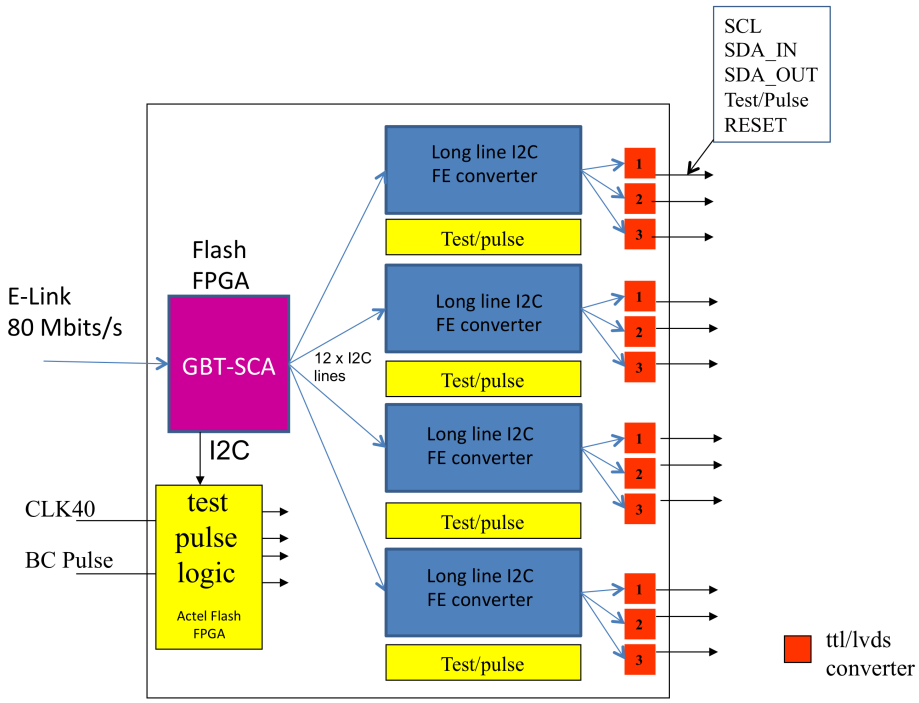

Figure 4.8: Block diagram of the nSB board.

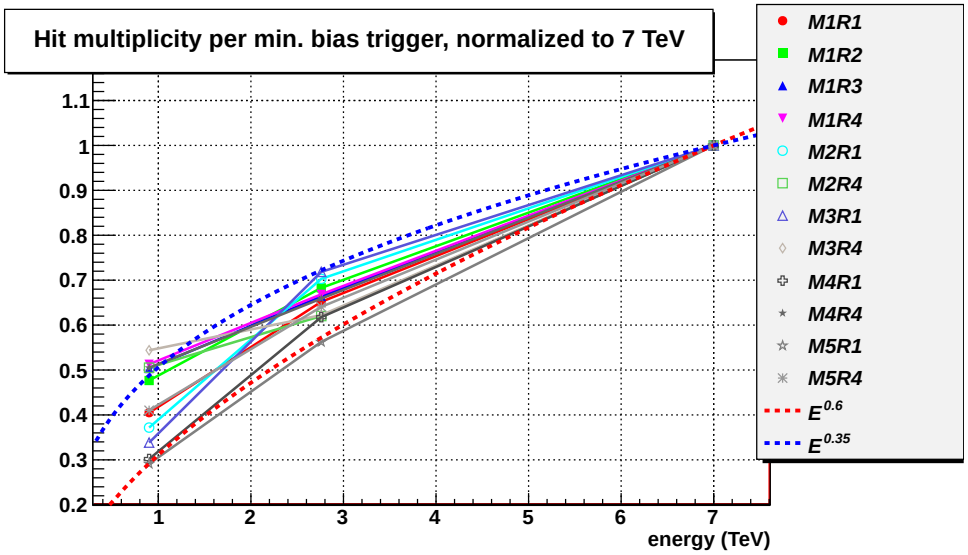

Figure 4.9: Evolution of hit multiplicity measured from data as function of the collision energy E_{cm}.

counter, normalized to the number of primary vertices, has been measured at 7 and 8 TeV on data samples from the inclusive selections of the $B_s^0 \to \mu^+\mu^-$ and $B \to h^+h'^-$ analyses. The ratio of the counters between 7 and 8 TeV is found to scale as $(8/7)^{0.6}$ within $\pm 5\%$. To take the scaling of hit multiplicity into account an effective average collision rate $\nu_{eff} = \nu \times (E_{cm}(\text{TeV})/8)^{0.6}$ is defined and used to extrapolate properly the hit rates from the measurements at 8 TeV to the upgrade luminosities. The assumed ν and ν_{eff} values are summarized in Table 4.4. The resulting hit rates expected in the different muon detector regions for the upgrade luminosities are reported in Table 4.5. The values are averages over the chamber with the minimum illumination, the whole region and the chamber with maximum illumination. The effect of the additional shielding discussed in Sect. 4.2.2 is included. According to simulations, the average rate is reduced by about 26% on the most irradiated region M2R1 thanks to this shielding. The quoted errors are due to the uncertainties on the extrapolation of the pp cross–section ($\pm 10\%$), the increase of hit multiplicity ($a = 0.6 \pm 0.2$) and the effect of the additional shielding.

Table 4.4: Values of ν and of the corresponding scaling factors ν_{eff} used for the rate extrapolations at the upgrade luminosities and 25 ns bunch spacing.

$\mathcal{L}$ ($\text{cm}^{-2}\text{s}^{-1}$)	ν	ν_{eff}
1×10^{33}	3.8	5.3
2×10^{33}	7.6	10.6

From the analysis of data taken at $\mathcal{L} = 1 \times 10^{33}$ $\text{cm}^{-2}\text{s}^{-1}$ during a test run in 2012 [90], it has been demonstrated that no space charge effects are expected at this luminosity. The only expected degradation of detector efficiency due to the increased rate is caused by the dead time

Table 4.5: Expected rates on the muon detector when operating at an instantaneous luminosity of 2×10^{33} cm^{-2}s^{-1} at a collision energy of 14 TeV. The values are averages, in kHz/cm^2, over the chamber with the minimum illumination, the whole region and the chamber with maximum illumination. The values are extrapolated from measured rates at 8 TeV.

Region	Minimum	Average	Maximum
M2R1	162 ± 28	327 ± 60	590 ± 110
M2R2	15.0 ± 2.6	52 ± 8	97 ± 15
M2R3	0.90 ± 0.17	5.4 ± 0.9	13.4 ± 2.0
M2R4	0.12 ± 0.02	0.63 ± 0.10	2.6 ± 0.4
M3R1	39 ± 6	123 ± 18	216 ± 32
M3R2	3.3 ± 0.5	11.9 ± 1.7	29 ± 4
M3R3	0.17 ± 0.02	1.12 ± 0.16	2.9 ± 0.4
M3R4	0.017 ± 0.002	0.12 ± 0.02	0.63 ± 0.09
M4R1	17.5 ± 2.5	52 ± 8	86 ± 13
M4R2	1.58 ± 0.23	5.5 ± 0.8	12.6 ± 1.8
M4R3	0.096 ± 0.014	0.54 ± 0.08	1.37 ± 0.20
M4R4	0.007 ± 0.001	0.056 ± 0.008	0.31 ± 0.04
M5R1	19.7 ± 2.9	54 ± 8	91 ± 13
M5R2	1.58 ± 0.23	4.8 ± 0.7	10.8 ± 1.6
M5R3	0.29 ± 0.04	0.79 ± 0.11	1.69 ± 0.25
M5R4	0.23 ± 0.03	2.1 ± 0.3	9.0 ± 1.3

of the readout electronics. This inefficiency can be computed measuring the in–time occupancy and the hit time profile for each channel and knowing the dead time of the readout chain. The latter has two components: the dead time of the CARIOCA chips, whose average value varies from 50 to 100 ns (depending on the the signal amplitude) and the dead time given by the programmable fixed length DIALOG digital output signals set to 18 ns during 2012. The effect of CARIOCA dead time is mitigated by the fact that the front-end electronics perform a logical OR of two independent detector planes. The effective dead time thus depends on the relative contribution to the rate from penetrating particles, firing simultaneously the two channels, and from low energy tracks detected by only one channel. The relative fractions of penetrating and low energy tracks were measured in a special run, where rates of the AND and OR of the two CARIOCA channels were measured. The fraction of hits due to penetrating particles is found to be as low as 7% on average for region M2R1.

The method is validated using special runs acquired with 25 ns bunch spacing, where the effect of dead time for a given ν is expected to increase with respect to runs at longer bunch spacing. The MWPC efficiency for the different regions was measured in runs with different values of ν and 25 ns or 50 ns bunch spacing. Data taking conditions with ν values of 2.6 and 25 ns bunch spacing correspond to a luminosity of 8×10^{32} cm^{-2}s^{-1}. The results are shown in Fig. 4.10.

To disentangle the effect of deadtime from the other effects contributing to the total chamber inefficiency, the variation of the measured inefficiency with ν is compared with the estimated inefficiency due to dead time and found in good agreement, as shown in Fig. 4.11. The uncertainty

on the estimated inefficiency due to the dead time is systematic and is dominated by the assumed CARIOCA dead time of 75 ± 25 ns.

Using the extrapolated rates from Table 4.5, it is now possible to estimate the dead time–induced inefficiency at upgrade luminosities. The results are summarized in Table 4.6. To obtain the full chamber inefficiency, the residual component due to intrinsic MWPC inefficiency must be added. This effect amounts to an additional inefficiency smaller than 1% and will be taken into account in the muon identification performance study described in Sect. 4.4.2. The effect of the additional shielding is included in the computation. Other means to achieve a reduction of rate and channel occupancy are under consideration. Notably, the reduction of logical channel size discussed in Sect. 4.3.1 was not considered in the extrapolations. The possibility for a further reduction of DIALOG signal length will be studied during Run 2.

4.4.2 Expected performance of the muon identification

The performance of the muon detector affects the physics results in a way that might be very different depending on the decay channel considered. It is therefore most informative to show the expected performance of the muon system using the muon identification itself as a figure of merit. The muon identification algorithms and their performances are described in details in Ref. [86]. The basic algorithm relies on the number of hits matching tracks extrapolated to the muon stations and is characterized by the binary variable IsMuon. Additional identification criteria can be applied using a combined $\mathrm{DLL}_{\mu\pi}$ variable based on the distance of matching hits from the extrapolated track in the muon stations combined with the information coming from RICH and calorimeter detectors [49]. The performances of the muon identification algorithms depend on the muon reconstruction efficiency, which in turn depends directly on the muon station efficiency and on the occupancy which affects the misidentification fractions.

The results of Table 4.6 can be used to estimate the effect of the extrapolated chamber

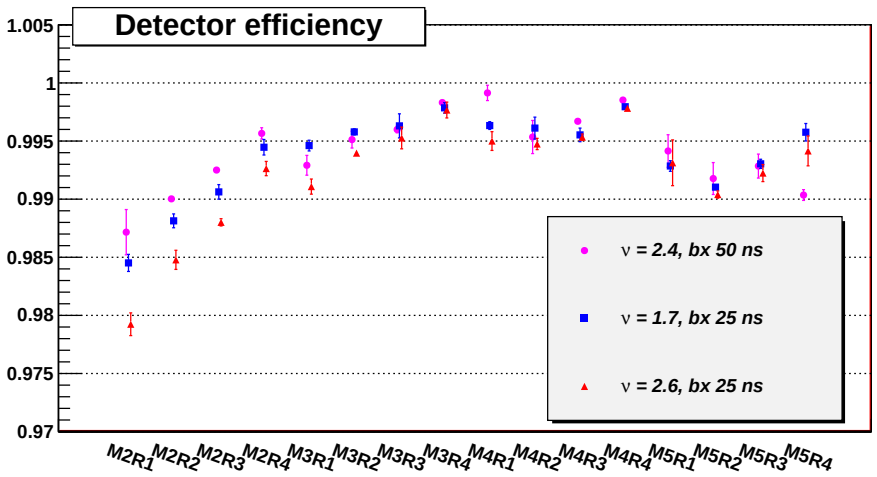

Figure 4.10: Average muon chamber efficiency per region per station in different data taking conditions.

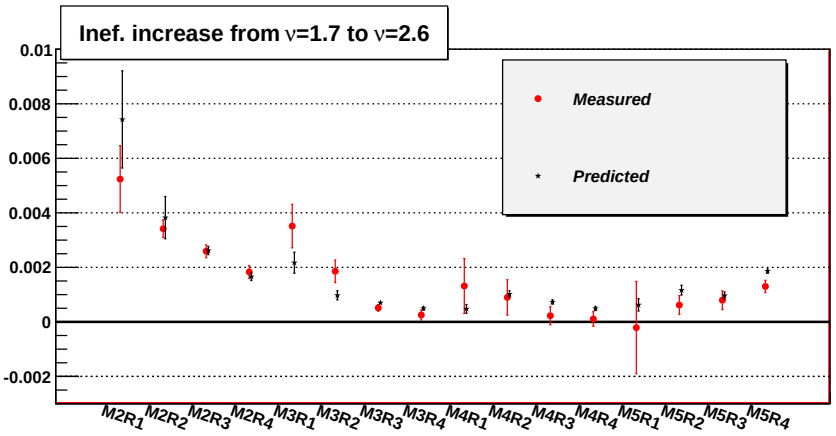

Figure 4.11: Measured variation of inefficiency of muon regions between runs at $\nu = 1.7$ and $\nu = 2.6$, compared with the estimated inefficiency due to dead time. The uncertainties on the measurements are statistical. The uncertainties on the prediction are systematic and are dominated by the assumed CARIOCA deadtime (75 ± 25 ns).

inefficiency on the muon identification performance at upgrade luminosities. The muon identification efficiency as a function of the momentum is obtained from a simulated sample of $B_s^0 \to \mu^+\mu^-$ events by randomly eliminating hits according to the inefficiencies extrapolated from data, corrected for the effect of residual MWPC hardware inefficiencies mentioned in Sect. 4.4.1. The results are shown in Fig. 4.12. The blue and red triangles correspond to the 2012 and upgrade

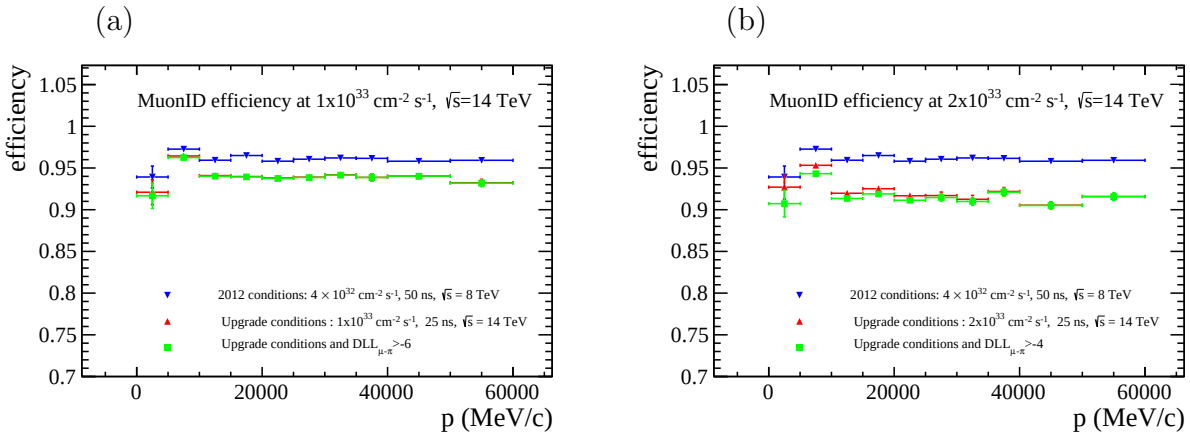

Figure 4.12: Muon identification algorithm efficiency versus momentum at a luminosity of 10^{33} cm^{-2}s^{-1} (a) and 2×10^{33} cm^{-2}s^{-1} (b) for the different criteria explained in the text, compared to the 2012 algorithm performance. The efficiency is obtained from a simulated sample of $B_s^0 \to \mu^+\mu^-$ events and is evaluated for single muons.

Table 4.6: Estimated inefficiencies due to dead time when operating at an instantaneous luminosity of 10^{33} cm^{-2}s^{-1} and 2×10^{33} cm^{-2}s^{-1} at 14 TeV collision energy and with 25 ns bunch spacing. The quoted errors reflect the unceratinties on the factors used for rate extrapolation, the average CARIOCA dead time (75 ± 25 ns), and the effect of additional shielding.

Region	Inefficiency at 10^{33} cm^{-2}s^{-1}	Inefficiency at 2×10^{33} cm^{-2}s^{-1}
M2R1	3.2 ± 1.2 %	7.1 ± 2.8 %
M2R2	2.0 ± 0.5 %	4.1 ± 1.1 %
M2R3	1.3 ± 0.2 %	2.6 ± 0.4 %
M2R4	0.9 ± 0.2 %	1.7 ± 0.3 %
M3R1	1.5 ± 0.4 %	3.3 ± 1.1 %
M3R2	0.6 ± 0.1 %	1.2 ± 0.3 %
M3R3	0.4 ± 0.1 %	0.9 ± 0.1 %
M3R4	0.3 ± 0.1 %	0.6 ± 0.1 %
M4R1	0.5 ± 0.2 %	1.1 ± 0.3 %
M4R2	0.6 ± 0.1 %	1.3 ± 0.2 %
M4R3	0.5 ± 0.1 %	0.9 ± 0.2 %
M4R4	0.3 ± 0.1 %	0.6 ± 0.1 %
M5R1	0.6 ± 0.2 %	1.3 ± 0.5 %
M5R2	0.7 ± 0.2 %	1.4 ± 0.3 %
M5R3	0.6 ± 0.1 %	1.2 ± 0.2 %
M5R4	1.2 ± 0.2 %	2.3 ± 0.3 %

running conditions respectively, using only the information of IsMuon variable. The extrapolated muon identification efficiency at the maximum upgrade luminosity of 2×10^{33} cm^{-2}s^{-1} is therefore found to be at the level of 90%, about 5% lower than that observed in 2012 LHCb running conditions, if only the IsMuon algorithm is used.

In assessing the PID performance at the upgrade it is also necessary to consider the misidentification rate. The fraction of misidentified pions and kaons is measured directly on data collected during 2012 using dedicated calibration samples of $D^0 \to K^-\pi^+$ decays. The calibration samples are divided in four bins according to the number of reconstructed tracks n_{trk}: $n_{trk} < 100$; $100 < n_{trk} < 200$; $200 < n_{trk} < 300$ and $300 < n_{trk} < 1000$. For each subsample the corresponding average number of primary vertices $< n_{PV} >$ is determined, giving respectively $< n_{PV} >= 1.4$, 2.1, 2.8 and 3.7. The misidentification is then measured in bins of momentum and is found to scale linearly with $< n_{PV} >$. The projection of the misidentification fractions at upgrade luminosities can thus be obtained from a linear extrapolation of present data.

The results for the pion misidentification fraction are shown in Fig. 4.13. The misidentification fraction at upgrade luminosities increases with respect to 2012 when only the IsMuon criterion is used. This effect is mainly due to the much higher hit occupancy expected in upgrade running conditions. The currently measured misidentification levels can be partially recovered in different momentum ranges applying appropriate $DLL_{\mu\pi}$ cuts. As an example, a soft $DLL_{\mu\pi}$ cut is sufficient to suppress significantly the misidentification at low momenta, where the misidentification fraction is higher, as shown in Fig. 4.13. The loss in muon identification efficiency due to the additional $DLL_{\mu\pi}$ cut is estimated through a linear extrapolation of the

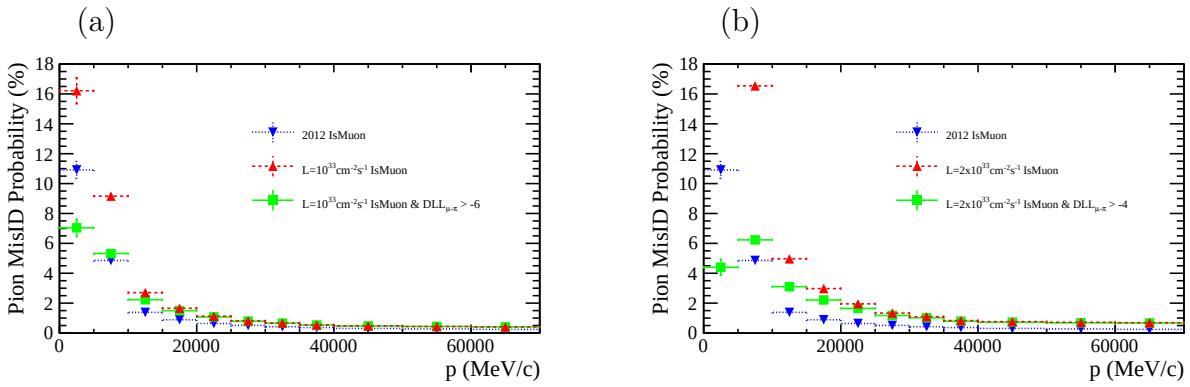

Figure 4.13: Pion misidentification probability versus particle momentum at a luminosity of 10^{33} cm^{-2}s^{-1} (a) and 2×10^{33} cm^{-2}s^{-1} (b) for the different criteria explained in the text, compared to the 2012 'IsMuon' algorithm performance. (Note that in order to improve readbility, the scale is chosen such that in the first bin of plot (b) the dashed red triangle entry is out of range.) The results are obtained with a linear extrapolation from data.

ratio of efficiencies ϵ(IsMuon AND DLL$_{\mu\pi}$cut)/ϵ(IsMuon) in each momentum bin. The result is shown in Fig. 4.12 (green squares). The additional loss in efficiency is found to be negligible and is concentrated at low momenta, as expected. All these results give confidence that the performance of the muon identification can be maintained close to the curent level, even at a luminosity of 2×10^{33} cm^{-2}s^{-1}. Further studies are ongoing to reoptimize the muon identification algorithms in order to cope better with upgrade running conditions. In addition, the effect on the muon identification performance of all the system modifications aimed at reducing the hit occupancy, such as additional shielding and the possible increase of logical channel granularity, will be carefully studied.

4.5 Project organisation

4.5.1 Work packages and responsibilities

The muon upgrade project is divided in different work packages which are under the responsibility of the INFN groups of Cagliari, Ferrara, Firenze, Frascati (LNF), Roma1, Roma2 and of PNPI and CERN. The work packages, together with the responsibilities, are listed in Table 4.7.

The R&D programme continues in the period until 2019. It will study high-granularity detectors for the innermost regions of M2 and M3, to be installed during LS3. This R&D activity, although described briefly in this document, is not an objective of the upgrade programme.

4.5.2 Manpower

The manpower needed for the muon upgrade project has been carefully evaluated. It is available within the groups participating in the project. The number of researchers involved will increase in 2014 and reaches a plateau of 16 FTEs that will be maintained up to the end of the installation

and commissioning phase in 2019. The numbers of engineers and technical stuff will rapidly increase in 2014, reaching 17 FTEs. This number will be maintained up to 2016 and will then gradually decrease at the completion of the construction phase, reaching a plateau of 13 FTEs that will be involved in the installation and commissioning phases.

4.5.3 Costs

The muon system upgrade costs have not changed much with respect to the FTDR [8], although the project has evolved substantially in the last year with respect to that which was outlined in the FTDR.

The design of a new muon system readout architecture has allowed a better use of the resources. In the current planning the construction of the spare boards needed to maintain the off-detector electronics has been replaced with the construction of new electronics boards, built with up-to-date electronics components, that will operate throughout the LHCb high luminosity run. The new readout boards will use the new GBT and Versatile Links, allowing an optimized use of the fibre bandwidth, resulting in a smaller number of links to be used and in a smaller number of TELL40s required to readout the M2-M5 stations, leading to significant savings with respect to the cost estimates of the FTDR.

These savings have allowed the planning of an upgrade to the muon system pulsing and control system, thus eliminating the need to build spares of obsolete modules, and allowing full advantage to be taken of the new clock and fast command distribution system. Furthermore, this initiative will also allow for more reliable and faster electronics configuration and monitoring procedures.

The current muon system upgrade costs, divided in the various categories, are presented in Table 4.8. These costs include a 15% contingency.

4.5.4 Project planning and milestones

The definition of the new muon system readout and control architecture has been completed during 2013. The design of the new boards, the nSYNC ASIC and all the required software

Table 4.7: Muon system upgrade project: work packages and responsibilities.

Work Package	**Responsibility**
New electronics architecture design	LNF, Cagliari, Roma1
New nSYNC ASICs	Cagliari
nODE readout board	LNF
nSB control board	Roma1
nPDM pulsing board	Roma1
Muon-specific TELL40 firmware	Roma2
New ECS	LNF, Roma1, Firenze, Ferrara
Spare MWPCs	LNF, PNPI
Extra shielding	CERN
Software	All INFN Institutes

Table 4.8: Muon system upgrade cost estimate (including 15% contingency). The number of pieces required for every item (including spares) is indicated in parentheses.

System		**[kCHF]**
Spare MWPC		**345**
	Wire	57
	PCB and HV bars	136
	Honeycomb, Faraday cages	45
	On-chamber electronics	23
	Construction consumables	30
	Infrastractures, shipment	54
Electronics		**1254**
	nSYNC ASIC (1000)	252
	nODE Boards (120)	312
	nSB Boards (132)	132
	nPDM Boards (10)	36
	TELL40/SOL40 boards (12)	420
	TELL40/SOL40 crates and fibres	102
Infrastracture		**100**
	Shielding	100
Total		**1699**

and firmware will start in 2014 and continue until 2018. The Gantt chart showing the time development of the different work packages is show in Fig. 4.14. The most important milestones shown in the Gantt chart are summarized in Table 4.9.

4.5.5 Risk assessment

A careful evaluation of the risks has been performed to assess the impact of possible delays in the muon upgrade project. Most of the activities described are decoupled from each other and a partial system installation and commissioning could be envisaged if needed. If any one activity were to be delayed to the extent that full commissioning of the new electronics could not be completed by the end of LS2, then the muon system could still be operated properly at 40 MHz (although with certain limitations and less redundancy) during the time required to complete this work, by keeping in operation part of the system currently used. The final installation could then be postponed to a later short shutdown period.

No major concerns are seen in the work packages referred to earlier. The nSYNC ASIC will be similar in functionality to the current SYNC ASIC and its design is not considered to be unusually challenging by our experts. The nODE is a simple carrier of the nSYNC chip, the GBT and GBT-SCA chips and the optical link drivers and the installation is mostly 'plug-and-play' and carries little risk. The nPDM and the nSB will be FPGA-based boards, and there are also no particular risks in the project thanks to the experience in FPGA-based board design of the groups involved. Installation will also be mostly 'plug-and-play'. The ECS reorganisation is foreseen to occur significantly in advance of LS2 to reduce the software commissioning time after

	Name	Start	Finish
1	**nSYNC**	**1/1/14 8:00 AM**	**6/30/17 5:00 PM**
2	Prototype develpoment	1/1/14 8:00 AM	12/31/14 5:00 PM
3	Prototype Ready	12/31/14 5:00 PM	12/31/14 5:00 PM
4	Prototype Production at Foundry	1/1/15 8:00 AM	6/30/15 5:00 PM
5	Prototype back from Foundry	6/30/15 5:00 PM	6/30/15 5:00 PM
6	Prototype Test and Final Chip Design	7/1/15 8:00 AM	7/1/16 5:00 PM
7	Final Chip ready for submission	7/1/16 5:00 PM	7/1/16 5:00 PM
8	Chip Production at Foundry	7/4/16 8:00 AM	12/30/16 5:00 PM
9	Final Chip back from Foundry	12/30/16 5:00 PM	12/30/16 5:00 PM
10	Chip Final Test	1/2/17 8:00 AM	6/30/17 5:00 PM
11	Project Completed	6/30/17 5:00 PM	6/30/17 5:00 PM
13	**nODE**	**1/1/14 8:00 AM**	**12/29/17 5:00 PM**
14	Prototype Development	1/1/14 8:00 AM	6/30/15 5:00 PM
15	Prototype Assembly and Test	7/1/15 8:00 AM	12/30/15 5:00 PM
16	Final Board Design	12/31/15 8:00 AM	6/30/17 5:00 PM
17	Board Assembly and Test	7/3/17 8:00 AM	12/29/17 5:00 PM
18	Project Completed	12/29/17 5:00 PM	12/29/17 5:00 PM
20	**nPDM**	**1/1/14 8:00 AM**	**12/29/17 5:00 PM**
21	Prototype	1/1/14 8:00 AM	6/30/15 5:00 PM
22	Prototype Ready	6/30/15 5:00 PM	6/30/15 5:00 PM
23	Production	7/1/15 8:00 AM	12/29/17 5:00 PM
24	Project Completed	12/29/17 5:00 PM	12/29/17 5:00 PM
26	**nSB**	**1/1/14 8:00 AM**	**12/29/17 5:00 PM**
27	Prototype	1/1/14 8:00 AM	6/30/15 5:00 PM
28	Prototype Ready	6/30/15 5:00 PM	6/30/15 5:00 PM
29	Production	7/1/15 8:00 AM	12/29/17 5:00 PM
30	Project Completed	12/29/17 5:00 PM	12/29/17 5:00 PM
32	**TELL40 Firmware**	**1/1/14 8:00 AM**	**12/29/17 5:00 PM**
33	TELL40 Firmware Development	1/1/14 8:00 AM	12/29/17 5:00 PM
34	Project Completed	12/29/17 5:00 PM	12/29/17 5:00 PM
36	**New ECS**	**1/1/14 8:00 AM**	**8/31/18 5:00 PM**
37	nODE ECS Development	1/1/14 8:00 AM	8/31/18 5:00 PM
38	nSB ECS Development	1/1/14 8:00 AM	8/31/18 5:00 PM
39	nPDM ECS Development	1/1/14 8:00 AM	8/31/18 5:00 PM
41	**Installation and Commissioning**	**1/1/18 8:00 AM**	**6/28/19 5:00 PM**
42	nODE Installation	1/1/18 8:00 AM	8/31/18 5:00 PM
43	nODE Commissioning	9/3/18 8:00 AM	6/28/19 5:00 PM
44	nPDM Installation	1/1/18 8:00 AM	8/31/18 5:00 PM
45	nPDM Commissioning	9/3/18 8:00 AM	6/28/19 5:00 PM
46	nSB Installation	1/1/18 8:00 AM	8/31/18 5:00 PM
47	nSB Commissioning	9/3/18 8:00 AM	6/28/19 5:00 PM
48	TELL40 Installation	1/1/18 8:00 AM	8/31/18 5:00 PM
49	TELL40 Commissioning	9/3/18 8:00 AM	6/28/19 5:00 PM
50	Commissioning Completed	6/28/19 5:00 PM	6/28/19 5:00 PM
52	**Spare MWPC**	**1/1/14 8:00 AM**	**12/29/17 5:00 PM**
53	Material Procurement	1/1/14 8:00 AM	12/31/14 5:00 PM
54	Production and Test	1/1/15 8:00 AM	12/29/17 5:00 PM

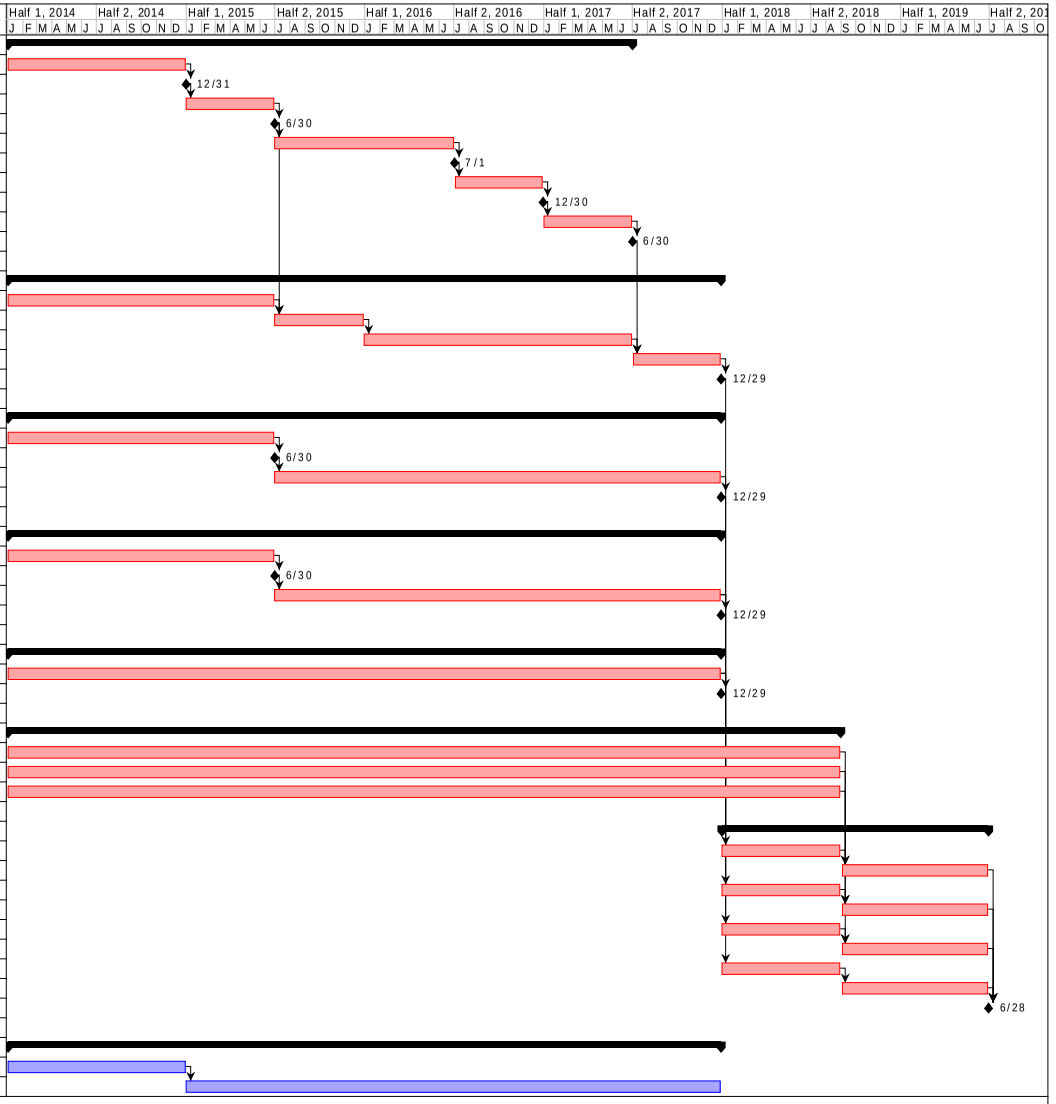

Muon Upgrade Project

Figure 4.14: Muon upgrade project planning.

Table 4.9: Muon system upgrade project: milestones.

Date	Milestone description
31/12/2014	nSYNC prototype submitted
30/06/2016	nSYNC final submission
30/06/2017	nSYNC ASICs fully tested
31/12/2015	nODE prototype tested
31/12/2017	nODE boards assembled and tested
30/06/2015	nPDM prototype ready
31/12/2017	nPDM boards assembled and tested
30/06/2015	nSB prototype ready
31/12/2017	nSB boards assembled and tested
31/12/2017	TELL40 muon firmware ready and tested
31/08/2018	New electronics installation completed
31/08/2018	ECS development completed
30/06/2019	Commissioning completed
31/12/2017	Spare MWPCs construction and test completed

hardware installation to the minimum.

The R&D programme for the new high-granularity detectors and related front-end electronics represents, de-facto, a contingency plan for the electronics upgrade. If it is found that running at upgrade luminosity will increase the inefficiency of the detector to a higher lever than expected due to detector dead time or to detector losses in performances arising from high radiation levels (space-charge effects and/or detector ageing), the new detectors developed during the R&D phase could be built earlier, in order to replace the ones located in the most irradiated regions.

4.5.6 Safety aspects

The muon detectors and the readout electronics of LHCb follow the CERN safety rules and codes, CERN safety document SAPOCO 42 and European and/or international construction codes for structural engineering as described in EUROCODE 3. The design of the additional shielding behind the HCAL, the upgraded electronics and the spare MWPCs will continue to comply with the same regulations.

Bibliography

[1] LHCb collaboration, R. Aaij *et al.*, *First observation of CP violation in the decays of B_s^0 mesons*, Phys. Rev. Lett. **110** (2013) 221601, arXiv:1304.6173.

[2] LHCb collaboration, R. Aaij *et al.*, *Measurement of the CKM angle γ from a combination of $B^\pm \to Dh^\pm$ analyses*, Phys. Lett. B **726** (2013) 151, arXiv:1305.2050.

[3] LHCb collaboration, R. Aaij *et al.*, *Measurement of the ratio of branching fractions $B(B^0 \to K^{*0}\gamma)/B(B_s^0 \to \phi\gamma)$ and the direct CP asymmetry in $B^0 \to K^{*0}\gamma$*, Nucl. Phys. B **867** (2012) 1, arXiv:1209.0313.

[4] CMS and LHCb collaborations, *Combination of results on the rare decays $B^0_{(s)} \to \mu^+\mu^-$ from the CMS and LHCb collaborations*, LHCb-CONF-2013-012,CMS-PAS-BPH-13-007.

[5] LHCb collaboration, R. Aaij *et al.*, *Measurement of the $B_s^0 \to \mu^+\mu^-$ branching fraction and search for $B^0 \to \mu^+\mu^-$ decays at the LHCb experiment*, Phys. Rev. Lett. **111** (2013) 101805, arXiv:1307.5024.

[6] LHCb collaboration, R. Aaij *et al.*, *First Evidence for the Decay $B_s^0 \to \mu^+\mu^-$*, Phys. Rev. Lett. **110** (2012) 021801, arXiv:1211.2674.

[7] LHCb collaboration, *Letter of Intent for the LHCb Upgrade*, CERN-LHCC-2011-001.

[8] LHCb collaboration, *Framework TDR for the LHCb Upgrade: Technical Design Report*, CERN-LHCC-2012-007.

[9] LHCb collaboration, R. Aaij *et al.*, *Implications of LHCb measurements and future prospects*, Eur.Phys.J. **C73** (2013) 2373, arXiv:1208.3355.

[10] LHCb collaboration, *LHCb RICH Technical Design Report*, CERN/LHCC 2000-37.

[11] LHCb collaboration, A. A. Alves Jr. *et al.*, *The LHCb Detector at the LHC*, JINST **3** (2008) S08005.

[12] M. Adinolfi *et al.*, *Performance of the LHCb RICH detector at the LHC*, Eur. Phys. J. C **73** (2013) 2431, arXiv:1211.6759.

[13] R. Forty, *TRIDENT: a new concept for particle identification in the upgrade* , LHCB-PUB-2012-012.

[14] C. d'Ambrosio, S. Easo, C. Frei and A. Petrolini, *RICH2019: a proposal for the LHCb-RICH upgrade* , LHCb-PUB-2013-011.

[15] J.-P. Cachemiche, P.-Y. Duval, F. Hachon, R. Le Gac and F. Rethore, *Readout board specifications for the LHCb upgrade*, https://edms.cern.ch/document/1251709/1 (2012).

[16] Omega micro group. http://http://omega.in2p3.fr/.

[17] C. Arnaboldi *et al.*, *Crosstalk study of the single-photon response of a flat-panel PMT for the RICH upgrade at LHCb*, IEEE Trans.Nucl.Sci. **57** (2010) 2267.

[18] M. Calvi *et al.*, *Characterization of a Hamamatsu R7600 multi-anode photomultiplier tube with single photon signals*, JINST **8** (2013) P02012.

[19] R. Chamonal, *Multianode photomultiplier tubes for the LHCb RICH photodetectors*, CERN-THESIS-2006-016 (2005).

[20] P. Carniti *et al.*, *CLARO-CMOS, a very low power ASIC for fast photon counting with pixellated photodetectors*, JINST **7** (2012) P11026, arXiv:1209.0409.

[21] A. Gabrielli *et al.*, *The GBT-SCA, a radiation tolerant ASIC for detector control applications in SLHC experiments*, Topical Workshop on Electronics for Particle Physics, Paris, France, 21 - 25 Sep 2009, pp.557-560.

[22] P. Barrillon and S. Blin, *The MAROC3 datasheet*, http://omega.in2p3.fr/.

[23] F. Faccio, contact person, *Development of DCDC converters at CERN*, https://espace.cern.ch/GBT-Project/default.aspx.

[24] M. Adinolfi *et al.*, *LHCb RICH 2 Engineering Design Review Report*, LHCb-2002-009.

[25] A. Petrolini, *RICH 1 and LHCb-RICH upgrade: reoptimization of the optics*, LHCb-PUB-2013-012.

[26] N. Brook *et al.*, *LHCb RICH 1 Engineering Design Review Report*, LHCb-2004-121.

[27] *The LHCb magnetic shielding*, EDMS-LHCB-0070, https://edms.cern.ch/nav/LHCB-0070/.

[28] M. Ameri *et al.*, *Design of a base-board for arrays of closely-packed multi-anode photomultipliers*, Nucl.Instrum.Meth. **A550** (2005) 559, arXiv:physics/0412175.

[29] P. Musico, M. Pallavicini, A. Petrolini, and F. Pratolongo, *First results of VLSI Front End Electronics for photo detectors*, Nucl.Instrum.Meth. **A518** (2004) 210.

[30] A. Santangelo and A. Petrolini, *Observing Ultra High Energy Cosmic Particles from Space: SEUSO, the Super Extreme Universe Space Observatory Mission*, arXiv:0909.5370.

[31] E. Albrecht *et al.*, *Performance of a cluster of multi-anode photomultipliers equipped with lenses for use in a prototype RICH detector*, Nucl.Instrum.Meth. **A488** (2002) 110.

[32] I. Arino *et al.*, *The HERA-B RICH*, Nucl.Instrum.Meth. **A453** (2000) 289.

[33] P. Abbon *et al.*, *Pattern recognition and PID for COMPASS RICH-1*, Nucl.Instrum.Meth. **A595** (2008) 233, arXiv:0902.0444.

[34] A. Petrolini, *A comparative study of light collector systems for use with multi-anode photo-multipliers*, Nucl.Instrum.Meth. **A497** (2013) 314.

[35] L. C. Klein, *Sol-Gel Materials*, Annual Review of Materials Science **23** (1993) 437.

[36] K. Wyllie *et al.*, *Electronics Architecture of the LHCb Upgrade*, LHCb-PUB-2011-011.

[37] L. Amaral *et al.*, *The versatile link, a common project for super-LHC*, JINST **4** (2009) P12003.

[38] F. Vasey *et al.*, *The versatile link common project: feasibility report*, JINST **7** (2012) C01075.

[39] C. Frei, *Cooling System of the RICH detectors*, `https://edms.cern.ch/document/1327542`.

[40] L.-P. D. Menezes, *LHCb RICH 1 Gas System*, 2008. `https://edms.cern.ch/document/892773/1`.

[41] L.-P. D. Menezes, *LHCb RICH 2 Gas System*, 2008. `https://edms.cern.ch/document/892775/1`.

[42] T. Sjöstrand, S. Mrenna, and P. Skands, *PYTHIA 6.4 Physics and manual*, JHEP **05** (2006) 026, `arXiv:hep-ph/0603175`.

[43] D. J. Lange, *The EvtGen particle decay simulation package*, Nucl.Instrum.Meth. **A462** (2001) 152.

[44] P. Golonka and Z. Was, *PHOTOS Monte Carlo: a precision tool for QED corrections in Z and W decays*, Eur.Phys.J. **C45** (2006) 97, `arXiv:hep-ph/0506026`.

[45] GEANT4 collaboration, J. Allison *et al.*, *Geant4 developments and applications*, IEEE Trans.Nucl.Sci. **53** (2006) 270; GEANT4 collaboration, S. Agostinelli *et al.*, *GEANT4: A simulation toolkit*, Nucl.Instrum.Meth. **A506** (2003) 250.

[46] M. Clemencic *et al.*, *The LHCb simulation application,* GAUSS*: design, evolution and experience*, J. of Phys: Conf. Ser. **331** (2011) 032023.

[47] S. Easo *et al.*, *Simulation of LHCb RICH detectors using GEANT4*, IEEE Trans.Nucl.Sci. **52** (2005) 1665.

[48] R. Forty, *RICH pattern recognition for LHCb*, Nucl.Instrum.Meth. **A433** (1999) 257.

[49] LHCb collaboration, *LHCb Reoptimized detector design and performance: Technical Design Report*, CERN/LHCC 2003-030.

[50] SAPOCO 42, EDMS 359387. `http://safety-commission.web.cern.ch/safety-commission/sapoco42/`.

[51] C. Frei, *Safety aspects of the RICH detectors*, `https://edms.cern.ch/document/1327565`.

[52] J. Milnes, *The TORCH PMT, a close packing, multi-anode, long life MCP-PMT for Cherenkov applications*, Presented at the DIRC 2013 workshop on fast Cherenkov detectors, Giessen, Germany (4–6 September 2013).

[53] R. Forty and M. Charles, *TORCH: Time of Flights Identification with Cherenkov Radiation*, Nucl.Instrum.Meth. **A639** (2011) 173.

[54] N. Harnew, *A large-area detector for precision time-of-flight measurements (TORCH)*, The support of the European Research Council is gratefully acknowledged in the funding of this work (call identifier: ERC-2011-AdG, 291175-TORCH).

[55] L. Castillo Garcia, *Timing performance of a MCP photon detector read out with multi-channel electronics for the TORCH system*, To be published in Proc. of 14th ICATPP Conference, Como, Italy (23–27 September 2013).

[56] R. Gao, *Development of precision time-of-flight electronics for LHCb TORCH*, To be published in Proc. of TWEPP 2013 Conference, Perugia, Italy (23–27 September 2013).

[57] F. Anghinolfi *et al.*, *NINO: An ultra-fast and low-power front-end amplifier/discriminator ASIC designed for the multigap resistive plate chamber*, Nucl.Instrum.Meth. **A533** (2004) 183.

[58] J. Christiansen *et al.*, *A data driven high performance time to digital converter*, Conf.Proc. **C00091111** (2000) 169.

[59] E. Albrecht *et al.*, *First observation of Cherenkov ring images using hybrid photon detectors*, Nucl.Instrum.Meth. **A411** (1998) 249.

[60] E. Albrecht *et al.*, *Performance of hybrid photon detector prototypes with 80% active area for the RICH counters of LHCB*, Nucl.Instrum.Meth. **A442** (2000) 164.

[61] BTeV collaboration, R. Mountain, *Development of a hybrid photodiode and its front end electronics for the BTeV experiment*, Nucl.Instrum.Meth. **A502** (2003) 183, `arXiv:hep-ex/0209050`.

[62] P. Cushman, A. Heering, and A. Ronzhin, *Custom HPD readout for the CMS HCAL*, Nucl.Instrum.Meth. **A442** (2000) 289–294.

[63] C. Parkes *et al.*, *Preliminary specification of a silicon strip readout chip for the LHCb Upgrade*, LHCb-PUB-2012-011.

[64] M. Agari *et al.*, *Beetle: A radiation hard readout chip for the LHCb experiment*, Nucl.Instrum.Meth. **A518** (2004) 468.

[65] ALIBAVA collaboration, R. Marco-Hernandez, *A portable readout system for silicon microstrip sensors*, Nucl.Instrum.Meth. **A623** (2010) 207.

[66] LHCb collaboration, *LHCb calorimeters Technical Design Report*, CERN-LHCC-2000-036.

[67] C. Abellan Beteta *et al.*, *Performance of the LHCb calorimeters*, to be submitted to JINST (2013).

[68] LHCb collaboration, R. Aaij *et al.*, *Letter of Intent for the LHCb upgrade*, CERN-LHCC-2011-001.

[69] D. Gascon *et al.*, *Low Noise Front End ASIC With Current Mode Active Cooled Termination for the Upgrade of the LHCb Calorimeter*, IEEE Trans.Nucl.Sci. **59** (2012) .

[70] E. Picatoste *et al.*, *Low Noise Front End ASIC with Current Mode Active Cooled Termination for the Upgrade of the LHCb Calorimeter*, JINST **7** (2011) C01080.

[71] Y. Chouia *et al.*, *14b, 50MS/s CMOS Front-End Sample and Hold Module Dedicated to a Pipelined ADC*, proceedings of the MWSCAS '04 symposium **1** (2004) I–353–6.

[72] C. Abellan Betata *et al.*, *Study of a solution with COTS for the LHCb calorimeter upgrade*, Physics Procedia **37** (2012) 1744.

[73] C. Beigbeder-Beau *et al.*, *The front end electronics for the LHCb calorimeters*, LHCb-1999-053.

[74] C. Beigbeder-Beau *et al.*, *The front-end electronics for LHCb calorimeters*, LHCb-2000-028.

[75] C. Beigbeder-Beau *et al.*, *Description of the ECAL/HCAL front-end card*, LHCb-2003-036.

[76] P. Moreira *et al.*, *The GBT Project*, Proceedings of conference TWEPP 2009 (2009) 342.

[77] C. Beigbeder-Beau *et al.*, *The trigger part of the of the calorimeter front-end card*, LHCb-2003-037.

[78] C. Abellan Beteta *et al.*, *Time alignment of the front end electronics of the LHCb calorimeters*, JINST **7** (2012) P08020.

[79] C. Beigbeder-Beau *et al.*, *The front-end electronics for the calorimeter triggers*, LHCb-2000-010.

[80] K. Wyllie *et al.*, *Electronics architecture of the lhcb upgrade*, LHCb-PUB-2011-011.

[81] D. Gascon *et al.*, *Cards, crates and connections for the calorimeters*, LHCb-2003-121.

[82] D. Breton *et al.*, *SPECS: A Serial Protocol for the Experimental Control System*, EDMS 985335.

[83] T. Skwarnicki, *A study of the radiative cascade transitions between the Upsilon-prime and Upsilon resonances*. PhD thesis, Institute of Nuclear Physics, Krakow, 1986. DESY-F31-86-02.

[84] L. Breiman, J. H. Friedman, R. A. Olshen, and C. J. Stone, *Classification and regression trees*. Wadsworth international group, Belmont, California, USA, 1984.

[85] A. A. Alves Jr. *et al.*, *Performance of the LHCb muon system*, JINST **8** (2013) P02022.

[86] F. Archilli *et al.*, *Performance of the Muon Identification at LHCb*, JINST **8** (2013) P10020.

[87] LHCb collaboration, *LHCb muon system Technical Design Report*, CERN/LHCC-2001-010.

[88] LHCb collaboration, *LHCb: addendum to the muon system Technical Design Report*, CERN-LHCC-2003-002.

[89] M. Anelli *et al.*, *High radiation tests of the mwpcs for the lhcb muon system*, Nucl.Instrum.Meth. **A599** (2009) 171.

[90] D. Pinci, *Performance of the Muon MWPC in high luminosity runs*, LHCb-PUB-2013-005. CERN-LHCb-PUB-2013-005.

[91] M. Anelli *et al.*, *Extensive aging test of two prototypes of four-gap MWPC for the LHCb Muon System*, LHCb-2004-029.

[92] G. Bencivenni *et al.*, *Study of new high granularity detectors for the LHCb muon system*, LHCb-PUB-2013-019.

[93] R. Paluch, R. Oldeman, and B. Schmidt, *Additional shielding behind the LHCb muon detector*, LHCb-PUB-2013-021.

[94] G. Felici *et al.*, *The Muon Detector FE Trigger Electronics*, presented at 9th Workshop on Electronics for LHC Experiments, Amsterdam, the Netherlands, 2003, doi: 10.5170/CERN-2003-006.

[95] LHCb collaboration, *LHCb Technical Proposal*, CERN/LHCC-98-4.

[96] R. Paluch and B. Schmidt, *Additional shielding in front of M2*, LHCb-PUB-2013-022.

[97] W. Bonivento, W. Moraes, D, N. Pelloux, and W. Riegler, *The CARIOCA Front End Chip for the LHCb muon chambers*, Nucl.Instrum.Meth. **A491** (2002) 233.

[98] S. Cadeddu, A. Lai, and C. Deplano, *The DIALOG chip in the front-end electronics of the LHCb muon detector*, IEEE Trans.Nucl.Sci. **52** (2005) 2726.

[99] A. Balla *et al.*, *The L0 Off Detector Electronics (ODE) for the LHCb muon spectrometer*, presented at the 10th Workshop on Electronics for LHC and Future Experiments, Boston, USA, 2004, doi: 10.5170/CERN-2004-010.

[100] A. Balla *et al.*, *The Off Detector Electronics of the LHCb Muon Detector*, IEEE Trans.Nucl.Sci **2** (2006) 1296.

[101] S. Cadeddu, V. De Leo, C. Deplano, and A. Lai, *The SYNC Chip in the Electronics Architecture of the LHCb Muon Detector*, IEEE Trans.Nucl.Sci. **57** (2010) 2790.

[102] P. Moreira, *Qpll manual*, `http://proj-qpll.web.cern.ch/proj-qpll/images/qpllManual.pdf`.

[103] F. Legger *et al.*, *TELL1 : a common readout board for LHCb*, LHCb-2004-100.

[104] V. Bocci, G. Chiodi, F. Iacoangeli, F. Messi, and R. Nobrega, *The Muon Front-End Control Electronics of the LHCb Experiment*, IEEE Trans.Nucl.Sci. **57** (2010) 3807.

[105] R. Jacobsson *et al.*, *Timing and fast control*, LHCb-2001-016.

[106] Technical documentation on the ELMB can be found at `http://atlas.web.cern.ch/Atlas/GROUPS/DAQTRIG/DCS/LMB/SB/index.html`.

[107] V. Bocci *et al.*, *The LHCb muon control system the DAQ domain*, IEEE Trans.Nucl.Sci. **3** (2007) 1737.

[108] P. Moreira *et al.*, *The GBT-SerDes ASIC prototype*, JINST **5** (2010) C11022.